

Evaluation of the Radiation Scheme of a Numerical Weather Prediction Model by Airborne Measurements of Spectral Irradiance above Clouds

Von der Fakultät für Physik und Geowissenschaften

der Universität Leipzig

genehmigte

DISSERTATION

zur Erlangung des akademischen Grades

Doktor der Naturwissenschaften
(Dr. rer. nat)

vorgelegt

von Master of Science Kevin Wolf

geboren am 17. November 1990 in Schmalkalden / Thüringen

1. Gutacher: Prof. Dr. Manfred Wendisch
2. Gutachter: Prof. Dr. Felix Ament

Tag der Verleihung: 18. Mai 2020

Bibliographische Beschreibung:

Wolf, Kevin

Evaluation of the Radiation Scheme of a Numerical Weather Prediction Model
by Airborne Measurements of Spectral Irradiance above Clouds.

Universität Leipzig, Dissertation

109 S., 143 Lit., 41 Abb., 18 Tab., 6 Anlagen

Referat:

In dieser Arbeit wird ein neuartiger Ansatz vorgestellt, bei dem die aufwärts- und abwärtsgerichtete Irradianz F von flugzeuggetragenen Messungen mit Strahlungssimulationen verglichen wird. Die Simulationen werden entlang des untersuchten Flugweges, mit dem Strahlungsmodul ecRad des Wettervorhersagemodells Integrated Forecast System (IFS) des European Centre for Medium Range Weather Forecast (ECMWF) durchgeführt. Analog zu den ecRad Simulationen, erfolgen Berechnungen mit der library for Radiative transfer (libRadtran), welche als Referenz für ecRad dienen. Beide Strahlungstransportmodelle (STM) basieren auf den gleichen IFS Analysedaten (IFS AD). Die simultane Verwendung beider STM und der Abgleich mit den durchgeführten Messungen erlaubt es, mögliche Fehler in den STM und den Analysedaten zu separieren. Neben einer breitbandigen Untersuchung im solaren Spektralbereich (266 – 2050 nm Wellenlänge), ermöglicht die spektrale Analyse einzelner Wellenlängenbänder des ecRad eine Verifizierung der operationellen Eiskristallparametrisierung, welche die wolkenmikrophysikalischen Parameter mit den wolkenoptischen Parametern verknüpft.

Die Auswertungen basieren auf einem vollständigen Messflug der Next Generation Remote Sensing for Validation Studies (NARVAL-II) Feldstudie, sowie einzelner Wolkensegmente der North Atlantic Waveguide and Downstream impact EXperiment (NAWDEX) Messkampagne. Aus dem gewählten NAWDEX Flug werden drei charakteristische Wolkenabschnitte ausgewählt. Zwei Abschnitte sind durch eine von der Eisphase dominierten Wolkenoberkannte gekennzeichnet. Der dritte Abschnitt stellt ein Wolkenregime dar, dass sich auf eine heterogene Flüssigwasserwolke konzentriert.

Die Analyse zeigt eine grundlegende Übereinstimmung von gemessenem und simuliertem Strahlungsfeld innerhalb der Messunsicherheiten. Während stratiforme Flüssigwasserwolken gut repräsentiert sind, tritt eine systematische Abweichung zwischen simulierten und gemessenen Strahlungsflussdichten F für Eiswasserwolken auf. Diese Differenzen sind für Wellenlängen über 1200 nm signifikant. Die Ursache der Abweichung ist auf die reduzierte spektrale Auflösung der Einfachstreualbedo in der Eiskristall-Parametrisierung zurückzuführen. Zusätzlich tritt für homogene Wolkenabschnitte eine systematische und wellenlängenunabhängige Unterschätzung der gemessenen F auf. Dies deutet auf einen zu geringen Eis- und Flüssigwasserpfad in den IFS AD hin. Für heterogene Segmente zeigt sich in den simulierten Strahlungsprofilen eine geringer Variabilität als beobachtet wurde, was auf die reduzierte räumliche Auflösung der IFS AD zurückgeführt wird. Zu der Unterschätzung der simulierten F tragen auch Defizite in der Wolkenrepräsentation von Grenzschichtwolken in arktischen Kaltluftausbrüchen bei.

Während des gewählten NARVAL-II Flugs wurden vorwiegend räumlich heterogen verteilte Passatwindwolken beobachtet. Die Analyse dieses Flugs zielt auf die Überprüfung der generelle Wolkenrepräsentation in Bezug auf Bedeckungsgrad, aufwärts gerichtet Irradianz, sowie die Wolkenalbedo ab. Für den gesamten Flug zeigt sich eine gute Übereinstimmung der simulierten F zwischen den beiden Modellen, wobei alle Simulationen kontinuierlich unterhalb der Messungen liegen. Separation der einzelnen Wolkenprofile nach Bedeckungsgrad und Flüssigwasserpfad LWP , deuten auf eine Überschätzung des Bedeckungsgrades und einen zu geringen LWP in den Analysedaten hin.

Für den NARVAL-II Flug werden Abschätzungen der Tropfenanzahlkonzentration N ermittelt, welche mit einer verbesserten Fernerkundungsmethode abgeleitet werden. Die Bestimmung von N basiert auf einer Kombination von passiven und aktiven Fernerkundungsinstrumenten, welche ein spektral auflösendes Radiometer, ein Mikrowellenprofiler, ein Wolkenradar und ein Lidar umfasst. Dadurch können synergetische Effekte der Instrumente genutzt werden, um die natürliche Variabilität von Wolken zu berücksichtigen und gleichzeitig Unsicherheiten in der Bestimmung von N verringern. Die abgeleitete Tropfenanzahlkonzentration wird in die Strahlungssimulationen von ecRad eingebunden, die Berechnungen wiederholt und mit den ecRad Referenzsimulationen verglichen, welche auf der Annahme einer konstanten N beruhen. Dabei zeigen sich lediglich geringe relative Unterschiede, die innerhalb des Fehlerbereichs der Strahlungsmessungen liegen.

Im Zuge dessen wird mit beiden Strahlungsmodellen eine Sensitivitätsstudie für optisch dünne Passatwindwolken durchgeführt, um den qualitativen Einfluss von Änderungen in N und LWP zu bestimmen. Die Studie zeigt zwischen beiden Modellen unterschiedliche Abhängigkeiten der Wolkenalbedo auf Änderungen des LWP . Für ecRad wird eine nicht-Linearität beobachtet, die dazu führt, dass die Wolkenalbedo für $LWP < 50 \text{ g m}^{-2}$ überschätzt und für $LWP > 100 \text{ g m}^{-2}$ unterschätzt wird.

Bibliographic Description:

Wolf, Kevin

Evaluation of the Radiation Scheme of a Numerical Weather Prediction Model
by Airborne Measurements of Spectral Irradiance above Clouds.

University of Leipzig, Dissertation

109 p., 143 ref., 41 fig., 18 tab., 6 add.

Abstract:

In this thesis a novel approach to compare airborne observations of spectral upward and downward irradiances F with along-track radiative transfer simulations (RTS) are presented. The RTS are performed with the ecRad radiation scheme of the Integrated Forecast System (IFS) operated by the European Centre for Medium Range Weather Forecast (ECMWF) and the library for Radiative transfer (libRadtran) on basis of hourly 0.1° IFS analysis data (IFS AD). The comparison aims to investigate the general capability of the utilized models to reproduce the observed radiation field. Simultaneous utilization of ecRad and libRadtran, driven by the same IFS AD, and comparison with observations enables to separate for potential errors in the applied IFS AD and ecRad. Analyzing spectral band-resolved upward and downward F enables to verify applied ice cloud parameterizations. In course of this work one research flights (RF) from the Next Generation Remote Sensing for Validation Studies (NARVAL-II) and the North Atlantic Waveguide and Downstream impact EXperiment (NAWDEX) are investigated, respectively.

From the NAWDEX RF, three characteristic cloud cases are selected, representing two stratiform ice clouds and a heterogeneous liquid water cloud section. The analysis shows, that the IFS AD and the model simulations are able to reproduce the observed radiation patterns in general, but are not capable to cover the observed along-track variability. Stratiform liquid water clouds are sufficiently represented in the IFS AD and related simulations of F . In contrast, ecRad simulations with the Fu ice parameterization of ice-topped clouds show systematic underestimations of upward F for wavelength larger than 1200 nm, while libRadtran benchmark simulations of F agree with the observations. Investigation of the ice phase sections indicate for systematic deficiencies in the ice optical parameterization of Fu but also for shortcomings in the cloud representation in the IFS AD by lower than observed ice water content.

The NARVAL-II RF is investigated with respect to the overall statistical cloud representation for cloud cover, upward F , and cloud top albedo. For this flight retrievals of Cloud Droplet Number Concentration N are available, using an extended technique to exploit synergistic airborne remote sensing observations. The retrieval applies a combination of a spectroradiometer, a microwave profiler, a cloud radar, and a lidar system. Resulting estimates of N are applied in the RTS to assess the potential influences of estimated N on simulated F .

Simultaneous sensitivity studies with ecRad and libRadtran, by varying LWP and N for typical values of trade wind cumuli, revealed the importance of precise parameterization of these clouds in Numerical Weather Prediction and Global Climate Models. The analysis indicates a reduced response of ecRad on changes of LWP and N compared to libRadtran, leading to an overestimation of simulated upward F for $LWP < 50 \text{ g m}^{-2}$ and an underestimation of upward F for $LWP > 100 \text{ g m}^{-2}$. For the NARVAL-II RF a reasonable overall agreement within the uncertainty range among the models and the observations was found, with indications for too high total cloud cover, due to the cloud overlap assumption, but a lack of liquid water path (LWP) in the IFS AD, which, in total, lead to an underestimation of F by both models compared to the observations.

Science knows no country,
because knowledge belongs to humanity,
and is the torch which illuminates the world.

Louis Pasteur (1822-1895)

Contents

1	Modeling of the Earths Atmosphere	1
1.1	Influence of Clouds on the Top-of-Atmosphere Radiation Budget	1
1.2	Challenges in Simulating Cloud Radiative Forcing	1
1.3	Model Validation	3
1.4	Retrieval of Cloud Optical Properties	5
1.5	Hypothesis	5
1.6	Outline	6
2	Fundamentals	7
2.1	Radiative Quantities	7
2.2	Cloud Optical Properties	8
2.3	Radiative Transfer Equation	11
2.4	Microphysical Properties	12
2.5	Radiative Transfer Module 'ecRad'	14
2.5.1	ecRad Model Atmosphere and Spectral Bands	15
2.5.2	Optical Properties	16
2.5.3	Radiative Transfer Solver	18
2.6	library for Radiative transfer (libRadtran)	18
2.7	Independent Pixel Approximation	19
3	Instrumentation and Observations	21
3.1	High Altitude and Long Range Research Aircraft (HALO)	21
3.2	Instrumentation	21
3.2.1	Spectral Modular Airborne measurement sysTem (SMART)	22
3.2.2	HALO Microwave Package (HAMP)	27
3.2.3	Additional Intrumentation	28
3.2.4	Moderate Resolution Imaging Spectroradiometer (MODIS)	28
3.3	Next Generation Remote Sensing for Validation Studies II	28
3.4	North Atlantic Waveguide and Downstream impact EXperiment	30
4	Retrieval of Cloud Droplet Number Concentration	33
4.1	Data Filtering	33
4.1.1	Cloud, Precipitation, and Phase Identifier	33
4.2	Cloud Optical Thickness and Effective Radius	34
4.3	Retrieval of Cloud Droplet Number Concentration	35
4.3.1	Method A: Based on Cloud Optical Thickness and Droplet Effective Radius . .	35
4.3.2	Method B: Based on Liquid Water Path and Droplet Effective Radius	36
4.3.3	Method C: Based on Liquid Water Path, Droplet Effective Radius, and Cloud Geometric Thickness	36
4.3.4	Calculation of Retrieval Uncertainty of Cloud Droplet Number Concentration .	36
4.4	Application of CDNC Retrieval on NARVAL-II Flight	38
4.5	Statistical Analysis of Liquid Water Path, Droplet Effective Radius, and Number Concentration	41
5	Simulations and Measurements Along HALO Flight Tracks	43
5.1	IFS Analysis Data	43
5.2	ecRad Model Setup	43
5.2.1	Input Data for ecRad Simulations	43
5.2.2	Output from ecRad Simulations	46
5.3	Sensitivity of ecRad to Variations in IFS Input-Data	48

5.4	libRadtran	49
5.4.1	Input Data for libRadtran Simulations	49
5.4.2	Output from libRadtran	50
5.5	Comparison of Modeled Albedo Sensitivity on Trade Wind Cumulus	50
5.6	Model Caveats	53
5.6.1	Representativeness of the Observations	53
5.6.2	Deviations between Modeled and Observed Irradiance	53
5.7	Comparison of Along-Track Measured and Simulated Irradiance	55
5.7.1	Downward Irradiance	55
5.7.2	Upward Irradiances of Stratiform Cloud Fields	55
5.7.3	Upward Irradiance of Trade Wind Cumuli	66
6	Summary and Conclusions	77
7	Appendix	81
7.1	Setup up of Radiation Scheme / Configuration of Namelist	81
7.2	Set-up of libRadtran	83
	Bibliography	91
	List of Symbols	100
	List of Abbreviations and Acronyms	105
	List of Figures	107
	List of Tables	109

1 Modeling of the Earths Atmosphere

1.1 Influence of Clouds on the Top-of-Atmosphere Radiation Budget

Numerical Weather Prediction (NWP) and Global Climate Models (GCMs) are numerical tools to describe the Earths atmosphere based on equations, assumptions, and parameterizations. Unfortunately, their accuracy is limited by the complexity and the staggering number of processes, inadequate quantified interactions, and a lack of process understanding (Bony and Dufresne, 2005). Focusing on the Earth atmosphere, physical processes inside clouds, atmosphere-ocean-interactions, and the radiative transport of solar radiation from the top-of-atmosphere (TOA) to the Earth's surface, are one of the most challenging parts of todays NWP and GCMs.

The individual components of the Earth's atmosphere, e.g., cloud and precipitation particles, aerosol particles, and gas molecules alter the distribution of the incident solar radiation by scattering and absorption. Clouds, in particular, modulate the Earth's radiative energy budget significantly and, by that, the amount of downward radiation reaching the surface and upward radiation leaving the system at the TOA (Chen et al., 2000). The impact of clouds on the radiative transport is quantified by the cloud radiative forcing (CRF), which is defined as the difference of the net (downward minus upward) irradiances between cloudy and cloud-free conditions. The CRF depends on the total cloud cover, the liquid water path, cloud height and thickness, cloud droplet number concentration, and the thermodynamic phase (Baran et al., 1999; Jensen et al., 1994). As a consequence of the overall natural cloud variability and the number of variables, which influence the CRF, it differs over a wide range (Rosenfeld, 2006): While for cirrus a warming effect dominates; boundary layer clouds and trade wind cumuli typically cool the subjacent atmosphere and surface by efficiently reflecting solar radiation (Warren et al., 1988). Due to this variety of cloud appearance, simulations of radiation fluxes in NWP and GCM are subject to several challenges, which require continuous model updates.

One leading example is the Integrated Forecast System (IFS) of the European Centre for Medium Range Forecast (ECMWF), which is a global NWP model well known for its data assimilation system and forecast accuracy. Nevertheless, the IFS model is under permanent development and evaluation (Geer et al., 2017).

1.2 Challenges in Simulating Cloud Radiative Forcing

Within the IFS the Radiative Transfer Equations (RTE) are solved by the radiation scheme ecRad for spectral bands with each covering several hundred nanometers wavelength, which are grouped for similar radiative properties. Currently, the operational 10-day forecast is calculated with a horizontal resolution of 9 km, 137 vertical model levels covering the entire Earth, and an hourly output. These model specifications restrict the capability to simulate the radiative transfer, e.g., by missing cloud-radiation-feedbacks and rapid cloud development. As a result, several IFS and ecRad related issues are reported (Hogan et al., 2017), from which four are approached within this thesis:

Cloud Overlap Assumption

The cloud overlap assumption (COA) determines the vertical distribution of cloud layers within an atmospheric column and, thus, the resulting total cloud cover and irradiance profiles. The COA becomes increasingly important for heterogeneous cloud fields. Comparisons with observations indicate that the so called 'exponential-random' parameterization, where adjacent cloud layers are exponentially coupled and cloud clusters are randomly distributed, fits the natural cloud distribution best (Hogan et al., 2000). The fractional standard deviation (FSD) of clouds in the model column, describes the cloud-to-cloud variability or cloud heterogeneity and influences the simulated radiation profile, which also requires in-situ reconciliation. Observations by Shonk et al. (2010) suggests a global average FSD of 0.75, whereby the case to case FSD depends on the observed cloud type and situation. Higher

then average FSD were found in the tropics while lower values appear for Arctic boundary layers. Therefore, the FSD and COA validation in different areas is required.

Effective Radius of Liquid Water Droplets and Ice Crystals

The representation of clouds in NWP and GCMs relies on parameterizations, which translate the cloud macrophysical and microphysical properties into the cloud optical properties. In case of liquid water clouds with spherical droplets the optical properties are accurately described by the Lorenz-Mie-theory and pre-calculated look-up-tables (LUT). Despite that, trade wind cumuli, clouds with low liquid water content LWC and cloud optical thickness τ , are poorly implemented in NWP and GCM, by showing a reduced sensitivity on changes in LWC , N , and the droplet effective radius r_{eff} (Bony et al., 2015). As a result, local radiative effects of trade wind cumuli and their natural variability are not sufficiently captured by NWP and GCM. By that, NWP models miss cloud-radiation interactions, which cause large uncertainties in global climate predictions (Bony and Dufresne, 2005).

Within the IFS the cloud droplet effective radius r_{eff} is computed from the LWC , the rain water content (RWC), and climatologies of cloud condensation nuclei (CCN) concentration (ECMWF, 2016b). The actual number of activated cloud droplets N is parameterized from the LWC and the CCN (Martin et al., 1994). Regional effects on small temporal and spatial scales, e.g., advection of aerosol, can not be considered. In nature, enhanced aerosol concentrations are observed in coastal areas, resulting in higher CCN and N with decreased r_{eff} compared to unpolluted maritime air (Wood, 2012). Additionally, the simplified parameterization leads to reduced changes in N and related r_{eff} , and reduced sensitivities in the simulated upward F and α (Bony and Dufresne, 2005). As a result of a fixed or climatology based N , the variability in simulated F is in contradiction to natural fluctuation. Hence, the significance of lower model sensitivity for local radiative effects has to be estimated.

In contrast to the well defined LUT of liquid water clouds, parameterizations of ice clouds suffer from an insufficient representation with respect to ice crystal shape, size, and roughness. These parameterizations and mass-size-relations have not been updated in the last years, although significant shortcomings in the observations were discovered on which the applied parameterizations base (Fu, 1996; Fu et al., 1998a). Current cloud optics parameterizations rely on single case studies, e.g., by Fu (1996); Fu et al. (1998a), with limited representativeness in space and time, and therefore, might not be valid for different atmospheric regimes. In addition, due to various formation mechanisms and aggregation, the resulting shapes differ considerably (Baran, 2004; Voigt et al., 2017). Consequently, the radiative impact of ice particles is not well quantified and poorly parameterized in the simplified Radiative Transfer Simulations (RTS) of NWP (Baran, 2012).

Twomey Effect of Shallow Trade Wind Cumulus

Bony and Dufresne (2005) showed that a significant fraction of the forecast uncertainties in NWP and GCM stem from an inadequate representation of the first aerosol effect (Twomey, 1977), describing the correlation of N and the cloud optical thickness τ or cloud top albedo α . It is most prominent for optically thin, low-level clouds such as developing trade wind cumulus (Platnick and Twomey, 1994; Werner et al., 2014), which are an ubiquitous cloud type in the tropics (Warren et al., 1988; Eastman et al., 2011). Despite their small vertical and horizontal extent, trade wind cumuli can have fractional cloudiness of more than 25 % (Albrecht, 1991) and, therefore, may influence the Earth radiative energy budget significantly (Chertock et al., 1993), which requires better parameterizations in the models to reduce forecast uncertainties.

Cloud Evolution and Cloud Top Icing

An other major issue is the representation of clouds during the initial phase of the cloud life cycle, when clouds are growing and their optical thickness τ is low, e.g., trade wind cumuli. In this stage, clouds undergo several internal processes, e.g., rain formation or phase transitions (Zhang et al., 2013; Herwehe et al., 2014; Khain et al., 2015).

Phase transitions at cloud top (CT) along Warm Conveyor Belts (WCB) influence the cloud radiative properties of a cloud indirect and direct. The indirect effect results from cloud dynamics modifications and changes of the cloud macrophysical properties. When clouds develop and grow in height with time, the CT reaches higher altitudes where lower ambient temperatures are present and the liquid water droplets are triggered to freeze. Turning from liquid water to ice is a diabatic process, which enhances and influences the cloud evolution. Phase transitions are accompanied by release or

consumption of latent heat with significant impact on the cloud structure (Rosenfeld et al., 2008; Tao et al., 2012). Latent heat release increases the internal energy and temperature of an air parcel, resulting in an accelerated upward motion and leading to elevated cloud tops. In case of unstable or conditionally unstable ambient atmospheric conditions this intensified upward motion can generate overshooting CT. Higher CT amplify the radiative cooling due to an increased emission of terrestrial radiation. Martínez-Alvarado et al. (2014) showed that solar radiative cooling is the third most relevant diabatic process responsible for widespread but heterogeneous surface cooling below WCB, which feeds back into the cloud dynamics. To consider for the indirect effect, the cloud dynamics module of NWP requires frequent updates by the radiation scheme, which is not realized in current NWP causing forecast errors (Hogan and Bozzo, 2018).

A direct influence of phase transitions on the radiative effect is caused by the difference between the scattering and absorption properties of liquid water droplets and complex shaped ice crystals. Simulations from Ehrlich (2009) and observations by Wendisch and Brenguier (2013) show, that icing at CT significantly increases α . These effects are most prominent for cloud optical thickness of $\tau < 50$ at the beginning of their lifetime. This implies that it is of importance for the cloud top radiative forcing at which stage of the cloud life cycle phase transitions and icing at CT take place.

1.3 Model Validation

The aforementioned challenges and the urgent requirement for improved cloud representation in NWP and GCM, for better forecast quality as well as error quantification, enforces the need for simultaneous model evaluation and investigation of cloud microphysical and radiative properties. This can be done either by: (i) inter-comparison with other models (Klocke and Rodwell, 2014) or by (ii) directly comparing the forecasts with appropriate observations (Bozzo et al., 2014).

The evaluation of the IFS ecRad module by using other sophisticated RTS (approach i), e.g., the library for Radiative transfer (libRadtran), enables to directly compare both radiation schemes. If ecRad and libRadtran are initialized with the same input, differences among the simulations only emerge from the models deviating optics parameterizations and can be clearly quantified. libRadtran, as a stand-alone RTS, allows to calculate vertical profiles of spectral irradiance covering the entire solar wavelength range. The library includes 12 different RT solvers, ranging from a two-stream solver, similar to ecRad, to more sophisticated ones with higher orders of streams. Microphysical properties of liquid water clouds base on pre-calculated Mie tables with one nanometer spectral resolution. In case of ice water clouds, a set of ice optical parameterizations can be selected, covering different ice crystal habits, e.g., columns, hexagonal plates, and droxtals. Ice crystal surface roughness ranges from smooth to severe, following Fu (1996), Fu et al. (1998b), and Baum et al. (2005a). All these options, make libRadtran a versatile tool for RTS. Detailed information on libRadtran and its application are given in Mayer and Kylling (2005), Emde et al. (2016), and Mayer et al. (2017). In Tab. 1.1 the characteristic features and differences of ecRad and libRadtran are listed.

To evaluate the model by observations (approach ii), ground-based lidar or microwave radiometer observations are used. Nuijens et al. (2015) compared observations and simulations of trade wind cumuli, and found a reasonable agreement between the simulated cloud fields and the observed cloud structures and their variability. In contrast, noticeable shortcomings in fractional cloud cover, cloud overlap assumption, and the resulting total cloud cover were indicated.

In case of the ECMWF and from a global perspective, a common approach is to compare the simulated cloud top albedo α with observations from the Clouds and the Earth's Radiant Energy System (CERES) satellite, e.g., done by Ahlgrimm and Forbes (2014) or Forbes and Ahlgrimm (2014). Using CERES data allows to check the overall global performance of the IFS forecast and ecRad. However, the observation geometry of the satellite's instrument and measuring radiances requires an approximated Hemispherical Directional Reflectance Function to derive α , which introduces potential biases in α (Su et al., 2005). In addition, simulated and observed α might agree, whereby spatial averaging will mask local biases. Such smoothing effects of the observations are reported for maritime stratocumulus fields along the west coasts of the continents. In these regions local radiative effects are expected, which are poorly captured by the IFS, but can not be resolved with CERES (Forbes, 2010). Further on, the CERES satellite observations are limited to broadband radiances, which excludes the possibility to evaluate the spectral representation of the simulated clouds.

Table 1.1: List of characteristic features of ecRad and libRadtran.

Variable	ecRad	libRadtran
Spectral resolution	14 bands 200 - 3846 nm (RRTM-G)	< 1 nm
Number of Streams	2	2 - 16
Gas optics	Monochromatic, RRTM-G (Mlawer et al., 1997)	LOWTRAN (Ricchiazzi et al., 1998), REPTRAN (Buehler et al. (2010), Gasteiger et al. (2014))
Liquid optics	SOCRATES Edwards and Slingo (1996), Slingo (1989), Monochromatic	Mie tables
Ice optics	Fu (1996), Fu et al. (1998a), Yi et al. (2013)	Baum et al. (2005a), Fu (1996), Fu et al. (1998a)
Ice crystal shapes	Solid columns	Solid columns, Mixtures, Aggregates
Solver	Homogeneous, McICA (Pincus et al., 2003), Tripleclouds, SPARTACUS (Hogan and Bozzo, 2018)	fdisort2 (Stamnes et al., 2000), twostr (Kylling et al., 2005), et al. see Mayer et al. (2017)
3D radiative transfer	sub grid-box parameterization	no
Cloud overlap assumptions	EXP-EXP, MAX-RAN, EXP-RAN	rand, maxrand, max, off
Application	Numerical Weather Prediction, Global Climate Models	Investigate radiative transfer in versatile applications, Benchmark

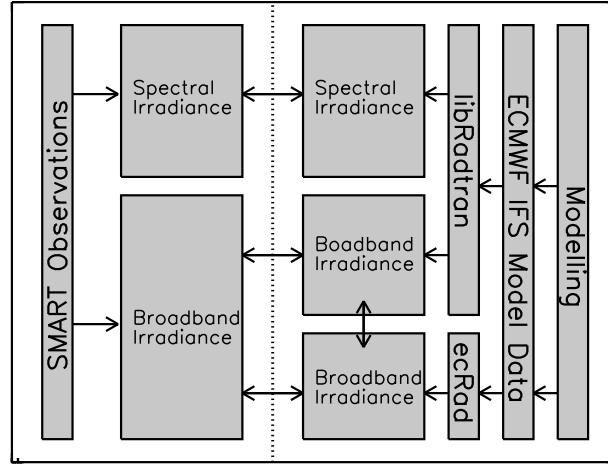


Figure 1.1: Schematic of the synergetic comparison strategy by combining observations and benchmark models for evaluation of Numerical Weather Prediction Models.

1.4 Retrieval of Cloud Optical Properties

As an alternative to in-situ measurements, remote sensing can be applied for model validation. This can be problematic as required retrieval assumptions introduce additional uncertainties. Remote sensing of cloud properties, like τ and r_{eff} , are questionable in case of ice clouds and complex cloud scenarios, like multi-layer clouds. In most of the applied forward simulations, homogeneous cloud-layers are assumed, whereby such simplifications and assumptions inevitably lead to uncertain retrieval results (Thelen and Edwards, 2012).

Despite the problems of cloud optical properties retrievals, e.g., applied assumptions on ice particle shape, remote sensing is appropriate in certain situations, e.g., homogeneous clouds structures, or even required when in-situ measurements of cloud microphysical properties are not accessible.

Within the last years, established remote sensing methods were advanced, e.g., new sensors with higher spatial and spectral resolution as well as new techniques and synergistic approaches to combine information from radar and lidar measurements (Delanoe et al., 2013). Further on, the usability of ground-based instruments has been transferred to airborne applications operated on aircraft, reducing the required retrieval assumptions and increasing the confidence in the retrieved properties.

While airborne spectroradiometers allow to obtain a detailed view of CT properties, cloud radar and microwave radiometer give insight in the vertical profile of clouds, even at cloud base. The additional radar and microwave measurements offer the possibility to derive and compare full vertical cloud profiles with model data.

Despite some first promising approaches of combined radar-lidar retrievals by Delanoe et al. (2013), synergetic methods by implementing different instruments are still sparse. In spite of that, current advanced cloud remote sensing of CT properties from airborne instruments, in combination with direct comparison of simulated and measured F above clouds, provides a prospective method for detailed NWP evaluation.

1.5 Hypothesis

Combining both model evaluation approaches, by utilizing two different RTS on basis of the same IFS AD and spectroradiometer measurements of F , differences between simulated and observed F are separated for errors in IFS AD and the RTS by ecRad.

Figure 1.1 shows a schematic of the synergetic comparison strategy. SMART provides observations of spectral and broadband measurements of F (Fig. 1.1 left). The simulations (Fig. 1.1 right) of ecRad and libRadtran (benchmark) utilize the same IFS AD. Simulated broadband F are compared among both models to identify errors, which solely emerge from the RTS. In a next step broadband F from the models are compared with the SMART measurements to identify potential deficiencies

in cloud representation in the IFS AD. In addition, the comparison of spectrally resolved F from SMART and libRadtran allows to investigate the spectral accuracy of the optical parameterizations but also to pinpoint weaknesses in the IFS AD, which influence the spectrum differently, e.g., liquid water content or cloud droplet size.

The aim of this work is to validate the RTS ecRad with simulations of spectral upward and downward F by libRadtran following the along-track measurements of F performed with the High Altitude and Long Range Research Aircraft (HALO) during flights of two measurement campaigns and leads to the hypothesis, that:

Airborne in-situ and remote sensing observations, in combination with simulations of spectral upward and downward irradiance, can be used to separate and quantify uncertainties in the radiation scheme of a numerical weather prediction model and the analysis data.

To address this hypothesis the following questions will be answered in the thesis:

- How well are ice topped clouds represented by the current optical ice parameterization of ecRad?
- How well are mid-latitude and tropical low-level liquid water clouds represented in the IFS AD?
- How does total cloud cover, liquid water content, cloud droplet number concentration, and cloud heterogeneity influence the radiative forcing of trade wind cumuli?

1.6 Outline

This introduction is followed by Chapter 2 where the basic radiative and microphysical quantities are defined, and the utilized radiative transfer modules are presented. Subsequently, the radiation measurements, the calibration procedure, and the field campaigns are described in Chapter 3. In Chapter 4 a developed synergetic cloud droplet number concentration retrieval is presented. In Chapter 5 the simulation setup is explained, which was used for the radiation calculations. In course of that, uncertainties of the ecRad simulations are estimated and the general representativeness of the observations with respect to the radiation field is assessed. Subsequently, the sensitivity of ecRad and libRadtran on shallow trade wind cumuli is compared and afterwards the along-track simulations are compared with observations of two field campaigns. The conclusion of the thesis is given in Chapter 6, shortly summarizing this thesis.

2 Fundamentals

The incident light from the sun, reaching the top of atmosphere (TOA), undergoes various interactions with the constituents of the Earth's atmosphere on its way to the surface. To quantify and describe these effects on the radiative transfer (RT), fundamental radiometric properties (section 2.1) as well as the cloud optical (section 2.2) and microphysical quantities (section 2.4) have been defined following the work of Petty (2006) and Wendisch and Yang (2012). The radiative transfer equation (RTE) and according numerical solution models for the RTE are described in section 2.3. Section 2.5 introduces the IFS radiation module ecRad and in section 2.6 the library for Radiative transfer (libRadtran) is outlined. This is followed by section 2.7 describing the concept of the Independent Pixel Approximation.

2.1 Radiative Quantities

The basic quantity of all RT is the spectral radiant energy flux Φ_λ , which is given by the radiant energy E_{rad} passing through an infinitesimal area element d^2A in a certain time interval $t + dt$ for a given wavelength (λ) range $\lambda + d\lambda$. It is denoted by:

$$\Phi_\lambda = \frac{d^2 E_{\text{rad}}}{dt d\lambda}. \quad (2.1)$$

$\Phi_\lambda(t)$ defines the power of radiant energy at the time t and carries the units of $\text{J s}^{-1} \text{nm}^{-1}$, which can be expressed as W nm^{-1} . Relating Φ_λ to the corresponding area element d^2A results in the spectral radiant energy flux density F_λ , which is defined as:

$$F_\lambda = \frac{d^2 \Phi_\lambda}{d^2 A} = \frac{d^4 E_{\text{rad}}}{d^2 A dt d\lambda}. \quad (2.2)$$

F_λ , also called spectral irradiance ($\text{W m}^{-2} \text{nm}^{-1}$) and quantifies the spectral radiant energy flux through the unit area from the complete hemisphere. For atmospheric applications, the area element d^2A is considered to be horizontally aligned, which means that the orientation of the unit vector (\hat{n}), which is perpendicular to d^2A , is pointing in zenith direction. Conversely, E_{rad} within a solid angle element $d^2\Omega$, which is pointed in the direction of propagation \hat{s} , is quantified by the spectral radiance $I_\lambda(\hat{s})$ as follows:

$$I_\lambda(\hat{s}) = \frac{d^4 \Phi_\lambda}{\cos \theta d^2 A d^2 \Omega} = \frac{d^6 E_{\text{rad}}}{dt d\lambda \cos \theta d^2 A d^2 \Omega}. \quad (2.3)$$

The spectral radiance is given in units of $\text{W m}^{-2} \text{nm}^{-1} \text{sr}^{-1}$. The geometry for the definition of $I_\lambda(\hat{s})$ is illustrated in Figure 2.1. The solid angle element $d^2\Omega$ is defined by the zenith angle θ and the azimuth angle φ with:

$$d^2\Omega = \sin \theta d\theta d\varphi, \quad (2.4)$$

and has the unit of sr. In this definition of the radiance the respective area element is the projection of d^2A onto the perpendicular plane to the direction of propagation \hat{s} by multiplying with the cosine of θ and given by:

$$d^2A_\perp = \cos \theta \cdot d^2A. \quad (2.5)$$

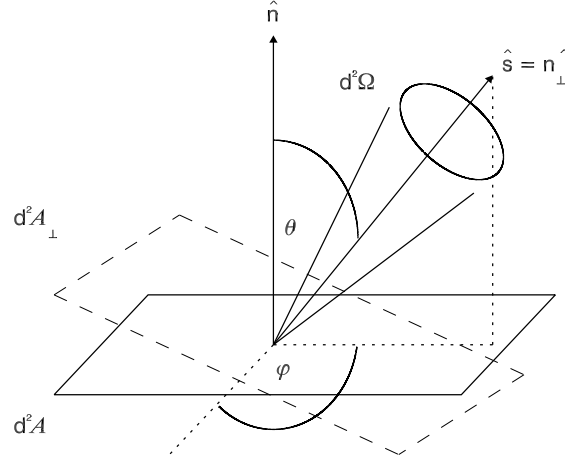


Figure 2.1: Illustration of the definition of radiance.

By integrating $I_\lambda(\hat{s})$ over all solid angles $d^2\Omega$ of the hemisphere, results in F_λ :

$$F_\lambda = \iint_{2\pi} I_\lambda(\hat{s}) \cdot \cos \theta \, d^2\Omega = \int_0^{2\pi} \int_0^\pi I_\lambda(\theta, \varphi) \cdot \cos \theta \cdot \sin \theta \, d\theta \, d\varphi. \quad (2.6)$$

From the restriction that the area element d^2A is horizontally oriented, F_λ corresponds to the upper and lower hemisphere and the respective upward irradiance F_λ^\uparrow and downward irradiance F_λ^\downarrow are obtained by:

$$F_\lambda^\downarrow = \int_0^{2\pi} \int_0^{\pi/2} I_\lambda(\theta, \varphi) \cdot \cos \theta \cdot \sin \theta \, d\theta \, d\varphi \quad (2.7)$$

$$F_\lambda^\uparrow = - \int_0^{2\pi} \int_{\pi/2}^\pi I_\lambda(\theta, \varphi) \cdot \cos \theta \cdot \sin \theta \, d\theta \, d\varphi. \quad (2.8)$$

Similarly, the radiance can be directed upward and downward looking to $I_\lambda^\uparrow(\hat{s})$ and $I_\lambda^\downarrow(\hat{s})$. Within the Earth's atmosphere, F_λ^\downarrow is determined by the position of the Sun. The angles between the zenith and the sun position are given by the solar zenith angle θ_0 and the solar azimuth angle φ_0 . Because F_λ^\downarrow has a direct and diffuse component, the radiation field is anisotropic, while F_λ^\uparrow is assumed to have a diffuse component only. In case of an isotropic radiation field, the radiance is independent of the orientation of \hat{s} and from the integration over all solid angles it follows:

$$F_{\lambda, \text{iso}} = \pi \, \text{sr} \cdot I_{\lambda, \text{iso}}. \quad (2.9)$$

2.2 Cloud Optical Properties

The interaction of radiation and single particles within the atmosphere, e.g., gas molecules, cloud particles, and aerosol particles, result in three different process called scattering, absorption, and emission. To describe the cloud optical properties, several quantities have been introduced and are shortly described in the following.

Extinction and scattering processes of radiation within the atmosphere can be characterized by the extinction cross section C_{ext} , the single-scattering albedo $\tilde{\omega}$, and the scattering phase function

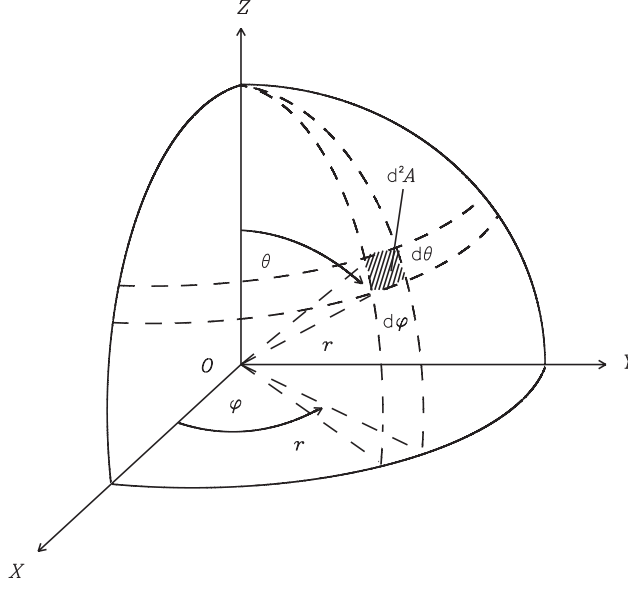


Figure 2.2: Definition of the solid angles given in polar coordinates (adapted from Wendisch and Yang (2012)). Figure 2.2 illustrates the definition of the solid angle by ϑ , μ , and φ .

\mathcal{P} . They are defined by the mass- or cross-sectional area, the spectral complex index of refraction \tilde{n} (depending on chemical composition), the particle shape, size, and orientation. For spherical liquid water droplets, Mie-theory can be applied, for which an analytical solution for the three quantities can be found (Mie, 1908; Bohren and Huffman, 1998). In contrast, the single-scattering properties of non-spheric particles, like ice crystals or aerosol particles, no general analytical solutions can be obtained and numerical methods have to be applied. Spectral single-scattering properties of different ice crystal shapes and sizes are published by Fu (1996); Fu et al. (1998a), Baum et al. (2005a,b), Yang et al. (2005), Baum et al. (2007), and others.

The extinction cross section C_{ext} in units of m^2 characterizes how effective an individual particle attenuates radiation. It is defined by the ratio of the extinct radiant energy flux Φ_{ext} relative to the incident F_{inc} :

$$C_{\text{ext}} = \frac{\Phi_{\text{ext}}}{F_{\text{inc}}}. \quad (2.10)$$

It can also be defined by the sum of the scattering cross section C_{sca} and the absorption cross section C_{abs} :

$$C_{\text{ext}} = C_{\text{sca}} + C_{\text{abs}}. \quad (2.11)$$

The probability of atmospheric radiation being absorbed or scattered by a particle is given by the dimensionless particle single-scattering albedo $\tilde{\omega}$, which is determined from the optical cross sections via:

$$\tilde{\omega} = \frac{C_{\text{sca}}}{C_{\text{sca}} + C_{\text{abs}}} = \frac{C_{\text{sca}}}{C_{\text{ext}}}. \quad (2.12)$$

$\tilde{\omega}$ can range between 0 and 1, where values of 1 indicate complete absorption of radiation by the cloud particle and values of 0 represent pure scattering, also called elastic ($\lambda_{\text{inc}} = \lambda_{\text{sca}}$) scattering. Together, C_{abs} and $\tilde{\omega}$ define the probability of absorption and are mostly determined the imaginary part of the refractive index \tilde{n}_i .

The angular distribution of scattered radiation by a particle is given by the dimensionless scattering phase function \mathcal{P} as a function of the incident direction (μ_{inc}, μ) to all possible directions (μ, φ) , with the substitution $\mu = \cos \theta$. \mathcal{P} is normalized to 4π :

$$\int_0^{2\pi} \int_{-1}^1 \mathcal{P}([\mu_{\text{inc}}, \mu]) d\mu d\varphi = 4\pi \text{ sr}. \quad (2.13)$$

For an azimuthal symmetric phase function, which is the case for liquid cloud droplet sizes, the relation

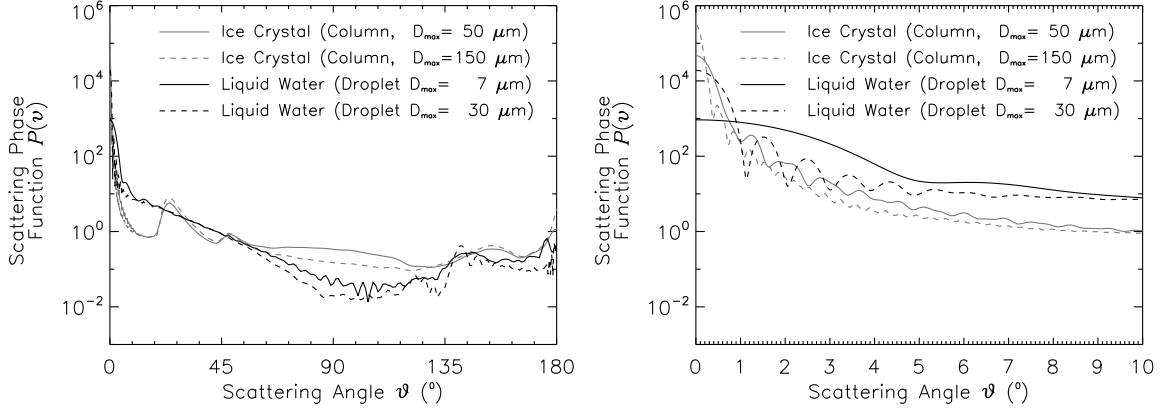


Figure 2.3: Scattering phase function \mathcal{P} of spherical liquid water droplets (black) and columnar ice crystal (gray) for two different sizes representing the typical dimension range, respectively. Left picture shows \mathcal{P} for the all scattering angles ϑ and right picture shows a close up of \mathcal{P} with ϑ between 0° and 10° (adapted from Wendisch and Yang (2012)).

between the incident and scattered direction in the scattering plane can be described by the scattering angle ϑ :

$$\cos \vartheta = \mu_{\text{sca}} \cdot \mu_{\text{inc}} + \sqrt{1 - \mu_{\text{sca}}^2} \cdot \sqrt{1 - \mu_{\text{inc}}^2}. \quad (2.14)$$

Figure 2.3 illustrates examples of the scattering phase functions \mathcal{P} for two cloud droplets and two ice crystals with columnar shape. Differences in the angular distribution arise from the different shapes and sizes. \mathcal{P} of solid columns is smoother than that of the water droplets, which comes from the azimuthal averaging in case of the ice crystals and the larger size of the ice particle. The irregular pattern of \mathcal{P} of the liquid water droplets results from the oscillation of the Mie solutions. Phase functions of ice crystals are characterized by a strong and narrow forward peak, while for liquid water droplets the forward peak is less pronounced. The intensity of the forward peak becomes larger for increasing particle size. In case of regularly shaped ice crystals, a large fraction of the incident radiation will pass through the particle without being scattered ($\vartheta = 0^\circ$). This process is called Delta-transmission (Takano and Liou, 1989). It was found that the Delta-Eddington-Approximation represents the original \mathcal{P} sufficiently well for application in NWP (Joseph et al., 1976).

The interaction of radiation with non-spherical particles, like ice crystals, is much more complex compared to spherical cloud droplets, and different approaches to describe the influence of a single particle are developed. The methods can be separated in three groups of analytical solutions, numerical solutions, and simplified approximations. In the last decades several papers, described these different approaches, e.g., Takano and Liou (1989), Takano and Liou (1995), Yang and Liou (1996), Macke et al. (1998), and Klotzsche and Macke (2006). The analytic methods try to solve Maxwell's equations, which is possible for specific shapes only. For other shapes and large particles, when the particle size is much larger than λ of the incident light, geometric optics can be applied, where radiation is regarded as a bundle of collimated rays. In combination with ray-tracing techniques, the path of individual photons through the particle is simulated to derive $\mathcal{P}(\vartheta)$. Alternatively, $\mathcal{P}(\vartheta)$ can be approximated, e.g., by the Delta-Eddington-approximation. Finally, $\mathcal{P}(\vartheta)$ is determined for a range of particle sizes and available in pre-calculated look-up-tables, which are used to reduce the computational effort, e.g., for NWP. The phase function can be further parameterized with respect to particle size distribution and the liquid water content.

Figure 2.4a displays $\tilde{\omega}$ as a function of wavelength for columnar ice crystals with sizes of 20, 40, and 60 μm following Fu (1996) and Baum et al. (2007). In Fig. 2.4b the absolute differences in $\tilde{\omega}$ between the two parameterizations are shown. Around 1450 and 1900 nm wavelength, liquid water and ice show pronounced absorption features, depending on the diameter of the particles. In general, $\tilde{\omega}$ decreases

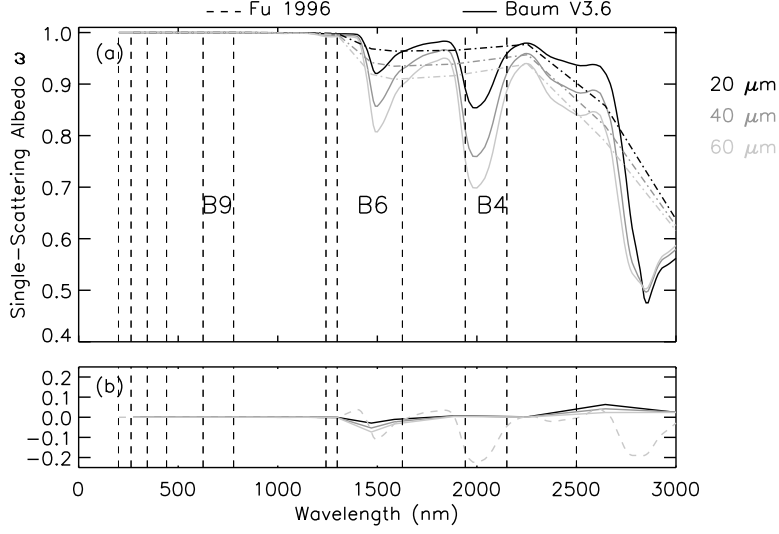


Figure 2.4: Upper panel: Spectral single-scattering albedo $\tilde{\omega}$ for columnar ice crystals with sizes of 20, 40, and 60 μm between 0 and 3000 nm basing on Fu (1996) (dashed) and Baum et al. (2007) (solid). Lower panel: Absolute differences in $\tilde{\omega}$ between both parameterizations. Dashed vertical lines indicate the spectral resolution of the radiation model of the Integrated Forecast System.

with increasing droplet size. The Baum parameterization shows a significant sensitivity of $\tilde{\omega}$ on the wavelength, e.g., between 1400 and 1500 nm as well as between 1900 and 2100 nm, compared to $\tilde{\omega}$ from the Fu parameterization. The deviations due to the Fu parameterization were already quantified by Fu (1996) and are in the range of $\pm 1.2\%$ for reflection and $\pm 2.9\%$ for absorption of the total incoming solar radiation. Despite the low deviation with respect to the total irradiance, absorption of solar radiation by ice clouds in the near-infrared wavelength range is of importance, as it controls the heating of the cloud and the resulting cloud development by diabatic processes.

The asymmetry factor g , of the phase function of an individual particle is estimated from the angular distribution of the scattered radiation. It is definite by

$$g = \int_{4\pi} \int_{4\pi} p(\vartheta) \cdot \cos \vartheta d^2\Omega = \frac{1}{2} \cdot \int_{-1}^1 \cos \vartheta \cdot \mathcal{P}(\cos \vartheta) d \cos \vartheta \quad (2.15)$$

where the phase function is integrated over all solid angles. In this case it is assumed that the phase function is axially symmetric. Evaluating Eq. (2.15), pure forward scattering ($\vartheta = 0^\circ$) leads to an asymmetry factor $g = 1$, whereby pure backward scattering ($\vartheta = 180^\circ$) results in $g = -1$. For a symmetric distribution of the phase function, g vanishes.

2.3 Radiative Transfer Equation

The radiative transfer (RT) is determined by the single scattering properties b_{ext} , $\tilde{\omega}$, and \mathcal{P} . Along a path through the atmosphere, the attenuation of the direct solar radiance I_{dir} is characterized by the law of Beer, Lambert, Bouguer:

$$I_{\text{dir}}(\tau, \mu_0, \varphi_0) = \frac{F_0}{4\pi \text{ sr}} \cdot \exp\left(-\frac{\tau}{\mu_0}\right), \quad (2.16)$$

with the optical thickness τ as a vertical coordinate and the cosine of the solar zenith angle $\mu_0 = \cos \theta_0$. The incident extraterrestrial irradiance F_0 at the top of the atmosphere (TOA), is attenuated exponentially along τ . In case of $\mu_0 = 0.64$ and cirrus clouds with $\tau = 5$ the transmitted fraction of direct solar

radiance through the cloud in below 0.05 %. As a result, radiation which penetrates the cloud, can be regarded as diffuse solar radiance I_{diff} only and in the spectral range from $\lambda = 0.2 - 5 \mu\text{m}$ thermal emission can be neglected. Under this assumptions the 1D RTE for plane-parallel and horizontally homogeneous atmospheric layers can be written as

$$\mu \frac{dI_{\text{diff}}(\tau, \mu, \varphi)}{d\tau} = I_{\text{diff}} - (J_{\text{dir}} + J_{\text{diff}}). \quad (2.17)$$

It was first introduced by Chandrasekhar (1950). The propagation direction of I_{diff} is represented by μ and φ . The two source terms $J_{\text{dir}} + J_{\text{diff}}$ characterize the radiation scattered into the viewing direction. J_{dir} is the single scattering term of the direct solar radiation, which is scattered into the viewing direction:

$$J_{\text{dir}} = \frac{\tilde{\omega}(\tau)}{4\pi \text{sr}} \cdot F_0 \cdot \exp\left(-\frac{\tau}{\mu_0}\right) \cdot \mathcal{P}([\mu_{\text{inc}}, \mu]). \quad (2.18)$$

Incoming solar radiation is attenuated described by the law of Beer, Lambert, Bouguer. The attenuated radiation is scattered into the viewing direction, depending on the amount of absorption ($\tilde{\omega}$) and the scattering phase function \mathcal{P} . J_{diff} describes the amount if diffuse radiation, which is scattered into the viewing direction:

$$J_{\text{diff}} = \frac{\tilde{\omega}(\tau)}{4\pi \text{sr}} \int_0^{2\pi} \int_{-1}^1 I_{\text{diff}}(\tau, \mu_{\text{inc}}, \varphi_{\text{inc}}) \cdot \mathcal{P}(\tau, [\mu_{\text{inc}}, \mu]) d\mu_{\text{inc}} d\varphi_{\text{inc}}. \quad (2.19)$$

2.4 Microphysical Properties

The microphysical properties of a cloud are given by the number particle size distribution (PSD), describing the number of cloud droplets N within a certain bin size dD , and its moments k , which are defined by:

$$M^k = \int_0^\infty m^k \cdot N(D) dD. \quad k \in \mathbb{N} \quad (2.20)$$

The total particle number concentration N_{tot} , the zeroth moment of the PSD ($k=0$), is obtained by integrating over particle sizes D of the PSD $n = dN/dD$:

$$N_{\text{tot}} = \int_0^\infty n(D') dN \quad (2.21)$$

with the unit m^{-3} . The amount of condensed liquid water in a cloud volume of 1 m^3 is proportional to the third moment of the PSD and described by the liquid water content LWC :

$$LWC = \frac{4}{3} \cdot \pi \cdot \varrho_w \cdot \int \left(\frac{D'}{2}\right)^3 \cdot \frac{dN}{dD'}(D') dD', \quad (2.22)$$

with the density of liquid water ϱ_w . The LWC is given in units of kg m^{-3} .

Assuming an adiabatic cloud, the LWC increases linearly with height and the liquid water path LWP is determined by integrating LWC from cloud base (CB) to cloud top (CT):

$$LWP = \int_{\text{CB}}^{\text{CT}} LWC(z) dz = \frac{4}{3} \cdot \pi \cdot \rho_w \cdot \int_{\text{CB}}^{\text{CT}} N(z) \cdot r_{\text{vol}}^3(z) dz \quad (2.23)$$

with the density of liquid water ρ_w , the geometric height z , and the mean-volume radius r_{vol} . LWP is obtained in units of kg m^{-2} . Accordingly, the ice water content IWC and ice water path IWP of

a ice clouds are quantified by:

$$IWC = \varrho_i \cdot \int V_D(D') \cdot \frac{dN}{dD'}(D') dD' \quad (2.24)$$

$$IWP = \int_{CB}^{CT} IWC(z) dz. \quad (2.25)$$

In-situ observations showed, that clouds are influenced by entrainment of drier surrounding air (Reid et al., 1999; Wendisch and Keil, 1999), leading to subsaturation and deviations from the adiabatic lapse rate of LWC . From the cloud LWP and estimates of cloud geometric thickness dz the lapse rate Γ_{calc} is derived by:

$$\Gamma_{calc} = \frac{2 \cdot LWP}{dz^2}. \quad (2.26)$$

The radiative effective droplet radius $r_{eff,liq}$ in units of μm is defined as the ratio of the third to the second moment of the PSD, representing the ratio of the cloud particle volume to its surface area. Within an ensemble of cloud particles r_{eff} is calculated as:

$$r_{eff} = \frac{1 \int D'^3 dN/dD'(D') dD'}{2 \int D'^2 dN/dD'(D') dD'}. \quad (2.27)$$

The characterization of r_{eff} becomes of particular importance for ice-crystals, as different definitions exist, depending on how the size of a non-spherical particle is defined. Following the general approach by Yang et al. (2000) and Key et al. (2002), r_{eff} is defined by the maximum dimension of an ice crystal D_{max} , its volume V_D , and its projected area A_D . V_D and A_D are derived from calculating the diameter of a sphere with the same volume and surface area as the regarded ice particle (Grenfell and Warren, 1999; Yang et al., 2000). After Yang et al. (2000) the r_{eff} for ice particles is defined as:

$$r_{eff} = \frac{3 \int V_D(D') \cdot dN/dD'(D') dD'}{4 \int A_D(D') \cdot dN/dD'(D') dD'}. \quad (2.28)$$

Alternatively, Fu (1996) defines r_{eff} by

$$D_{eff,Fu} = \frac{\int W^2 L \cdot n(L') dL'}{\int (W \cdot L' + \sqrt{3}/4 \cdot W^2) \cdot n(L') dL'} dL' \quad (2.29)$$

with the size distribution $n(L)$, the width W , and the length L of the crystal. It has to be emphasized that this definition is valid for hexagonal columns only. Other ice crystal shapes are not considered. The effective size of a particle defined by Eq. (2.28) and Eq. (2.29) deviate and are related by:

$$D_{eff,Fu} = \frac{2 \cdot \sqrt{3}}{3} \cdot r_{eff} \quad (2.30)$$

in case of ice columns.

Following Hansen and Travis (1974) and Stephens (1978) the cloud optical thickness τ of liquid water clouds is related to the *LWP*, N , and r_{eff} by:

$$\tau = \int_{\text{CB}}^{\text{CT}} \sigma_{\text{ext}} dz = \int_{\text{CB}}^{\text{CT}} \pi \int_0^\infty Q_{\text{ext}}(x) \cdot N(r, z) \cdot r^2 dr dz = \int_{\text{CB}}^{\text{CT}} \pi \cdot Q_{\text{ext}}(\bar{x}) \cdot N(z) \cdot r_{\text{srf}}^2 dz \quad (2.31)$$

with the extinction coefficient σ_{ext} , the extinction efficiency factor Q_{ext} which is approximately 2 for cloud droplets in the solar wavelength range, and the size parameter $x = (2 \cdot \pi \cdot r)/\lambda$. According to Martin et al. (1994), the cloud droplet effective radius r_{eff} correlates with the mean-surface radius r_{srf} and the mean-volume radius r_{vol} of the droplet size distribution given by:

$$k = \left(\frac{r_{\text{vol}}}{r_{\text{eff}}} \right)^3 = \left(\frac{r_{\text{srf}}^3}{r_{\text{vol}}^2} \right)^6. \quad (2.32)$$

This relation depends on the shape of the PSD and is referred as the k -parameter (Martin et al., 1994). Using k as the distribution shape factor, r_{srf} and r_{vol} in Eq. (2.23) and Eq. (2.31) are replaced by r_{eff} leading to:

$$\tau = \frac{3 \cdot \int_{\text{CB}}^{\text{CT}} LWC(z) \cdot dz}{2 \cdot \rho_w \cdot r_{\text{eff}}}. \quad (2.33)$$

For adiabatic clouds, Eq. (2.33) can be solved analytically, which results in a relation that directly links *LWP* to τ and r_{eff} :

$$LWP = \frac{5}{9} \cdot \rho_w \cdot \tau \cdot r_{\text{eff}} \quad (2.34)$$

following Brenguier et al. (2000).

2.5 Radiative Transfer Module 'ecRad'

ecRad is a radiative transfer package including a one-dimensional RTS, developed by the European Centre for Medium Range Forecast (ECMWF) to calculate vertical profiles of solar (200 to 3846 nm) and terrestrial (3.1 to 1000 μm) irradiances F . It is operational since IFS Cycle 43R3 in 2017, replacing the previous McRad scheme, and is part of the IFS weather forecast model. ecRad is programmed in a modular design, which allows to change between different RTS and parameterizations for cloud-, gas-, and aerosol-optics. The individual components and the resulting interchangeability enables to adapt and use ecRad in other NWP, too. A complete scientific overview of ecRad is given by Hogan and Bozzo (2018). The following description of the ecRad specifications are valid for release Cy43r3 (Hogan and Bozzo, 2018).

ecRad provides four different RTS to calculate profiles of F , called homogeneous, McICA (PinCUS et al., 2003), Tripleclouds (Shonk and Hogan, 2008), and SPARTACUS (Hogan et al., 2016). These solvers treat sub-cloud structures in different ways. While McICA is based on the Monte-Carlo method, Tripleclouds performs 2D simulations, and SPARTACUS is the first operational RTS implementing 3D radiative transfer parameterizations within a grid-box.

The individual components of ecRad are called by the main program of ecRad successively. Figure 2.5 shows a schematic of the modular design of ecRad and the data-flow between the four components. Radiative fluxes are calculated in the following order: The gas optics component calculates the optical properties of the gases at each spectral interval, based on the wavelength grouping of the rapid radiative transfer model for Global Climate Models (RRTM-G) (Mlawer et al., 1997). Additionally, the spectral Planck function is applied and the incoming solar radiation at TOA is calculated from the given solar constant as a function of the solar zenith angle. The resulting fluxes are handed over to the aerosol optics component, where the radiative contribution of aerosol is added to the simulated fluxes. The output from the combined cloud- and aerosol optics part is referred as the cloud-free optical properties of the grid-box. The cloud optical component is calculated for the grouped 14 solar and 16 thermal-infrared spectral bands of ecRad. Within the cloud optics module, the grid-box is treated as entirely cloud covered for the calculations and the radiative contribution of clouds is added to the RTS. In the next step the solver routine merges cloud-free and cloud optical properties under consideration of the grid-box cloud fraction and the selected cloud overlap assumption (COA). Flux

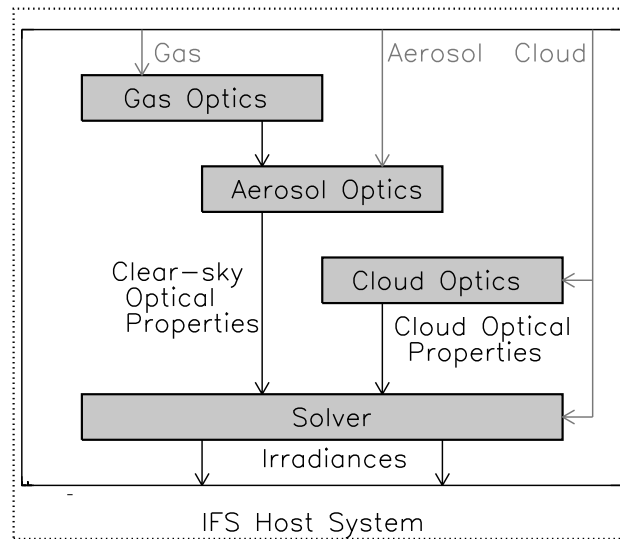


Figure 2.5: Schematic of the stepwise internal radiation calculations of ecRad by the individual modules. Solid arrows indicate calculated optical properties and irradiances. (Adapted from Hogan et al. (2017))

calculations are performed for each model level of the atmospheric column.

2.5.1 ecRad Model Atmosphere and Spectral Bands

Radiation calculations are an expensive part of NWP models in terms of their computational cost. Therefore, simplifications are developed utilizing spectral bands, which base are based on the 'van de Hulst, Curtis, Godson approximation', but are known to be inaccurate for some gases, particularly for ozone (Goody et al., 1989). Potential errors stem from atmospheric pressure broadening, which becomes pronounced in cases of multiple scattering. To overcome this problem, the correlated- k method was developed by Lacis and Oinas (1991). It is a numerical procedure, which uses groups of the absorption coefficient k_{abs} , sorted by absorption strength for distinctive spectral intervals. This requires less spectral points for the RTS compared to spectrally high resolving line-by-line models.

On the basis of the correlated- k method, Mlawer et al. (1997) developed a rapid radiative transfer model (RRTM) designed for general studies of atmospheric radiative transfer and for the application in NWP. The purpose of RRTMs is to parameterize line-by-line calculations, but remaining consistent with the spectrally high resolved line-by-line models. Various types of RRTMs are developed and provided by Atmospheric and Environmental Research, Inc. (AER, Inc.)¹.

¹http://rtweb.aer.com/rrtm_frame.html

Table 2.1: List of spectral bands of the ecRad scheme for the shortwave wavelength range and characteristic absorbers.

Band number	Wavelength (nm)	Wavenumber (cm^{-1})	Characteristic absorbers
1	3077 - 3846	2600 - 3250	H ₂ O, CH ₄
2	2500 - 3076	3250 - 4000	H ₂ O, CO ₂
3	2150 - 2500	4000 - 4650	H ₂ O, CH ₄
4	1942 - 2150	4650 - 5150	H ₂ O, CO ₂
5	1626 - 1941	5150 - 6150	H ₂ O, CH ₄
6	1299 - 1625	6150 - 7700	H ₂ O, CO ₂
7	1242 - 1298	7700 - 8050	H ₂ O, O ₂
8	778 - 1241	8050 - 12850	H ₂ O
9	625 - 777	12850 - 16000	H ₂ O, O ₂
10	442 - 624	16000 - 22650	H ₂ O
11	345 - 442	22650 - 29000	
12	263 - 344	29000 - 38000	O ₃
13	200 - 262	38000 - 50000	O ₃ , O ₂
14	3846 - 12195	820-2600	

The RRTM is most accurate compared to line-by-line results for single column calculations. An improved version is the RRTM-G with increased efficiency and a minimal loss of accuracy. The RRTM-G is implemented in several GCMs, like ECHAM5 of the Max Planck Institute Hamburg (MPI) and the Community Atmosphere Model (CAM5) of the National Center for Atmospheric Research (NCAR). It is also applied in NWP, like the IFS of ECMWF and the Non-hydrostatic Meso-scale atmospheric model (Meso-NH) of the French National Meteorological Service (Meteo-France). RRTM-G considers absorption by H₂O, CO₂, O₃, NO, CH₄, CFC – X, and CCl₄. The spectral absorption features of these gases requires the subdivision of the visible and thermal-infrared spectra into a series of spectral bands implemented into ecRad. The key absorber in each band dominates the characteristic of the individual band, while minor contributing trace gases have a smaller influence.

The wavelength in RRTM-G are divided in a solar-infrared (200 nm - 12200 nm) and a thermal-infrared (3.08 μm - 1000 μm) part. In the following the focus will be on the RRTM-G solar-infrared part (RRTM-GS) only. It provides 14 continuous bands (see Tab. 2.1) based on a reduced number of 112 supporting points, called g-intervals. The given spectral resolution of RRTM-G defines the spectral bands of ecRad. Figure 2.6 presents simulated downward F^\downarrow at TOA and at the surface with a spectral resolution of 1 nm for a cloud-free atmosphere. The spectral bands of ecRad are indicated by alternating gray and white sections. The bands are numbered according to Tab. 2.1. The plot clearly shows the spectral signature in F^\downarrow resulting from the absorption and scattering by gases in different wavelength ranges marked by the arrows. Characteristic absorption features in the near-infrared range are present around 1140 and 1400 nm wavelength due to H₂O, which are poorly resolved by the coarse resolution of ecRad.

2.5.2 Optical Properties

To relate the cloud microphysical with the optical properties of liquid water clouds in the IFS, the two-stream radiation code of Edwards and Slingo (1996) was used to create pre-calculated tables of the mass-extinction coefficient β , single scattering albedo ω , and asymmetry parameter g as a function of the particle effective radius r_{eff} . The resulting Padé parameterizations (Hogan and Bozzo, 2018),

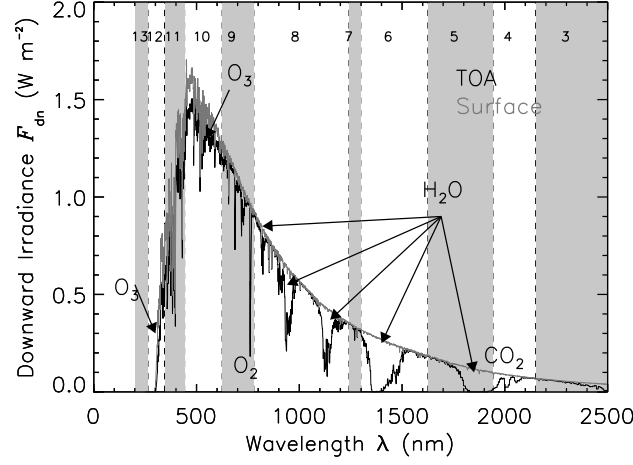


Figure 2.6: Simulated spectral downward irradiance F_{λ}^{\downarrow} at top of atmosphere (TOA) and at the surface. Spectral bands of ecRad are marked by dashed lines. Band number is indicated by the number. Relevant gas absorption bands are indicated by arrows.

for liquid water clouds are given by:

$$\beta = \frac{[a_0 + r_{\text{eff}} \cdot (a_1 + r_{\text{eff}} \cdot a_2)]}{1 + r_{\text{eff}} \cdot [a_3 + r_{\text{eff}} \cdot (a_4 + r_{\text{eff}} \cdot a_5)]} \quad (2.35)$$

$$\omega = 1 - \frac{[b_0 + r_{\text{eff}} \cdot (b_1 + r_{\text{eff}} \cdot b_2)]}{1 + r_{\text{eff}} \cdot (b_3 + r_{\text{eff}} \cdot b_4)} \quad (2.36)$$

$$g = \frac{c_0 + r_{\text{eff}} \cdot (c_1 + r_{\text{eff}} \cdot c_2)}{1 + r_{\text{eff}} \cdot (c_3 + r_{\text{eff}} \cdot c_4)}. \quad (2.37)$$

The coefficients are determined for each of the IFS spectral bands. These parameterizations are referred as SOCRATES within the IFS. The droplet size distributions base on Rockel and Raschke (1991).

To calculate ω , β , and g of ice water clouds from the particle effective diameter D_{eff} and ice water content IWC , the IFS uses the polynomial fits from Fu (1996):

$$\beta = a_0 + a_1/D_{\text{eff}} \quad (2.38)$$

$$\omega = 1 - (b_0 + b_1 \cdot D_{\text{eff}} + b_2 \cdot D_{\text{eff}}^2 + b_3 \cdot D_{\text{eff}}^3) \quad (2.39)$$

$$g = c_0 + c_1 \cdot D_{\text{eff}} + c_2 \cdot D_{\text{eff}}^2 + c_3 \cdot D_{\text{eff}}^3 \quad (2.40)$$

The coefficients a_i , b_i , and c_i are given with a varying spectral resolution (min. 30 nm) and are interpolated to match the spectral resolution of ecRad. The full set of coefficients is available in Fu (1996).

It has to be emphasized that Fu (1996), Fu et al. (1998a), Sun and Rikus (1999), and Sun and Fu (2001) assume hexagonal crystals. For other ice crystal shapes these size definitions are not valid and will lead to uncertainties and deviations in the calculated effective radius and in the RTS.

Applying the above parameterizations, the cloud optics module uses the mass-mixing ratios of condensed liquid water and ice, the fractional cloud cover, and the particle effective radius r_{eff} for liquid water and ice particles, to calculate profiles of F . These simulations are performed for each spectral band of ecRad. Forward scattering of aerosol and cloud particles are treated separately by Delta-Eddington-Scaling within the ecRad modules (Hogan and Bozzo, 2018).

2.5.3 Radiative Transfer Solver

The radiative transfer solver combines the optical properties of the cloud-free and cloudy fluxes from the gas, aerosol, and cloud optics module scaled by the fractional cloud cover and the selected cloud overlap assumption.

Despite an increasing spatial resolution, current NWP still use horizontal grid-box sizes with several kilometers. Depending on the number of vertical model levels, the vertical resolution is in the range of tenths of meters increasing with height. Small scale clouds, like trade wind cumuli, cover only minor parts of a grid-box and representation of sub-grid cloud heterogeneity becomes important. These sub-grid heterogeneities have to be considered in the simulations as the assumption of homogeneous and plane-parallel clouds is not fulfilled for these partly covered grid-boxes. Therefore, different radiative transfer solvers are developed to parameterize these effects.

For the IFS, Tiedtke (1993) developed a method, where the grid-box is divided in a cloudy and the cloud-free part. The fraction of the cloudy part is defined by the prognostic cloud fraction f provided by the IFS. The scheme assumes a homogeneous distribution of the LWC in the cloudy part, which does not represent the natural variability of LWC . The scheme by Tiedtke (1993) leads to a cloud top albedo bias (Cahalan, 1994; Cahalan et al., 1995), which is corrected by a factor implemented by Tiedtke (1996). However, the fixed factor is not applicable for all cloud situations.

Later, the Independent Column Approximation (ICA) was introduced (Hogan and Bozzo, 2018). It divides a grid-box in sub-grid columns and performs the RTS for each sub-column individually. Afterwards, the average over all sub-columns is determined. However, this method is computational expensive and not well suited for NWP. It was further developed to the Monte Carlo Independent Column Approximation (McICA) by Pincus et al. (2003) and Barker et al. (2008) with improved performance and lower numerical noise.

Subsequent developments led to the 'Triplecloud' solver (Shonk and Hogan, 2008) based on the code of Edwards and Slingo (1996). This solver is an alternative approach to account for sub-grid size cloud heterogeneity in NWP and GCM. The Tripleclouds solver is used for all ecRad simulations in this thesis. The latest improvement in the RTS within the IFS is the 'Speedy Algorithm for Radiative Transfer through Cloud Sides' (SPARTACUS) (Hogan et al., 2016). The new solver is designed to consider for 3D cloud effects. It addresses the two shortcomings of the previous solvers by using periodic boundary conditions to consider for lateral photon transport and cloud heterogeneity, which are represented by dividing the grid-box into different cloud regions, similar to the Tripleclouds approach. In spite of that, the SPARTACUS solver is still experimental but first comparisons with libRadtran 3D simulations showed good agreement (Hogan et al., 2016).

2.6 library for Radiative transfer (libRadtran)

The library for Radiative transfer (libRadtran) is a suit of radiative transfer solvers. The main tool of this package is 'uvspec', which allows to calculate vertical profiles of spectral irradiance, radiance, and actinic fluxes. The simulations cover a spectral range from 120 nm in the ultra-violet to 100 μm in the microwave spectral range.

Within uvspec, a variety of options are available. The main features are 12 RTS, including the two-stream method and higher orders of streams. Pre-defined standard-atmospheres for different regions of the Earth are available. The inclusion of self-defined atmospheric profiles for temperature, pressure, and the main gaseous constituents of the atmosphere is possible. Radiosonde data, molecular absorption for different aerosol regimes, and surface albedo parameterizations can be incorporated. To represent incoming solar radiation at the TOA, different extra-terrestrial irradiance spectra can be selected. Representation of liquid water and ice water clouds is possible by defining vertical profiles of water content and particle effective radius in two separate cloud files for the two phases. To transfer the microphysical properties of liquid water clouds to optical properties, pre-calculated Mie tables are

available. In case of ice water clouds, a set of parameterizations can be selected, covering different ice crystal habits, e.g., columns, hexagonal plates, and droxtals. Ice crystal surface roughness ranges from smooth to severe can be selected, e.g., Fu (1996), Fu et al. (1998b), Baum et al. (2005a). All these options make libRadtran a versatile tool and the simulations are regarded as a benchmark for ecRad. More detailed information on libRadtran and its application are given by Mayer and Kylling (2005), Emde et al. (2016), and the libRadtran documentation (Mayer et al., 2017).

2.7 Independent Pixel Approximation

All simulations in this thesis, are performed on the basis of the Independent Pixel Approximation (IPA), alternatively called Independent Column Approximation. This method is applied in radiation modeling to approximate the radiative properties of an individual pixel / column. It assumes, that radiative properties, e.g., cloud top albedo, of a horizontal field are independent from surrounding pixels and, therefore, allows to apply the one-dimensional / two-stream radiative theory.

Since the introduction of IPA by Cahalan and Joseph (1989), the approach was validated with 3D Monte Carlo simulations, including column interactions and lateral photon transport to quantify characteristic errors and identify limitations of IPA compared to the 3D simulations (Marshak et al., 1995; Scheirer, 2001). According to these studies, the IPA accuracy mainly depends on two factors:

i) The first factor is the pixel size, which is given by the horizontal and vertical grid resolution. To quantify the influence of the grid-box shape, Marshak et al. (1995) defined the pixel aspect ratio, which is the relation of the vertical to the horizontal grid box size. For small ratios the simulations are close to the estimations of a parallel, homogeneous cloud and the IPA results become more accurate. Due to the increased horizontal size of an individual cell with respect to its vertical size, photon exchanges with surrounding columns are less frequent. Contrarily, a large pixel aspect ratio results in horizontally small individual columns compared to their vertical extend, where lateral exchanges of radiation becomes more likely. In the latter case the IPA shows significant deviations with respect to 3D simulations.

The deviations between IPA and 3D simulations are not consistent for all cloud types. Scheirer (2001) highlights the dependence of the IPA accuracy on the cloud optical thickness τ . They found, that the agreement between the IPA and 3D models is better for clouds with $\tau \geq 10$. Due to larger τ , photons are absorbed, multi-scattering is decreased, and simulations for a single column are less influenced by surrounding columns. Therefore, differences between IPA and 3D are pronounced for τ between 2 and 10 due to the non-linearity of the cloud albedo with respect to τ . They further emphasized that IPA is not valid for convective and multi-layer clouds where errors are nearly independent from τ . Consequently, IPA is only valid for small aspect ratios and when the cloud optical thickness τ exceeds values of 10.

ii) As a second factor, Marshak et al. (1995) found wavelength dependent impacts on the simulated radiation. Model validations indicate, that the IPA is more realistic for absorbing wavelengths larger than 1200 nm, while the agreement is reduced for scattering wavelengths. As the spectral albedo $\alpha(\lambda)$ is a function of the single-scattering albedo $\tilde{\omega}$, a decrease in $\tilde{\omega}$ with increasing wavelength leads to reduced scattering and enhanced absorption, simultaneously reducing the likelihood for multiple-scattering effects and according lateral photon transport.

Both effects have to be considered and their significance has to be estimated when simulated and measured irradiances of different cloud regimes are compared.

3 Instrumentation and Observations

Data presented in this work was collected during two different field campaigns. The Next Generation Remote Sensing for Validation Studies (NARVAL-II, Stevens et al. 2019) focused on shallow trade wind cumuli in subtropical regions, while the North Atlantic Waveguide and Downstream impact EXperiment (NAWDEX, Schäfler et al. 2018) field campaign aimed to investigate adiabatic processes, cloud development of low pressure systems over the North Atlantic Ocean, and to evaluate NWP models.

The Spectral Modular Airborne measurement sysTem (SMART), with its measurement setup and calibration procedure, and an estimation of measurement uncertainties are introduced in Section 3.2.1. The active and passive microwave remote sensing by the HALO Microwave Package (HAMP) (Mech et al., 2014) are introduced in Section 3.2.2 and additional observations are mentioned in Section 3.2.3.

3.1 High Altitude and Long Range Research Aircraft (HALO)

HALO is a research aircraft based on a commercial G 550 model of the manufacturer Gulfstream®. The aircraft is stationed in Oberpfaffenhofen, Germany and operated by the Deutsche Zentrum für Luft- und Raumfahrt (DLR). The technical capabilities of HALO, with its max flight range of 8000 km, the cruising altitude of 15.5 km, and a maximum take-off weight of 41 t, allow to observe wide areas of the Earth with a comprehensive set of passive and active remote sensing instruments. The research priorities of HALO are aerosol particles, clouds, and the chemistry of atmosphere and tropopause as well as climate change and extreme weather events. Project partners are 16 universities, Helmholtz centers, the Max Planck Association, the Leibniz Association, and research institutions of the German Federal Ministries.

3.2 Instrumentation

During NARVAL-II and NAWDEX, HALO was equipped with a set of active and passive remote sensing instruments. The locations of the individual instruments are given in Fig. 3.1. Table 3.1 lists all instruments, measured quantities, and responsible operators.

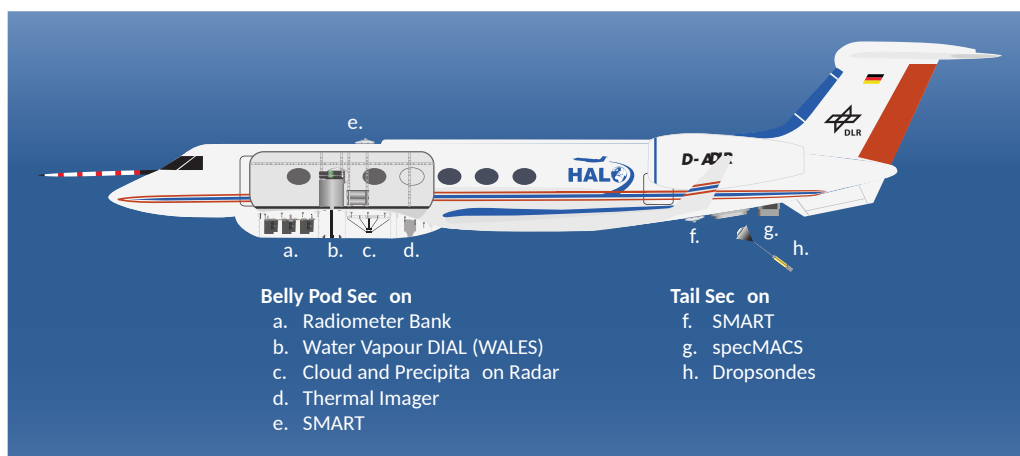


Figure 3.1: Side view of HALO giving the locations of the deployed instruments. Adapted from Stevens et al. (2019).

Table 3.1: List of installed instruments, observed and derived properties, and operators during NARVAL-II and NAWDEX. Table adapted from Schäfler et al. (2018)

Instrument	Observed and derived properties	Institute	Operator
HALO Microwave Package (HAMP)	integrated water vapor, temperature and humidity profiles, liquid and ice water path, profiles of radar reflectivity	University Cologne / University of Hamburg	F. Ament / S. Crewell
SMART	spectral upward and downward irradiance, nadir radiance, cloud top albedo and phase	University Leipzig	M. Wendisch
Water Vapor Differential Absorption Lidar in Space (WALES)	profiles of water vapor, backscatter coefficients, particle depolarization ratio, particle extinction coefficient, cloud top height	DLR	M. Wirth
specMACS: Imaging cloud spectrometer	spectral upward radiance, cloud top phase and effective radius	University of Munich	B. Mayer
Dropsonde system	temperature, humidity, wind profiles	University of Hamburg	F. Ament

3.2.1 Spectral Modular Airborne measurement sysTem (SMART)

The SMART-Albedometer has been developed at the Leibniz-Institute for Tropospheric Research (TROPOS), to measure solar radiation spectrally (Wendisch et al., 2016). A scheme of the principle set-up is given in Fig. 3.2. Upward and downward solar radiation is collected with three independent optical inlets connected via fiber optics to six separate Zeiss grating spectrometers. The incident radiation is dispersed by gratings and projected on a single-line photo-diode array (PDA) acting as an analog-digital converter. Depending on the intensity of the radiation per diode an electronic signal is generated by the photoelectric effect. This discrete signal is recorded by a data acquisition system and stored on a hard-drive. To link the recorded signal with absolute values of the measured radiation, a radiometric calibration has to be performed for each of the spectrometers.

The modular construction of SMART allows to adapt the setup depending on the application, which makes it flexible to install. Each SMART module consist of two separate spectrometers. The spectrometer for the visible (VIS) covers a wavelength range between 200 - 1050 nm, with 1024 diodes per array leading to a spectral resolution of 2 to 3 nm (full width at half maximum, FWHM). In the near-infrared (NIR) spectral range wavelength from 950 - 2100 nm are covered, with 512 diodes per array with a varying spectral resolution between 9 and 16 nm FWHM. In the NIR the thermal noise of the spectrometers has to be considered, which is generated by random motions of electrons in the diode array. To determine the temperature depended dark current, a shutter is installed in the optical path of the NIR spectrometer. In distinctive temporal intervals the shutter is closed and dark measurement are performed. This dark measurement signal is subtracted from the light exposed measured signals. In the VIS no dark measurements are needed. The VIS signal is corrected by adjusting the raw counts below 250 nm to zero, assuming that all radiation below this wavelength is absorbed under atmospheric conditions and is pure dark noise.

Because of edge effects at the lower and upper boundaries of the spectrometer wavelength range, the radiation cannot be focused precisely on the array edges. This leads to low signal intensities just above the detection threshold resulting in low signal-to-noise ratios. Therefore, only the wavelength range from 266 to 2100 nm is usable.

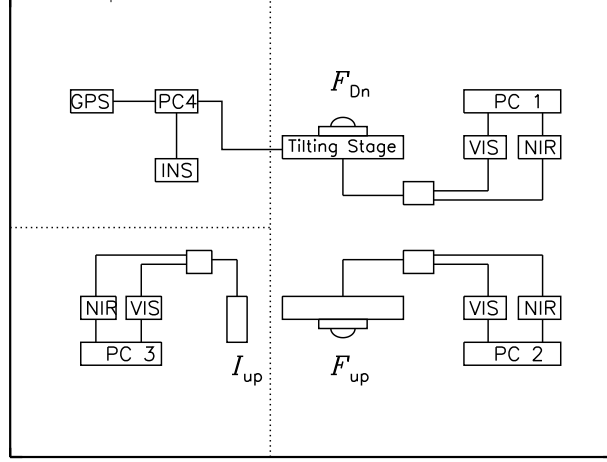


Figure 3.2: Schematic of the SMART measurement setup. Top-left: Navigation unit for aircraft position and attitude feeding the controller of the tilting stage. Right: Optical inlets for irradiance with optical fibers, spectrometers, and data acquisition. Lower left: Optical Inlet for radiance with optical fibers, spectrometers, and data acquisition.

During NARVAL-II and NAWDEX, SMART has measured spectral upward F_{λ}^{\uparrow} and downward irradiance F_{λ}^{\downarrow} as well as spectral upward radiance I_{λ}^{\uparrow} . Each quantity was recorded with two separate Zeiss grating spectrometers, covering the VIS and NIR range. By merging the spectra for VIS and NIR, about 97 % of the solar spectrum are covered (Bierwirth et al., 2009). During both campaigns a fixed spectrometer integration time t_{int} of 0.5 s was chosen as a compromise between sufficient Signal-to-Noise-Ratio (SNR) and overexposure of the spectrometers.

Radiance Optical Inlet

For remote sensing of cloud optical properties, measurements from the radiance optical inlet are used. The inlet is based on a Zeiss collimator lens, which acts as a telescope by focusing the narrow light beam into the opening cone of the optical fiber. The I_{λ}^{\uparrow} inlet has an approximate opening angle Γ_{OI} of 2° , slightly depending on the diameter of the optical fiber, determined by laboratory tests (Ehrlich, 2009). The footprint diameter D_{FOV} is determined by the distance Δz between the optical inlet and the observed object, and the opening angle Γ_{OI} by:

$$D_{\text{FOV}} = 2 \cdot \tan \left(\frac{\Gamma_{\text{OI}}}{2} \right) \cdot \Delta z \quad (3.1)$$

With t_{int} of 0.5 s, an average aircraft ground-speed of about 220 m s^{-1} , and a distance of $\approx 10 \text{ km}$ between cloud top and aircraft, this leads to a FOV of about $100 \text{ m} \times 120 \text{ m}$ for an individual pixel.

Irradiance Optical Inlets

Figure 3.3 shows a sketch of the irradiance optical inlets, which are constructed as integrating spheres. The incident photons penetrate a quartz glass dome and a Spectralon[®] coated inside of the inlet diffuses the radiation, and guides the photons into the optical fibers. A cone in the middle of the sensor shades the optical fiber inlet from the direct component of the radiation. The internal construction of the optical inlet ensures a approximate cosine-weighted sampling of the photons. Wavelength-dependent relative errors are in the range of $\pm 3 \%$ (Wendisch et al., 2001, 2002; Ehrlich et al., 2009). For solar zenith angles θ_0 close to 0° (high sun) or 90° (sun at the horizon) the deviations from the cosine response increase.

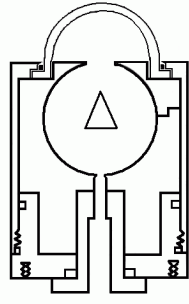


Figure 3.3: Schematic of the irradiance optical inlet mounted at the upper and lower fuselage of HALO. Adapted from A. Ehrlich.

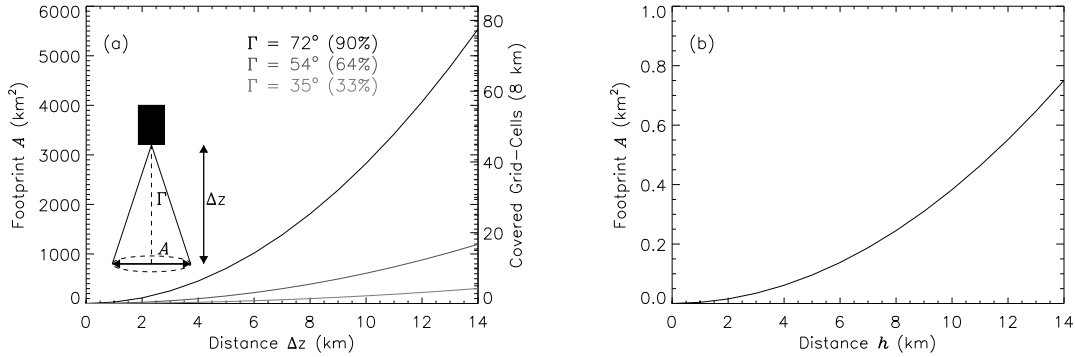


Figure 3.4: Footprint size A of the measured spectral upward irradiance F_λ^\uparrow (a) and radiance I_λ^\uparrow (b) as a function of the distance Δz between cloud and sensor at flight altitude. For F_λ^\uparrow an additional axis indicates for the sensor covered model grid-cells with 8 km size.

The inlets are mounted at the upper and lower aircraft fuselage, collecting radiation from the entire upper and lower hemisphere. From the definition of F and integrating Eq. 2.8 over all azimuth angles φ , F for variable θ is given by:

$$F(\theta) = I \cdot \pi \cdot \cos^2\theta, \quad (3.2)$$

with $\theta = 90^\circ - \vartheta$. The fraction \mathcal{H} of total F_{tot} is then:

$$\mathcal{H} = \frac{F_\theta}{F_{\text{tot}}} = \frac{I \cdot \pi \cdot \cos^2\theta}{I \cdot \pi} = \cos^2\theta. \quad (3.3)$$

Assuming an average flight altitude of 12 km and a cloud height of 2 km for a low-level liquid water cloud, a resulting distance of $\Delta z \approx 10$ km between aircraft and cloud is present. To cover the FOV of the irradiance inlet with a cloud by 90 %, a circular cloud has to have a diameter of 60 km or a covered area of 2827 km². In case of observing high-level ice water clouds with a lower distance of 1 km between cloud and aircraft, and a coverage of 90 % the cloud has to have a diameter of 2 km or a covered area of 7 km². In Fig. 3.4 the dependence of the observed area as a function of the distance between sensor and cloud, and the fraction of the influenced F is given. On the second ordinate axis the number of covered model grid-cells, assuming a spatial resolution of 8 km, is given.

It shows that upward irradiances of low-level clouds observed by high flying aircraft comprise up to 80 grid-boxes, which is in contradiction to the IPA. In contrast, homogeneous clouds with small δz , better fit the IPA simulations and are less prone to potential biases.

Horizontal Stabilization Platform

SMART on HALO uses a horizontal stabilization platform to ensure horizontal alignment of the irradiance inlet independently of the aircraft attitude. A detailed description is given by Wendisch et al. (2001) and Wendisch et al. (2004). Due to the space limitation on HALO, during NAWDEX and NARVAL-II, only the upper F_{λ}^{\downarrow} inlet was actively stabilized, while the lower F_{λ}^{\uparrow} inlet was fixed to the aircraft fuselage. Therefore, F_{λ}^{\uparrow} are assumed to be dominated by isotropic radiation and mostly independent from the aircraft attitude.

The stabilization platform consists of two motors, tilting the optical inlet around two axes. The attitude of the aircraft is determined by an Inertial Measurement Unit (IMU) measuring heading, angular accelerations, and the position of the aircraft. A controlling unit uses this information to calculate counterbalancing motions of the inlet. Attitude corrections are limited to a certain angular degree. For the roll and pitch angles a maximum of $\pm 6^\circ$ can be compensated with an accuracy better than $\pm 0.2^\circ$. The response time to sudden changes is reported with 43 ms.

Measurements outside of the correction range are not horizontally aligned by the platform and are excluded from further usage. Upward irradiance F^{\uparrow} is assumed to be comprised of a diffuse component only and to be isotropic under common atmospheric conditions, e.g., no sun-glint from the ocean surface. By that, the sensitivity of F^{\uparrow} on changing roll angles ϕ_{ac} and pitch angles θ_{ac} of the aircraft are below the measurement uncertainty and can be neglected. For flight legs with curves (ϕ_{ac} and $\theta_{ac} > 4^\circ$), F^{\uparrow} can be biased by radiation from the upper hemisphere, intensifying for larger absolute values of ϕ_{ac} and θ_{ac} . The pitch angle of HALO during straight flight legs at cruise altitude is between $1.8^\circ < \theta_{ac} < 3.2^\circ$ on average and compensated by the F^{\uparrow} sensor mounting. Measurements exceeding $\phi_{ac} > \pm 1.5^\circ$ and $1.8^\circ < \theta_{ac} > 3.2^\circ$ are excluded to ensure near-horizontal alignment of F^{\uparrow} .

Calibration

Prior and after the measurement campaigns, SMART was radiometrically calibrated in the laboratory using certified calibration standards traceable to the National Institute of Standards and Technology (NIST). The radiometric calibration relies on the basic assumption that the radiometric quantity Q_{λ} can be connected by a constant calibration factor c_{λ} , with the measured counts S by:

$$S_{\lambda} = c_{\lambda} \cdot Q_{\lambda}. \quad (3.4)$$

The calibration factor has to be determined for all pixels of the diode array. To determine c_{λ} the sensor is mounted in front of the 1000 W calibration lamp with a defined distance of 50 cm. The calibration lamp emits with a well-known intensity per wavelength (Q_{λ}) while the spectrometers measure S_{λ} . In that way c_{λ} is determined separately for each optical inlet and spectrometer. While the F_{λ} inlets are exposed to direct radiation from the reference lamp, the calibration of I_{λ} needs diffuse light and is performed with a certified integrating sphere. This sphere contains a light source hidden by a baffle to avoid direct radiation. The inside of the sphere is coated with barium sulfate to provide diffuse radiation. The certification of the sphere does not allow a calibration below 400 nm and a second setup utilizing the 1000 W calibration lamp and a reflecting panel is used, proving calibration for wavelength below 400 nm.

Assembling and disassembling of the instrument setup will change c_{λ} and a secondary calibration is needed, when the instruments are installed on HALO in the field. The secondary calibration is performed by a mobile standard, using so called Ulbricht spheres, which are integrating spheres with internal lamps, emitting diffuse radiation. By that c_{λ} is transferred to the mobile standard by using the identical calibration setup as used for the reference lamp. Because of the transfer of the absolute calibration, this procedure is also called transfer calibration. It further allows to track potential changes of the instrument sensitivity during the campaign. By comparing measurements, which were performed with the portable integrating sphere during the absolute calibration process, with transfer calibrations in the field, the spectral differences due to re-connection of the fibers are determined. When the spectrometer signal is transformed into spectral radiances and irradiances, the spectral transfer calibration factor (\mathcal{T}_{λ}) is multiplied to consider for the changes of the transmissivity of the entire optical path. \mathcal{T}_{λ} is determined by the ratio of the spectrometers digital counts during the

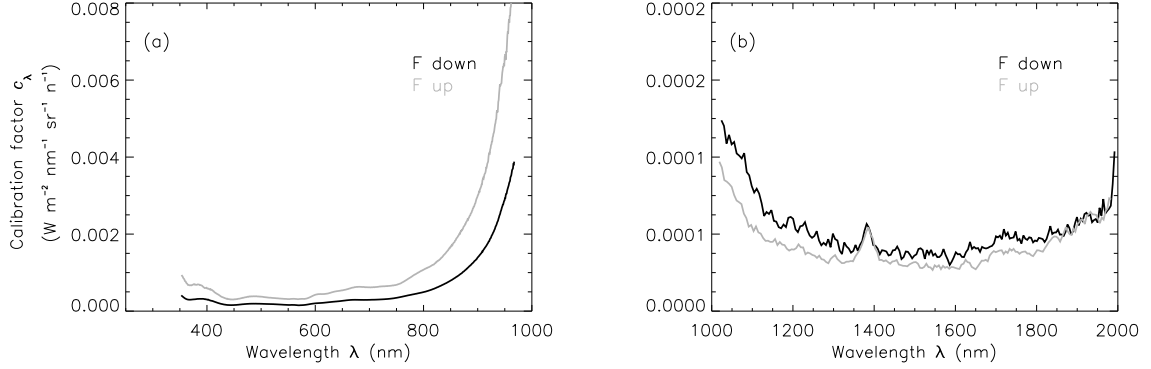


Figure 3.5: Spectral calibration factors c_λ for the VIS (a) and the NIR spectrometer (b). Black line shows for downward and gray line for upward irradiance.

absolute calibration G_{abs} to the digital counts in the field G_{fie} :

$$\mathcal{T}_\lambda = \frac{G_{\text{abs}}(\lambda)}{G_{\text{fie}}(\lambda)}. \quad (3.5)$$

Figure 3.5a and Fig. 3.5b show spectral calibration factors for the upward (gray) and downward (black) irradiance composed of the absolute and the transfer calibration. The described radiometric calibration is applied to F_λ and I_λ inlets.

Because of the non-linearity of the spectrometers with regard to the integration time, the absolute and transfer calibration have to be performed for several t_{int} , which are used in the field campaign. The integration times have to be selected carefully to avoid underexposure (poor SNR) or overexposure (loss of spectral signature) of the spectrometers. For each integration time a new c_λ is determined.

In addition, the optical inlets for F_λ have to be characterized for their cosine response. The sensor is illuminated by a direct radiation source and then tilted by steps of 3 to 5 degree, scanning from -95 to 95 degree for two directions (perpendicular). For each step a measurement of the raw signal is performed. From these procedure the cosine correction factor $k_{\text{cos}}(\theta)$ is calculated by:

$$k_{\text{cos}}(\theta) = \frac{S(\theta = 0^\circ) \cdot \cos(\theta)}{S(\theta)}. \quad (3.6)$$

The obtained correction factors only apply for direct radiation. The diffuse correction factors $k_{\text{cos}}^{\text{diff}}(\theta)$ are calculated with:

$$k_{\text{cos}}^{\text{diff}}(\theta) = 2 \cdot \int_0^{90} k_{\text{cos}}(\theta) \cdot \cos \theta \cdot \sin \theta \, d\theta. \quad (3.7)$$

The measured irradiance $F_{\text{mea}}^\downarrow$ is then corrected by:

$$F_{\text{corr}}^\downarrow = f_{\text{dir}} \cdot k_{\text{cos}}(\theta) \cdot F_{\text{mea}}^\downarrow(\theta) + (1 - f_{\text{dir}}) \cdot k_{\text{cos}}^{\text{diff}}(\theta) \cdot F_{\text{mea}}^\downarrow(\theta) \quad (3.8)$$

for each wavelength / pixel with f_{dir} the direct fraction of $F_{\text{mea}}^\downarrow$. The direct fraction is estimated by utilizing radiative transfer simulations along the flight path considering solar zenith angle (SZA), location, aerosol load, and flight altitude. Correction is only possible when there is no cloud above the aircraft.

Table 3.2: Measurement uncertainties of SMART for the VIS and NIR spectrometer.

	Wavelength range (nm)	Absolute calibration (%)	Spectrometer signal (%)	Transfer calibration (%)	Total (%)
VIS	250 - 1000	5	< 1	1.2	5.4
NIR	1000 - 2200	8	2.3	1.1	8.4

Measurement Uncertainties

The total measurement uncertainties of $F_{\lambda}^{\downarrow\uparrow}$ and I_{λ}^{\uparrow} are composed of individual errors by the spectral calibration, the spectrometer noise and dark current, the primary radiometric calibration, and the transfer calibration. Assuming that these uncertainties are independent from each other and normally distributed, the total uncertainty is determined by Gaussian error propagation.

The absolute calibration uncertainty of I_{λ}^{\uparrow} consist of the uncertainty of the 1000 W reference lamp (5 %) and the reflectance panel (< 1 %). Both values are provided by the manufacturers. For the alternative calibration of I_{λ}^{\uparrow} utilizing the integrating sphere, an uncertainty of 5 to 10 % is given. The uncertainty of the raw counts from the spectrometers depends on the signal-to-noise-ratio and the wavelength calibration. The standard deviation of the signal is 2 - 3 counts in the VIS and 15 - 25 counts in the NIR. The maximum range of counts from the spectrometers is between 0 and 32700. Utilizing appropriate t_{int} of 0.5 s the signal is around 15000 counts in the VIS and 20000 counts in the NIR. The sensitivity of the spectrometers is reduced for $\lambda < 300$ nm and $\lambda > 2100$ nm leading to poor SNR and consequent higher relative uncertainties. Measurements below and above these wavelength are not used.

For typical conditions and observations the total measurement uncertainty of irradiances $F_{\lambda}^{\uparrow\downarrow}$ and upward radiance I_{λ}^{\uparrow} is about 5.4 % for the VIS and 8.4 % for the NIR range. Finally, measured $F_{\text{mea}}^{\downarrow\uparrow}$ are checked for correct signal processing. Table 3.2 lists the individual calibration errors separated for the two spectrometer wavelength ranges.

3.2.2 HALO Microwave Package (HAMP)

The HALO Microwave Package (HAMP) is a combination of a passive microwave radiometer and an active cloud radar specifically designed for the operation on HALO (Mech et al., 2014). The microwave radiometer includes 26 frequency channels between 22.24 GHz and 183.31 ± 12.5 GHz. The brightness temperature (BT) measured along the 22.24 GHz and 183.31 GHz rotational water vapor lines provide information on the total column water vapor (Schnitt et al., 2017) and information on its vertical distribution. Liquid water emission increases roughly with the frequency squared. By combining BT in window channels, i.e., 31.4 GHz and 90 GHz, mostly affected by liquid water with those sensitive to water vapor the *LWP* can be retrieved. This principle is also employed by satellite instruments, which provide global climatologies of *LWP*, suffering from the coarse footprint of a few 10ths of kilometer (Elsaesser et al., 2017).

The statistical *LWP* retrieval is based on a large variety of atmospheric profiles with differently structured warm clouds as training data composed from the dropsondes as described by Schnitt et al. (2017). Synthetic BT are simulated from these profiles and subsequently used to fit a multi-parameter linear regression model employing higher order terms following Mech et al. (2007). Testing the retrieval algorithm on an independent subsample provides an accuracy of about 30 g m^{-2} for *LWP* values below 500 g m^{-2} .

The cloud radar MIRA-36 operates at a frequency of 36 GHz and has a similar horizontal resolution as the *LWP* of about 1000 m and a temporal resolution of 1 s. Vertical profiles are divided into 30 m bins (Mech et al., 2014). The radar provides different parameters linked to the cloud microphysical properties including the radar reflectivity *Z*, the linear depolarization, the Doppler velocity, and the spectral width of the droplet size distribution. The latter two are affected by the relative motion of the aircraft to the wind and the antenna width (Mech et al., 2014).

3.2.3 Additional Instrumentation

Vapour Lidar Experiment in Space (WALES)

The Differential Absorption Lidar (DIAL) called WALES operates at four wavelengths near 935 nm to measure atmospheric water vapor and derive vertical profiles of mixing ratios, covering the atmosphere below the aircraft. WALES also contains channels for aerosol measurements at 532 nm and 1064 nm wavelength with depolarization detection. At 532 nm, WALES uses the high-spectral resolution technique, which distinguishes molecular from particle backscattering, to enable direct extinction measurements. Within this study only the aerosol channels are used to provide information on the cloud top height. The ranging resolution of the instrument is 15 m. Together with the flight altitude inferred from the HALO on-board positioning system and an appropriate attitude correction the accuracy of the cloud top height detection is about 20 m.

The laser has a beam divergence of 1 mrad, which leads to an illuminated spot of 10 m diameter on ground at a flight altitude of 10 km. Laser pulses are emitted with a repetition rate of 100 Hz. 20 signals are averaged to improve the SNR, resulting in an along flight track resolution of 44 m at 200 m s⁻¹ aircraft speed. Thus, the horizontal resolution is reduced as compared to SMART and HAMP. Along track, this can be taken into account by further signal averaging.

spectrometer of the Munich Aerosol Cloud Scanner (specMACS)

The spectrometer of the Munich Aerosol Cloud Scanner (specMACS), captures fields of upward I_{λ}^{\uparrow} as well as images in the visible and near-infrared wavelength range of the cloud scene below the aircraft. Latter allow to get a visual impression of the cloud distribution below HALO.

3.2.4 Moderate Resolution Imaging Spectroradiometer (MODIS)

The MODIS instrument is installed aboard the Terra and Aqua satellites operated by the National Aeronautics and Space Administration (NASA). Both satellites follow a sun-synchronous orbit around the Earth. MODIS takes measurements of the upward radiance in 36 spectral bands ranging from 400 nm to 14.4 μ m with varying spatial resolution between 250 and 1000 m, with lower resolution for increasing wavelength. The measured radiances are used for remote sensing of land, cloud, aerosol, and atmospheric properties, e.g., to derive ice coverage, surface and cloud temperature, cloud top effective radius, cloud optical thickness, and liquid and ice water content. The MODIS sensor, the retrieval technique, and higher level products are described in Platnick et al. (2001, 2003, 2017).

3.3 Next Generation Remote Sensing for Validation Studies II

The NARVAL-II campaign is a field campaign led by the Max-Planck-Institute (MPI) Hamburg and the University of Hamburg. The aim of NARVAL-II was to investigate and characterize shallow trade wind cumuli. These clouds show a tendency for self-aggregation due to cloud-atmosphere-interactions, which are not fully understood yet (Bony et al., 2017). Representation of trade wind cumuli in NWP is limited and has to be validated by airborne measurements (Klocke et al., 2017), which are sparse (Stevens and Lenschow, 2001).

The campaign took place from 20 July to 31 August 2016. During this time HALO was stationed at the Bridgetown Airport, Barbados. Figure 3.6 shows all NARVAL-II flights and Tab. 3.3 lists the individual objectives and specifications of each flight.

NARVAL-II Research Flight 06 from 19 August 2016

Research flight 06 (referred as RF06) from the NARVAL-II campaign is investigated in this thesis as an exemplary case study. RF06 was carried out starting from Bridgetown, Barbados, on 19 August 2016. Figure 3.7 shows the flight track on a MODIS Terra satellite image captured at 19:30 UTC. The first target (lower circles) was approached with north-easterly flight direction. After the ferry section two circles with one hour duration were flown. The circle-patterns are used to derive estimates of large-scale vertical motions from dropsonde measurements (Stevens et al., 2019). The southern located circles covered an area, which was influenced by dust aerosol particles, confirmed by WALES measurements.

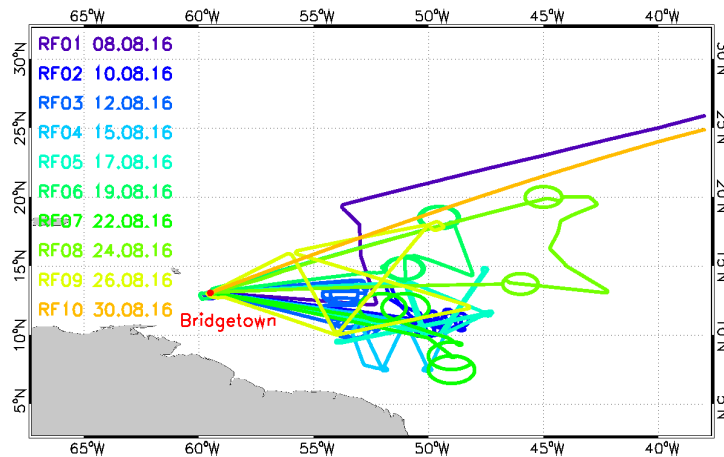


Figure 3.6: Flight tracks of HALO performed during NARVAL-II.

Table 3.3: Research flight (RF), date, time of day, available A-Train overpasses (AO), number of launched dropsondes, and flight objectives of the flights performed during NARVAL-II. Adapted from Stevens et al. (2019).

RF	Date	Time (UTC)	AO	#	Objective
01	08.08.	08:22 - 18:59	1507	9	Transfer flight
02	10.08.	11:53 - 20:47	1709	30	ITCZ Crossing
03	12.08.	11:43 - 19:37	n/a	50	Divergence, Radar Calibration
04	15.08.	11:49 - 19:46	1711	10	ITCZ Crossing
05	17.08.	14:48 - 23:07	1701	12	Satellite Validation (Cirrus)
06	19.08.	12:29 - 20:53	1648	53	Divergence, NTAS buoy recon
07	22.08.	11:17 - 20:58	n/a	13	Inner ITCZ (Doldrums)
08	24.08.	12:43 - 20:55	n/a	12	Gaston – Deep Conv. (no radar)
09	26.08.	13:44 - 20:54	n/a	12	Gaston – Shallow Conv. (no radar)
10	29.08.	09:44 - 19:00	n/a	17	Transfer flight, Stratus Circle (no radar)

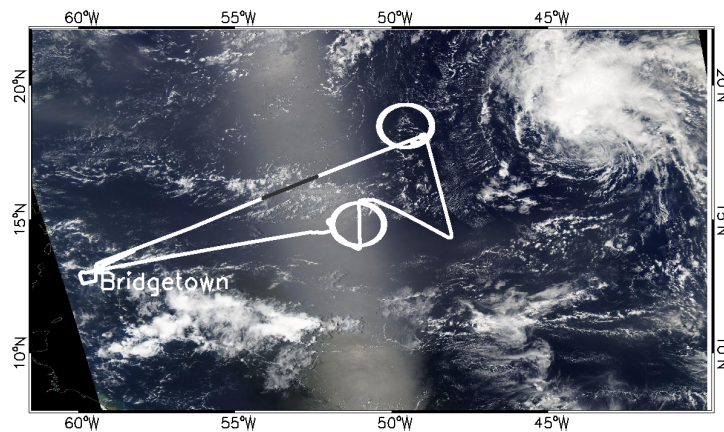


Figure 3.7: Flight track of HALO (white) of RF 06 (19 August 2016) plotted on a MODIS Terra satellite image from 19:30 UTC. Selected cloud section is highlighted in gray.

Table 3.4: Research flight (RF), date, time of day, number of launched dropsondes, and objectives of the flights performed during NAWDEX. Adapted from Schäfler et al. (2018).

RF	Date	Time (UTC)	#	Objective
-	15.09.	08:55 - 09:42		Transfer flight
01	17.09.	07:17 - 14:12	10	Waveguide near WCB outflow, Overflight Chilbolton, SMART Calibration Pattern, Radar Calibration Pattern at 2 FLs
02	21.09.	13:55 - 19:25	14	Waveguide near WCB outflow northwest of Iceland, WCB ascent south of Iceland related to cyclone Ursula
03	23.09.	07:36 - 16:36	32	Waveguide near WCB outflow, WCB ascent over easter North Atlantic related to cyclone Vladiana
04	26.09.	09:57 - 18:59	25	WCB ascent, tropopause fold, intensifying Ex-TC Karl
05	27.09.	11:32 - 20:37	22	Strong moisture Transport upstream of HIW predicted to Impact UK and Southern Scandinavia, PV Cut-off, Tropopause fold and remnants of Ex-Karl closer to Iceland
06	01.10.	08:22 - 11:48	3	TPV structure near Newfoundland
07	06.10.	07:02 - 16:13	20	TPV structure near Newfoundland
08	09.10.	10:24 - 19:04	9	PV streamer, WCB ascent related to cyclone Sanchez, Ra-Li Comparisons
09	10.10.	11:58 - 19:37	20	PV streamer and cyclone Sanchez
10	13.10.	07:58 - 15:58	26	Ridge Building northern North Atlantic, CAT, orographic gravity waves over Iceland, Andoya Overflight
11	14.10.	08:23 - 14:53	15	Ra-Lidar Observations, Aircraft coordination, A-Train
12	15.10.	08:41 - 14:36	-	TPV over New Foundland, GPM underflight
13	18.10.	08:51 - 14:41	16	Coordinated jet-crossing, PV cut-off over UK with ascent over North Sea, Overflight of Jülich

Subsequently, HALO flew in north-west direction towards tropical storm 'Fiona' (upper right part of the image), performing two further circle patterns. This area was almost unaffected by aerosol particles. Due to the low-pressure system, this area is characterized by more aggregated and deep-convective clouds, resulting in an increased total cloud cover. After the second circle pair, the ferry section to Bridgetown is characterized by aged, decaying cloud structures, containing remnants of mid-level clouds and cloud anvils.

3.4 North Atlantic Waveguide and Downstream impact EXperiment

The campaign took place from 19 September to 16 October 2016. During this time HALO was stationed at the Keflavik Airport, Iceland, which allowed to cover the entire North Atlantic region. During NAWDEX, HALO was equipped with the same instrumentation as during NARVAL-II.

Figure 3.8 shows all flight tracks during NAWDEX and Tab. 3.4 lists the individual objectives and specifications of the individual flights.

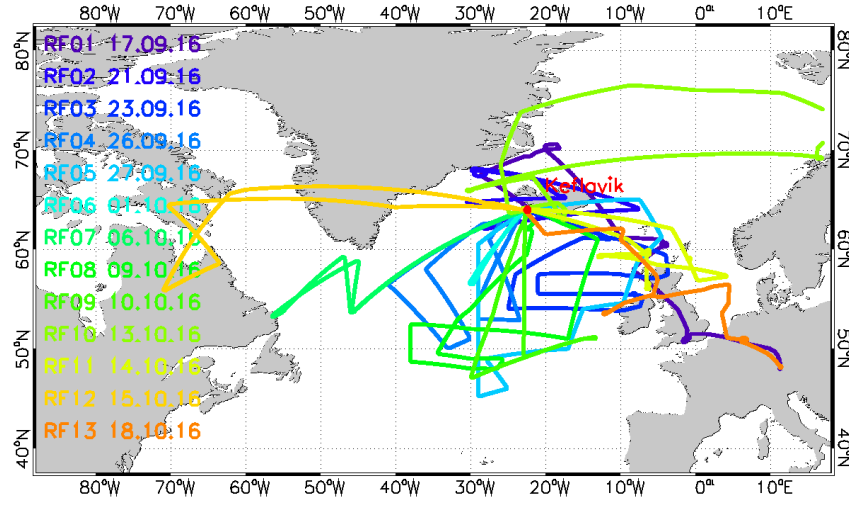


Figure 3.8: Flight tracks of HALO performed during NAWDEX.

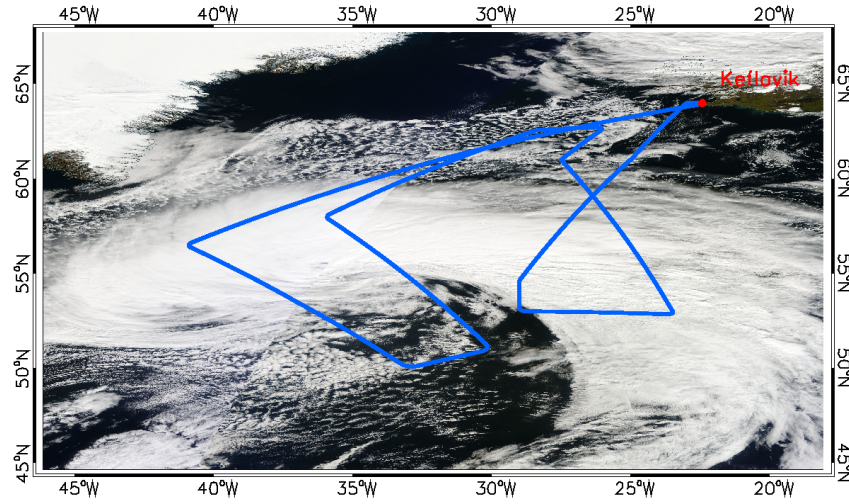


Figure 3.9: Flight track (blue) of HALO during the measurement flight of 26 September 2016. Observation of the low-pressure system 'Karl'. Sections selected for detailed analysis are marked in yellow.

NAWDEX Research Flight 04 from 26 September 2016

From NAWDEX, research flight 04 (RF04) from the 26 September 2016 is selected. Figure 3.9 shows the flight track of HALO on a MODIS Terra satellite image. RF04 targeted a region, which was influenced by cyclone 'Vladiana' within the previous 48 hours before take-off. Within this period the storm was displaced towards the British Islands and Norway. Vladiana was followed by the low pressure system 'Karl', which was a former tropical cyclone. Between both systems advection of warm and moist sub-tropical air masses from south-west towards north-east evolved. Situated aloft, a north-easterly trending jet stream developed with winds around 90 m s^{-1} at 300 hPa height, indicating for the strength of 'Karl'. Alongside, lifting of the sub-tropical air masses causes condensation and latent heat release, leading to vertically extended and wide-spread homogeneous cloud fields with homogeneous CT along the WCB. During the measurement period the low-pressure system moved from south-west to north-east. The frontal systems of 'Karl' were crossed almost perpendicular for four times to investigate the temporal evolution.

4 Retrieval of Cloud Droplet Number Concentration

NWP models, like the IFS, determine the cloud droplet effective radius r_{eff} on basis of the liquid water content LWC of a single grid-box and on assumptions of cloud condensation nuclei (CCN) concentration and activated cloud droplet number concentration N . Assumptions of CCN concentration are either set to constant values, e.g., in IFS for clouds over open ocean to 50 cm^{-3} until version 32R1, or utilize global aerosol climatologies, e.g., by Tegen et al. (1997). These two approaches do not necessarily represent the natural variability and the conditions during a particular measurement flight. In case of observations, where in-situ measurements of cloud properties are not available, one has to rely on remote sensing estimates or remote sensing of N .

The common method, using retrievals of cloud optical thickness τ and cloud droplet effective radius r_{eff} under the assumption of vertical adiabatic cloud profile, underlies several uncertainties (Grosvenor et al., 2018). Therefore, an advanced synergetic retrieval method for N (section 4.3) is presented in this chapter. The determination of N is adapted from Wolf et al. (2019). The retrieval is applied to RF06 of NARVAL-II to estimate N and, in turn, is applied in the RTS of ecRad.

4.1 Data Filtering

Trade wind cumuli appear randomly distributed with a tendency to form self-organizing structures (Bony et al., 2015). Typically, the vertical cloud extent of an individual cell is larger than the horizontal size. The dominance of such small-scale cumuli during NARVAL-II results in heterogeneous cloud scenes, which is in contrast to the assumption of stratiform cloud fields applied in the common retrieval techniques to derive τ , r_{eff} , and N . Clouds smaller than the instruments FOV, potentially bias the retrieval of the microphysical properties (Oreopoulos and Davies, 1998a,b). Therefore, three identifiers are required to select suitable flight sections for the retrieval of N .

4.1.1 Cloud, Precipitation, and Phase Identifier

Cloud Identifier

To distinguish between cloud and cloud-free measurements over ocean surfaces the ratio χ given by:

$$\chi = \frac{I_{858}^{\uparrow}}{I_{648}^{\uparrow}} \quad (4.1)$$

is used as a cloud identifier (Platnick et al., 2013). A running mean over 750 consecutive χ (approximately 12.5 min) is applied, to determine the baseline of χ . When χ exceeds the baseline by +0.025, the measurement is flagged as cloudy.

The horizontal extent of trade wind cumuli can be shorter than the SMART FOV. To identify such cases, an additional homogeneity cloud flag (HCF) is introduced. The cloud is considered homogeneous (HCF is true) when a single observation is enclosed by five cloud masked measurements. For clouds not surrounded by at least two cloudy pixel the HCF is set to false. Therefore, the HCF identifies clouds that are large enough to fill the FOVs of SMART and HAMP at the same time.

Observed Total Cloud Cover

Total cloud cover $f_{\text{tot,mea}}$ from SMART bases on individual measurements, flagged as cloudy or cloud-free. $f_{\text{tot,mea}}$ and resulting probability size distributions (PDFs) are determined by calculating a running mean of n consecutive measurements. The flight speed v_{ac} , the FOV of the instruments I^{\uparrow} inlet, and n will determine the estimated $f_{\text{tot,mea}}$. While a larger averaging window, e.g., $n > 50$,

will narrow the distribution of $f_{\text{tot,mea}}$, a smaller averaging window, e.g., $n < 50$, will allow for more variability and a broaden PDF. Therefore, the applied n is chosen in dependence of the flight speed and the spatial resolution of the evaluated Model. In case of the IFS, n is set to 50. With an average $v_{\text{ac}} \approx 220 \text{ m s}^{-1}$, the $f_{\text{tot,mea}}$ assigned to one time-step is in the spatial range of $50 \cdot 220 \text{ m s}^{-1} = 11000 \text{ m}$, according to the grid-box size.

Precipitation Identifier

Precipitation is identified using the radar reflectivity Z provided by HAMP. Measurements are considered to be affected by precipitation, when Z exceeds a threshold of -20 dBz within 50 to 200 m above sea level (Schnitt et al., 2017). This allows to discriminate precipitation events, which affect the LWP measured by the microwave radiometer and retrieved by SMART. The simple thresholding of radar reflectivity close to the sea surface does not capture all precipitating clouds, since drizzle particles might evaporate before reaching the lower 200 m close to the sea surface.

Cloud Top Phase Identifier

Spectral measurements of upward $I_{\text{mea}}^{\uparrow}$ are applied to derive the cloud top phase (CTP) using the ratio χ_p of $I_{\text{mea}}^{\uparrow}$ at 1550 and 1700 nm wavelength:

$$\chi_p = \frac{I_{1700}^{\uparrow} - I_{1550}^{\uparrow}}{I_{1700}^{\uparrow}}. \quad (4.2)$$

This method was introduced and systematically evaluated for different cloud regimes and solar illuminations by Jäkel et al. (2013). It is based on the spectral differences in the complex refractive index of infrared radiation by liquid water and ice. A determination of the cloud's quantitative composition by liquid water and ice is not possible. Phase discrimination is done by setting a threshold for χ_p to separate between liquid water and ice. According to Jäkel et al. (2013) the thresholds are:

$$\begin{aligned} \chi_p &< -0.3 && \text{liquid water cloud} \\ \chi_p &> +0.3 && \text{ice cloud} \\ \chi_p &\text{other} && \text{mixed-phase cloud.} \end{aligned}$$

The CTP ranges from positive to negative values and is dimensionless.

4.2 Cloud Optical Thickness and Effective Radius

Based on the reflected solar radiance I_{λ}^{\uparrow} measured by SMART and the radiance ratio method proposed by Werner et al. (2013), a retrieval of τ and r_{eff} is performed. By using ratios of I^{\uparrow} from wavelength with varying sensitivity, the retrieval depends on relative rather than on absolute values of I^{\uparrow} , reducing the retrieval uncertainties. In addition, calibration and measurement uncertainties vanish and for the wavelength ratio retrieval an uncertainty of 6 % is assumed. Further on, the use of this method reduces the influence of cirrus clouds above the aircraft and increases the retrieval sensitivity with respect to r_{eff} by separating the dependence of I_{λ}^{\uparrow} on τ and r_{eff} . Forward simulations of I_{λ}^{\uparrow} , which are required in the retrieval, were carried out with the libRadtran 2.0.2 package (Emde et al., 2016).

For the retrieval of τ the 870 nm wavelength is selected and r_{eff} is determined using the ratio of 1050 nm and 1645 nm wavelength. Compared to retrievals using larger wavelength, e.g., 2100 or 3700 nm, r_{eff} derived by the SMART measurements does not only represent the cloud particles at CT. The vertical weighting function for 1600 nm covers significant amount of information from lower cloud layers (Platnick, 2000). Therefore, retrieved r_{eff} are smaller than the actual cloud droplet size at cloud top. Results from the SMART optical properties retrieval are denoted with subscript "A" in the following.

Clouds not covering the entire FOV of SMART, alter the retrieved optical properties. Lower values of I_{λ}^{\uparrow} bias τ towards lower values, whereas r_{eff} is shifted to larger droplet sizes (Cahalan et al., 1995). Further on, the heterogeneous structure of trade wind cumuli is likely to cause 3D radiative effects,

like shadowing cloud areas by nearby cloud-towers or enhanced reflectivity due to additional reflection into the FOV.

The liquid water path is obtained directly from libRadtran on the basis of Eq. (2.33) and denoted with subscript "A". In case of cloud heterogeneity, sun-glint, or 3D radiative effects, the retrieval of τ is very likely biased. Following Eq. (2.33), a bias of τ also influences the retrieval of r_{eff} and, therefore, LWP . To mitigate these effects, measurements of LWP from HAMP (denoted with subscript "B") are applied in the libRadtran radiation simulations of the cloud retrieval, as LWP data from microwave radiometers are obtained from wavelengths not influenced by sun-glint or 3D radiative effects. Using LWP from HAMP as a precondition, the Look-up-Tables of the forward simulations reduce to the absorbing wavelengths, mostly sensitive to r_{eff} . Therefore, the non-linear dependence between τ and r_{eff} is removed and the retrieval becomes more reliable. Retrieved r_{eff} from combined passive solar radiance and microwave measurements are denoted with subscript "B".

4.3 Retrieval of Cloud Droplet Number Concentration

The retrieval of N from remote sensing observations is based on the relation proposed by Brenguier et al. (2000) and Wood (2006), which links N of a stratiform cloud to τ_A and $r_{\text{eff},A}$ by:

$$N_A = \frac{\sqrt{10}}{4 \cdot \pi \cdot \sqrt{\rho_w}} \cdot \sqrt{f_{\text{ad}} \cdot \Gamma_{\text{ad}}} \cdot \frac{\sqrt{\tau_A}}{\sqrt{r_{\text{eff},A}^5}} \quad (4.3)$$

with ρ_w the density of liquid water, f_{ad} the degree of adiabaticity, and Γ_{ad} the adiabatic profile. The technique assumes an adiabatic vertical cloud profile, where temperature linearly decreases and LWC linearly increases with height. An adiabatic profile implies that the total water mass mixing ratio of the cloud is conserved. This is true when: (i) no water is removed from the cloud (no precipitation or fallout), (ii) no entrainment of dryer air at the cloud edges occurs, and (iii) no evaporation from precipitation happens. As a result, the proposed method should be applied to non-precipitating clouds only, which do not undergo strong vertical convection and mixing. A vertically constant N throughout the cloud layer is assumed. This assumption is verified for stratiform clouds and shallow trade wind cumuli by in-situ measurements, e.g., Reid et al. (1999) and Wendisch and Keil (1999). The vertically constant N is mainly determined by the amount of available Cloud Condensation Nuclei (CCN) at cloud base and their potential to form cloud droplets depending on the degree of supersaturation, which is controlled by temperature, entrainment of dry air, and updraft velocity.

The k -parameter, which relates the effective radius r_{eff} and the volumetric radius r_{vol} by:

$$k = \left(\frac{r_{\text{vol}}}{r_{\text{eff}}} \right)^3 \quad (4.4)$$

is set to $k = 0.8$ for marine clouds following the suggestion by Martin et al. (1994) and Pontikis (1996). Depending on the cloud type, the k -parameter can vary by ± 0.1 (Martin et al., 1994).

By means of the cloud properties retrieved by airborne remote sensing, Eq. (4.3) can be applied in different complexity to derive N . In the following three methods are proposed. Method A uses only SMART data, while method B additionally includes HAMP observations of LWP . Method C also involves cloud top height measurements by WALES. The obtained parameters and assumptions are summarized in Tab. 4.1.

4.3.1 Method A: Based on Cloud Optical Thickness and Droplet Effective Radius

Method A follows the traditional satellite approach to feed Eq. (4.3) with τ and r_{eff} obtained from a single passive remote sensing instrument. Here, τ_A and $r_{\text{eff},A}$ retrieved by SMART are applied. The degree of adiabaticity f_{ad} is assumed to be one. This implies, that for trade wind cumuli, which are typically sub-adiabatic, the estimated N is potentially biased. However, similar retrieval assumptions are frequently applied to observations from satellite such as MODIS (Grosvenor et al., 2018).

4.3.2 Method B: Based on Liquid Water Path and Droplet Effective Radius

Equation (2.34) allows to apply Eq. (4.3) with an independent measure of LWP instead of τ , to calculate N . As given by Wood (2006) combining Eq. (4.3) and Eq. (2.34) leads to:

$$N_B = \frac{3 \cdot \sqrt{2}}{4 \cdot \pi \cdot \rho_w} \cdot \sqrt{f_{ad} \cdot \Gamma_{ad}} \cdot \frac{\sqrt{LWP_B}}{r_{eff,B}^3}. \quad (4.5)$$

In method B, LWP measurements by HAMP and derived $r_{eff,B}$ from the combined SMART microwave-radiometer retrieval are applied. The results are denoted with N_B . Exchanging $r_{eff,A}$ by $r_{eff,B}$ takes into account that LWP is determined from HAMP only. This makes the retrieval independent of τ derived by SMART and, therefore, less sensitive to effects by sun glint. Further on, LWP determination from HAMP applies wavelengths between 20 and 100 GHz, which are not influenced by aerosol particles. An additional advantage of the determination of LWP from HAMP is the separation of clouds for different LWP and to untangle the effects of varying LWP on cloud top albedo α (McComiskey and Feingold, 2008).

4.3.3 Method C: Based on Liquid Water Path, Droplet Effective Radius, and Cloud Geometric Thickness

Equations (4.3) and Eq. (4.5) assume constant values of f_{ad} and Γ_{ad} . Therefore, in method A and B the adiabatic profile of LWC follows the maximum, theoretically possible profile under which liquid water is released due to condensation from upward motion in the atmosphere. In-situ measurements of stratocumulus and trade wind cumuli indicate that a majority of cloud profiles do not follow this adiabatic assumption (Wendisch and Keil, 1999; Merk et al., 2016). In most cases the profiles are sub-adiabatic, meaning a reduced increase of LWC with height mostly due to entrainment and mixing from dry air at the cloud edges. When convection and mixing is moderate, an equilibrium between the droplets and the surrounding air can be assumed. Entrainment and mixing reduce f_{ad} but not necessarily N . Further it might reduce the (super-)saturation at the cloud edges causing a shrinking of the droplets but not their complete vanishing. To account for a sub-adiabatic increase of LWC with height in method C, $f_{ad} \cdot \Gamma_{ad}$ is replaced by observations. Observed Γ_{calc} is determined by Eq. (2.26) with LWP_B obtained by the microwave radiometer. The cloud geometric thickness $H = h_{CT} - h_{LCL}$ is estimated from a combination of the WALES cloud top height h_{CT} observations and h_{LCL} from dropsondes.

WALES can only derive h_{CT} when the laser is attenuated by clouds with high τ . As a result, the lidar signal is attenuated soon and the cloud base height is not detectable. Therefore, $h_{CB} = h_{LCL}$ is determined separately from dropsondes. Using the temperature T and dew point temperature T_d at the two lower most points of the sounding, the lifting condensation level with $h_{LCL} \approx 125 \cdot (T - T_d)$ is approximated (Espy, 1836). Nevertheless, uncertainties of estimated h_{LCL} from dropsondes are in the range of ± 35 m not considering additional uncertainties caused by the assumptions in the equation (Romps, 2017). Alternatively, cloud boundary determination by combinations of lidar, radar, and dropsonde are applied, where: (i) the cloud droplets are large enough to produce a detectable radar echo, and (ii) no precipitation is present, but are complicated for heterogeneous cloud fields. Selection of the appropriate instrument synergy depends on the observed cloud scene. Utilization of radar observations is preferred giving the best vertical resolution for well defined cloud edges. Using the estimated Γ_{calc} given by:

$$\Gamma_{calc} = \sqrt{\frac{2 \cdot LWP_B}{H^2}}, \quad (4.6)$$

than Eq. (4.5) changes to:

$$N_C = \frac{3}{2 \cdot \pi \cdot \rho_w} \cdot \frac{LWP_B}{H \cdot r_{eff,B}^3}. \quad (4.7)$$

4.3.4 Calculation of Retrieval Uncertainty of Cloud Droplet Number Concentration

Cloud droplet number concentrations calculated with Eqs. (4.3), (4.5), and (4.7) are effected by uncertainties from τ , LWP , and especially r_{eff} , but also depend on the accuracy of k , f_{ad} , and Γ_{ad} .

To estimate the uncertainties of retrieved N , it is assumed that the errors are normally distributed and independent from each other. In this case the uncertainty of N_A from Eq. (4.3) is calculated by:

$$\Delta N = \left[\left(\frac{\partial N}{\partial k} \right)^2 (\Delta k)^2 + \left(\frac{\partial N}{\partial f_{\text{ad}}} \right)^2 (\Delta f_{\text{ad}})^2 + \left(\frac{\partial N}{\partial \Gamma_{\text{add}}} \right)^2 (\Delta \Gamma_{\text{add}})^2 + \left(\frac{\partial N}{\partial \tau} \right)^2 (\Delta \tau)^2 + \left(\frac{\partial N}{\partial r_{\text{eff}}} \right)^2 (\Delta r_{\text{eff}})^2 \right]^{0.5} \quad (4.8)$$

and analogous for Eqs. (4.5) and (4.7). All uncertainties of N presented in the following sections are based on calculation by this approach. The uncertainties of the single parameters assumed in the calculations are summarized below.

For method A, B, and C, the uncertainty of k , representing the shape of the droplet size distribution, is set to $k = 0.8 \pm 0.1$ according to the range of values suggested by Martin et al. (1994) and Pontikis and Hicks (1992).

For methods A and B the degree of adiabaticity f_{ad} is fixed to one. In that case, no uncertainty in a measurement scene is attributed to f_{ad} . For method C, the uncertainty of f_{calc} is determined by the uncertainty of h_{CT} , h_{CB} , and retrieved LWP following Eq. (2.26). Cloud top height from WALES is determined with an accuracy of $\Delta h_{\text{CT}} = \pm 20$ m. The cloud base height is derived from single dropsondes and, therefore, prone to horizontal variability of T , p , and T_d . Based on an analysis of different dropsondes in close vicinity, a cloud base height $h_{\text{LCL}} = 660 \text{ m} \pm 35 \text{ m}$ is assumed. The evaluation of all dropsondes show that the thermodynamic conditions in the selected area stayed constant ($\Delta T < 2 \text{ K}$ and $\Delta p < 4 \text{ hPa}$) during the flight time with $h_{\text{CT}} \approx 1800 \text{ m}$, $T_{\text{CT}} = 20.2^\circ \text{C}$, and $p_{\text{CT}} = 820 \text{ hPa}$. The accuracy of the deployed Vaisala dropsondes RD94 is reported to be within $\Delta T = \pm 0.2 \text{ K}$ and $\Delta p = \pm 0.4 \text{ hPa}$. Uncertainties of N_C caused by errors in Γ_{ad} are, therefore, negligible compared to the influence of τ and r_{eff} .

The adiabatic increase of LWC with height calculated from the Clausius-Clapeyron-Equation depends mostly on cloud top temperature T_{CT} and to a lower degree on cloud top pressure p_{CT} . Therefore, Γ_{ad} depends on T_{CT} and p_{CT} , too. The cloud droplet number concentration is mostly effected by the assumed T_{CT} whereby p_{CT} is only of minor contribution. Despite that, the cloud top pressure more strongly affects warm than cold clouds (Grosvenor et al., 2018). For the uncertainty calculation, a temperature difference of 2 K is considered, which changes Γ_{ad} by $\pm 0.1 \cdot 10^{-3} \text{ g m}^{-3} \text{ m}^{-1}$ for the reference value of $2.5 \cdot 10^{-3} \text{ g m}^{-3} \text{ m}^{-1}$.

The uncertainty of the retrieval of τ and $r_{\text{eff,A}}$ result from the measurements uncertainties of SMART, which are described in section 3.3.1. For typical trade wind cumuli, uncertainties of ± 0.1 for τ and $\pm 1.1 \mu\text{m}$ for $r_{\text{eff,A}}$ are assumed.

Small clouds not covering the entire FOV bias the retrieval of the optical properties towards low τ , large r_{eff} and resulting low N . Additionally, the uncertainties in r_{eff} increase for low τ . Correlation of τ and Δr_{eff} reveal, that this effect is pronounced for $\tau \leq 5$. This mostly results from the increasing influence of the ocean surface with low albedo in broken cloud regions.

From the error estimation of the N retrieval it can be concluded that uncertainties in r_{eff} , LWP , and H have to be minimized as they influence the retrieval the most. Determination of h_{CB} , either from the dropsondes or the radar, and resulting H have to be accurate within at least $\pm 60 \text{ m}$.

In addition to the measurement uncertainties, the sensitivities of the individual retrievals on τ , r_{eff} , LWP , h_{CT} , and h_{CB} have to be considered. It shows that the retrieval of LWP by SMART is sensitive for thin clouds ($LWP < 100 \text{ g m}^{-2}$) with an increasing uncertainty for optically thicker clouds caused by a reduced response of reflected I^\uparrow in case of high optical thickness. The usage of LWP from SMART for optical thin clouds is further supported by the retrieval uncertainty in LWP by HAMP for LWP values below 100 g m^{-2} . For clouds with LWP around 100 g m^{-2} both methods A and B (assuming an uncertainty of LWP derived by HAMP of about 20 %) lead to an uncertainty of N in the range of 10 cm^{-3} . In case of thicker clouds ($LWP > 100 \text{ g m}^{-2}$), method B with LWP from HAMP is used, achieving the N accuracy of $\pm 14 \text{ cm}^{-3}$ from SMART. Clouds with $LWP > 100 \text{ g m}^{-2}$ and considerable geometric thickness ($H > 1500 \text{ m}$), HAMP retrieved LWP becomes more representative as the retrieval represents the entire cloud and not only CT properties observed by SMART. Common satellite-based microwave radiometer retrievals of LWP above 180 g m^{-2} are error-prone because of their large footprint. With the smaller footprint of HAMP these uncertainties in LWP are reduced, resulting in a lower uncertainty in retrieved N_B and N_C .

Table 4.1: Overview of the cloud droplet number concentration retrievals and applied measurements, retrieval parameters, and assumptions.

Method	A	B	C
Instruments and Parameters			
SMART	$\tau_A, \tau_{\text{reff},A}$	$\tau_{\text{reff},B}$	$\tau_{\text{reff},B}$
HAMP	\times	LWP	LWP
WALES	\times	\times	f_{calc}
Assumptions			
adiabatic cloud-profile	\checkmark	\checkmark	\times
adiabatic change of LWC	$f_{\text{ad}} \cdot \Gamma_{\text{ad}} = 2.5 \cdot 10^{-3} \text{ g m}^{-3} \text{ m}^{-1}$		Γ_{calc}
k -parameter	$k = 0.8$	$k = 0.8$	$k = 0.8$
const. N	\checkmark	\checkmark	\checkmark
deep convection	\times	\times	\times
cloud homogeneity	\checkmark	\checkmark	\checkmark
precipitation	\times	\times	\times
minimum horizontal size	$\approx 150 \text{ m}$	$\approx 150 \text{ m}$	$\approx 150 \text{ m}$
Estimated total uncertainties	$\Delta N_A = \pm 7.1 \text{ cm}^{-3}$	$\Delta N_B = \pm 14.1 \text{ cm}^{-3}$	$\Delta N_C = \pm 15.1 \text{ cm}^{-3}$

The retrievals of $r_{\text{eff},B}$ from combined measurements of SMART and HAMP are slightly more prone to the uncertainty of the LWP_B measurements and lead to uncertainties of $r_{\text{eff},B}$ of up to $\pm 1.5 \mu\text{m}$, being slightly higher than r_{eff} estimated for method A. However, the uncertainty of N with respect to r_{eff} is lower as the sensitivity of N_B with respect to $r_{\text{eff},B}$ is lower in Eq. (4.5) compared to Eq. (4.3). The sensitivity study leads to the conclusion, that an appropriate retrieval of r_{eff} is the most important factor for the calculation of N .

For the exemplary ideal adiabatic case study discussed in above, the total uncertainties of the three methods are for $\Delta N_A = \pm 7.1 \text{ cm}^{-3}$, $\Delta N_B = \pm 14.1 \text{ cm}^{-3}$, and $\Delta N_C = \pm 15.1 \text{ cm}^{-3}$. For sub-adiabatic clouds, the uncertainties of method A and B increase due to the assumption of adiabaticity. The additional error in N results from the increased variability in f_{ad} .

4.4 Application of CDNC Retrieval on NARVAL-II Flight

The retrieval of N is applied to a section of research flight 06 RF06 of NARVAL-II (see Fig. 3.7). The presence of intense sun-glint is visible, which enhances the reflected radiance I_{λ}^{\uparrow} and influences the cloud detection (low contrast) and the retrieval of τ and $r_{\text{eff},A}$ by SMART. The general weather situation was characterized by moderate convection with low cloud top altitudes. Locally more dense cloud fields formed, at about 10°N and 16°N at 55°W . The north eastern part of the flight track (upper circles) was dominated by aggregated trade wind cumuli, whereby in the south-western part (lower circles) individual shallow cumuli were present.

Time series of measured and retrieved parameters are shown in Fig. 4.1. The three methods to calculate N assume that there is no precipitation present. Because measured Z is most sensitive to large cloud droplets, it can not be guaranteed that drizzle is excluded completely. Estimation of the drizzle rate on basis of H and N as proposed by Pawlowska and Brenguier (2003) and vanZanten et al. (2005) is not possible as retrieved N is biased by the process of drizzle formation and, therefore, not applicable with the presented instrument setup of HALO. Flight sections which are flagged for precipitation are highlighted by the gray boxes. At the top of Fig. 4.1 the cloud mask (blue) and the homogeneity cloud flag (yellow) are indicated. Images of RGB composites by specMACS are given in the lower part of the plot to illustrate the visual cloud characteristics. Data gaps are due to cloud free pixel.

The selected cloud case (CC) represents a heterogeneous single-layer cloud, observed between 19:29 and 19:32 UTC. This section shows moderate convection with the likelihood of slight precipitation. In these areas, the criteria for cloud homogeneity is not fulfilled. Despite that, calculation of N is performed, knowing that the retrieval of N using method A and B are prone to errors under this circumstance. The results are used to evaluate the improvement of retrieved N by method C, which accounts for cloud geometry and sub-adiabaticity. By comparing convective and non-convective areas

of this CC, the limitations and advantages of the three methods are investigated. Mean values of the measured and retrieved parameters from the three different methods, separated for non-precipitation and precipitation are summarized in Tab. 4.2.

For the non-precipitating and homogeneous part of the CC, τ does not exceed a value of 30 and $r_{\text{eff,A}}$ and $r_{\text{eff,B}}$ range between 18 and 40 μm (Fig. 4.1a, b). Retrieved LWP from SMART and HAMP (Fig. 4.1c) agrees within the uncertainty range of HAMP for most parts of the homogeneous cloud sections. Larger differences appear around 19:29:30 UTC where LWP_A is larger than LWP_B . For method C, cloud geometrical thickness H is calculated from a combination of HAMP and WALES. Radar reflectivity Z is above the precipitation detection threshold of -20 dBZ and allows to determine vertical profiles of the LWC and h_{CB} with an average value of $h_{\text{CB}} \approx 900$ m where no precipitation is present. Cloud top height h_{CT} from WALES ranges between 200 and 1000 m for the non-precipitating regions. This results in a highly variable f_{calc} , which varies between strongly varies between 0.05 and 1.0.

Cloud droplet number concentration from method A and B calculated for this CC are generally low (see also Tab. 4.2), mostly ranging between 20 and 40 cm^{-3} . Together with large $r_{\text{eff,A}}$ and $r_{\text{eff,B}}$ these values indicate typical pristine maritime clouds. An exception is observed around 19:29:30 UTC, when N peaks up to 120 cm^{-3} for all three methods, mostly resulting from a decrease of $r_{\text{eff,A}}$ and an increase of τ . The decrease in r_{eff} might result from 3D-radiative effects at the cloud edge overestimating the cloud particle size, and biasing the retrieval of N .

In precipitation marked areas, retrieved τ , LWP_A , and LWP_B are higher compared to the precipitation free regions, while $r_{\text{eff,A}}$ and $r_{\text{eff,B}}$ are in the same range as for the non-precipitating areas. In contrast to the homogeneous parts of the cloud, the convective regions show stronger horizontal heterogeneity in all parameters. The optical thickness reaches up to 40 and $r_{\text{eff,A}}$ ranges from 20 to 38 μm . In these areas the LWP_B from HAMP exceeds 270 g m^{-2} and shows a maximum value up to 500 g m^{-2} . Liquid water path from SMART is in the same range of LWP_B except for the first precipitation section (19:30:30 UTC) where LWP_B is lower than LWP_A . For the precipitating regions the cloud base height h_{CB} is assumed to be at the same level as determined for the non-precipitating regions as precipitation makes the cloud base invisible for the radar. The cloud geometric thickness H is slightly higher for the connective regions and ranges between 800 and 1300 m. The calculated adiabaticity f_{calc} is lower than 0.5 for the majority of the measurement and shows that most parts of the cloud are sub-adiabatic. For the precipitation regions calculated N are between 10 and 90 cm^{-3} with the highest concentrations for method B, followed by method A and the lowest N for method C. In the areas with precipitation, N shows a systematic higher variability, which is observed by all three methods and likely caused by the variability of r_{eff} retrieved from SMART. One reason for this variability is the relation of r_{vol} to r_{eff} , which is assumed to be (i) constant in the retrieval of r_A and r_B and (ii) significantly influenced by formation of precipitation. Therefore, calculated N by all three methods are highly prone to errors for precipitating clouds. The variability of N might also be caused by intense turbulent mixing processes within the cloud. Concluding from that, it is suggested to filter areas with stronger convection, precipitation, and heterogeneous scenes and analyze the retrieved N with special care.

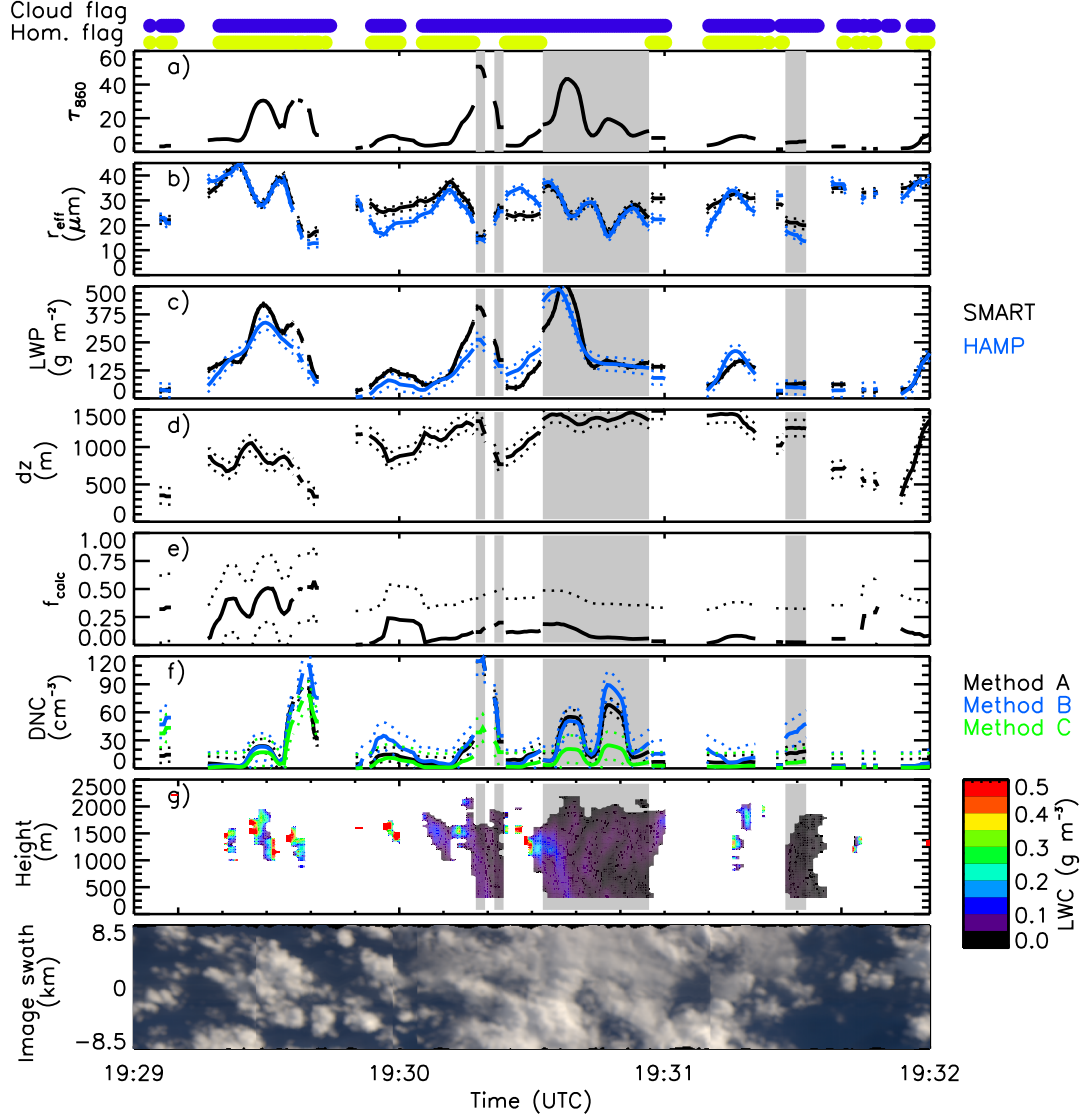


Figure 4.1: Time series of measured and retrieved cloud properties from NARVAL-II RF06 between 19:29 and 19:32 UTC. Panels show a) cloud optical thickness τ_{850} , b) cloud droplet effective radius r_{eff} , c) liquid water path LWP , d) cloud geometric thickness dz , e) calculated adiabaticity f_{calc} , f) cloud droplet number concentration N , g) liquid water content LWC , and in h) an image in the visible wavelength range. At the top, the cloud mask (blue) and the homogeneity cloud flag (yellow) derived by SMART are indicated.

Table 4.2: Mean values of cloud properties of the presented cloud section.

parameter	non-precipitating	precipitating (p)
τ	3.5	11.3
$r_{\text{eff,A}} [\mu\text{m}]$	30.4	24.9
$r_{\text{eff,B}} [\mu\text{m}]$	29.1	23.4
$LWP_A [\text{g m}^{-2}]$	135	226
$LWP_B [\text{g m}^{-2}]$	120	210
$H [\text{m}]$	959	1315
$N_A [\text{cm}^{-3}]$	17	47
$N_B [\text{cm}^{-3}]$	25	53
$N_C [\text{cm}^{-3}]$	13	40

4.5 Statistical Analysis of Liquid Water Path, Droplet Effective Radius, and Number Concentration

Statistics of retrieved cloud properties are analyzed for measurements between 19:24 and 19:39 UTC only, when the HCF indicates homogeneous clouds and uncertainties of the retrieved cloud parameters are low. However, in total 700 individual measurements are included, which represents a cloud field of 77 km length. The clouds were separated into precipitating (p) and non-precipitating (np) pixel. Mean values of the parameters for each measurement are summarized in Tab. 4.2.

Figure 4.2a and Fig. 4.2b show normalized probability density functions (PDFs) of the calculated N for non-precipitating (a) and precipitating regions (b) of the selected flight-leg from all three methods A, B, and C. For non-precipitating clouds (Fig 4.2a) the distribution of N_A peaks at $N_A \approx 30 \text{ cm}^{-3}$ with a steep decrease towards a concentration of $\approx 100 \text{ cm}^{-3}$. The first local maximum of the N_B distribution is at $N_B \approx 30 \text{ cm}^{-3}$ slowly decreasing for larger N . Only a slight difference between N_A and N_B is present for higher N_A . This can be explained by the slightly higher values of SMART LWP_A compared to HAMP LWP_B . The PDFs of N_A and N_B show reasonable results for pristine, maritime clouds with relative large $r_{\text{eff,A}}$ and according low N from method A and B. Cloud droplet number concentration from method C are significantly lower as a result of the considered adiabaticity of the individual clouds.

Measurements affected by precipitation (see Fig. 4.2b) compared to Fig. 4.2a show almost the same distribution with a shift to larger N for all three calculation methods, especially for method C. Filtering for precipitating clouds, the statistic might be biased by only considering further developed clouds, in which precipitation formation changes and broadens the droplet size distribution. This leads to differences in the means of r_{vol} and r_{eff} , influencing the k -parameter, which is assumed to be 0.8 in the N calculation. Retrieving k by passive remote sensing is not possible yet (Wood, 2006).

Figure 4.3a and Fig. 4.3b show the cloud top reflectivity \mathcal{R}_{532} measured by SMART at 532 nm as a function of N_B retrieved from combined SMART and HAMP measurements. Only measurements of the flight leg where no precipitation was observed are presented. The data is binned for two different $LWPs$. Figure 4.3a shows clouds with LWP between 0 and 50 g m^{-2} , and Fig. 4.3b shows clouds in the range between 50 and 100 g m^{-2} . Colors represent $r_{\text{eff,B}}$ binned from 5 to $30 \mu\text{m}$ in $5 \mu\text{m}$ steps (label in Fig. 4.3 refers to the mean bin value). The red lines in Fig. 4.3 indicate radiative transfer simulations by libRadtran of theoretical $\mathcal{R}_{532,\text{sim}}$ for clouds of the same LWP are added by the red line. For the thin clouds in Fig. 4.3a the measured \mathcal{R}_{532} shows a clear increase for higher N_B over the entire measurement range. This correlation is less pronounced for the thicker clouds in Fig. 4.3b due to a reduced range of \mathcal{R}_{532} and N , and the observations may not cover the entire natural variability. However, for both cloud sub-samples, the measurements follow the theoretical line given by the simulations only that the measured \mathcal{R}_{532} are too low or retrieved N to high. Both might be attributed to measurement biases: either the radiometric calibration of SMART or the retrieved LWP_B and $r_{\text{eff,B}}$, which feed the calculation of N_B . Additionally, the homogeneous assumption of cloud properties applied in the RTS can lead to an overestimation of $\mathcal{R}_{532,\text{sim}}$ compared to the

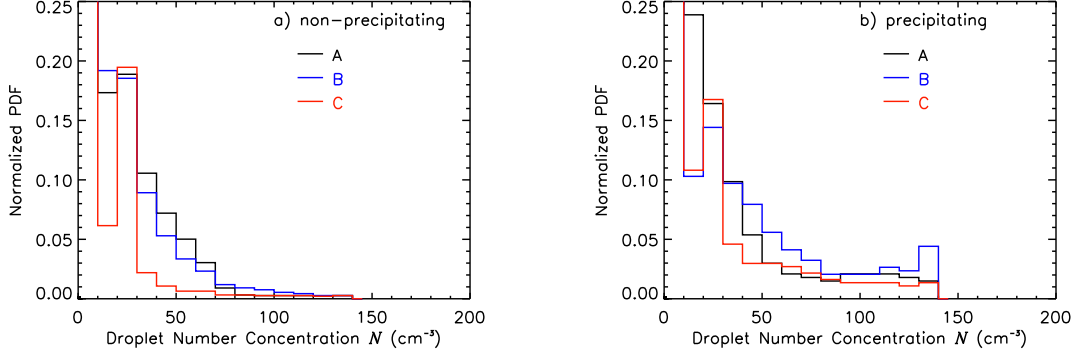


Figure 4.2: Normalized probability density function of the cloud droplet number concentration N for the selected flight path using method A, B, and C. Distributions are filtered for non-precipitating a) and precipitating b) clouds.

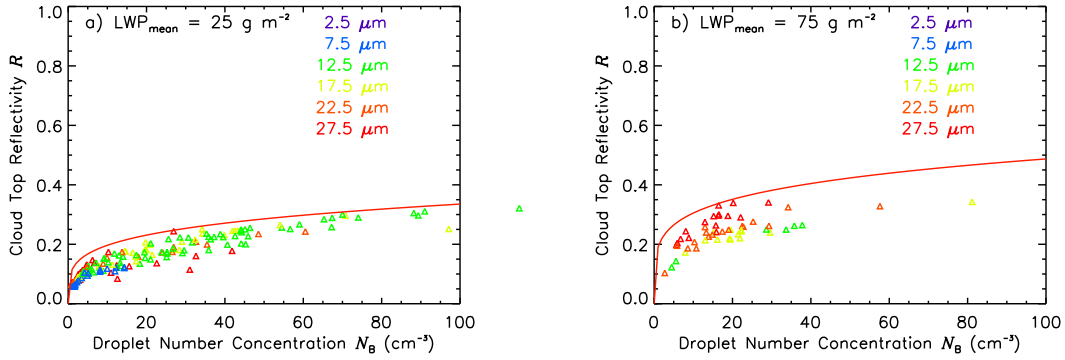


Figure 4.3: Cloud top reflectivity \mathcal{R}_{532} as a function of cloud droplet number concentration N_B for homogeneous, non-precipitating clouds of different liquid water path LWP_B (panel a: $0 - 50 \text{ g m}^{-2}$, panel b: $50 - 100 \text{ g m}^{-2}$). The droplet effective radius r_{eff} of each measurement is indicated by the color code. The red line represents simulated reflectivity \mathcal{R}_{532} from radiative transfer calculations for clouds with same LWP .

measurements. The subdivision of data for different $r_{\text{eff},B}$ shows that clouds in an early developing state with low LWP_B (Fig. 4.3a) are dominated by smaller cloud droplets up to $r_{\text{eff},B} = 17.5 \mu\text{m}$ whereby clouds in a later development state with higher LWP_B (Fig. 4.3b) are dominated by cloud droplets larger than $r_{\text{eff},B} = 17.5 \mu\text{m}$.

5 Simulations and Measurements Along HALO Flight Tracks

In this chapter the method and model setup for simulating upward and downward irradiances $F_{\lambda}^{\uparrow\downarrow}$ with ecRad and libRadtran are presented. The radiative transfer simulations (RTS) are performed along the flight track and altitude of HALO. Focus is on the spectral wavelength region between 266 and 2050 nm measured by SMART, covering nearly 95% of the solar spectrum (Petty, 2006). The RTS are performed using gridded hourly analysis data (AD) of the Integrated Forecast System (IFS) of the European Center for Medium Range Forecast (ECMWF).

5.1 IFS Analysis Data

NWP models provide two different types of atmospheric model data-sets describing the Earth's atmosphere at a given time.

Re-analysis data are re-calculated data sets of the atmospheric state, at a later time point than the original forecast run, whereby all data-sets utilize the same assimilation method. An example would be a re-analysis performed on 22 January 2019 and issued for 26 September 2016 on basis of the assimilation method, which is operational on the 22 January 2019. These re-analysis results are consistent back in time with respect to the utilized assimilation technique. Due to the computational effort re-analysis data are available in a reduced spatial and temporal resolution only. In case of the best ECMWF Re-Analysis Version 5 (ERA5) data, the temporal resolution is one hour with a spatial resolution of 30 km (Hersbach et al., 2018).

For precise simulations of radiative fluxes, it is inevitable to know the state of the Earth's atmosphere as accurate as possible. Using the example from above, the applied IFS AD are created on the 26 September 2016 giving the best temporal and spatial resolution. During NARVAL-II and NAWDEX the IFS version 'Cr41r2' was operational and used for the data assimilation.

The provided IFS AD are stored in NetCDF files with a temporal resolution of one hour and a horizontal resolution of 0.1° . The horizontal resolution of the model grid given in kilometers depends on the position on the Earth, as the distance between neighboring grid-points of equal latitude / longitude increases from the pole to the equator and the horizontal resolution decreases towards the equator. On average, e.g., at 40° N where the NAWDEX campaign was centered, the given resolution of 0.1° leads to a spatial resolution between 9 and 11 km. For the RTS only the 99 lower most model levels are used, with the highest level at around 28 hPa, approximately 28 km according to the U.S. standard atmosphere, describing the stratosphere sufficiently to simulate the radiation at flight altitude.

All provided parameters from the IFS analysis data are listed in Tab. 5.1.

5.2 ecRad Model Setup

ecRad is installed on the servers of the Leipzig University. This allows to repeat the simulations for different initial conditions. To specify the boundary conditions and to control ecRad, a namelist file is used (see Appendix 7.1). Due to the openIFS offline version the operational host system is missing, which handles the data input and output for ecRad. Therefore, the required input variables for ecRad, which are not available from the analysis data, e.g., liquid $r_{\text{eff,liq}}$ and ice effective radius $r_{\text{eff,ice}}$, have to be provided alternatively to ecRad, which is realized by a local host system.

5.2.1 Input Data for ecRad Simulations

Simulations of F along the flight track require the extraction of cross-sections from the 3D fields of IFS AD according to time and position of the aircraft. It is based on the nearest neighbor method

Table 5.1: List of all provided parameters from the IFS analysis data with their long names, symbols, and units for the radiative transfer simulations.

Variable	Symbol	Unit
Specific humidity	q	kg kg^{-1}
Specific liquid water content	q_{liq}	kg kg^{-1}
Specific ice water content	q_{ice}	kg kg^{-1}
Specific rain water content	q_{rw}	kg kg^{-1}
Specific snow water content	q_{sn}	kg kg^{-1}
Temperature	T	$^{\circ}\text{C}$
u-wind component	u	m s^{-1}
v-wind component	v	m s^{-1}
10 m u-wind component	$u10$	m s^{-1}
10 m v-wind component	$v10$	m s^{-1}
ω -wind component	ω	Pa s^{-1}
Surface pressure	p_{S}	hPa
Sea-level pressure	p_{SLP}	hPa
Pressure	p	hPa
Cloud cover	FCC	0 - 1
Skin / Surface temperature	T_{S}	$^{\circ}\text{C}$
Land-Sea-Mask	LSM	0 - 1

with a temporal resolution of two seconds. With an average ground speed around $v_{\text{ac}} = 220 \text{ m s}^{-1}$ this leads to a spatial representation of the simulations of 440 m. To account for temporal changes the IFS AD are linearly interpolated in time between two enclosing IFS AD files for each simulation step. All mandatory parameters for the RTS are listed in Tab. 5.2. Missing parameters for ecRad are calculated by the local host system following the equations in the IFS documentation (ECMWF, 2016b).

Aerosol, Surface Albedo, and Top of Atmosphere Solar Irradiance

Offline simulations by ecRad do not include aerosol climatologies. The analyzed flights were performed at altitudes above 11 km height, where aerosol concentrations are commonly low and the contribution due to scattering and absorption by aerosol is negligible. During RF04 of NAWDEX the measurement area was not influenced by aerosols advection of any kind. For NARVAL-II RF06 aerosol contributions can not be fully omitted.

RF04 of NAWDEX and RF06 of NARVAL-II were performed over open ocean. Therefore, the sea surface albedo α_{sea} in dependence of the solar zenith angle θ_0 is parameterized for every simulation step by:

$$\alpha_{\text{sea}} = \frac{0.037}{1.1 \cdot \cos(\theta_0)^{1.4} + 0.15} \quad (5.1)$$

following Taylor et al. (1996). Calculated α_{sea} are used in the simulations by ecRad and libRadtran.

The mean downward solar irradiance $F_{\text{TOA,eR}}^{\downarrow}$ at the top of the model atmosphere is adjusted according to the date of the research flight to consider the annual variation of the Earth-Sun-distance.

Table 5.2: List of mandatory variables, which have to be provided to ecRad. Variable names from ecRad, array dimensions, and descriptions are given. Table is adapted from the 'ecRad' manual by Hogan, 2018.

Variable	Dimension	Description
solar_irradiance	-	Solar irradiance at Earth's orbit (W m^{-2})
skin_temperature	col	Skin temperature (K)
cos_solar_zenith_angle	col	Cosine of solar zenith angle
sw_albedo	col, sw_albedo_band	Shortwave albedo (if 1D then assumed spectrally constant)
lw_emissivity	col, lw_emiss_band	Longwave emissivity (if 1D then assumed spectrally constant)
pressure_hl	col, half_level	Pressure at half levels (Pa)
temperature_hl	col, half_level	Temperature at half levels (K)
q	col, level	Specific humidity (kg kg^{-1})
o3_mmr	col, level	Ozone mass mixing ratio (kg kg^{-1})
o3_vmr	col, level	Ozone volume mixing ratio (kg kg^{-1})
q_liquid	col, level	Liquid cloud mass mixing ratio (kg kg^{-1})
q_ice	col, level	Ice cloud mass mixing ratio (kg kg^{-1})
re_liquid	col, level	Liquid cloud effective radius (m)
re_ice	col, level	Ice cloud effective radius (m)
overlap_parameter	col, level_interface	Cloud overlap parameter
fractional_std	col, level	Fractional standard deviation of cloud optical depth
inv_cloud_effective_size	col, level	Inverse of cloud effective horizontal size for SPARTACUS solver (m^{-1})
aerosol_mmr	col, aerosol_type, level	Aerosol mass mixing ratio (kg kg^{-1})

Clouds

In the IFS clouds are described by the prognostic variables cloud fraction f , specific liquid water content q_{liq} , specific ice water content q_{ice} , specific rain water content q_{rw} , and specific snow water content q_{sn} . The IFS cloud module uses these variables to parameterize the mean effective radius of liquid water droplets $r_{\text{eff,liq}}$ and ice crystals $r_{\text{eff,ice}}$. In offline mode $r_{\text{eff,liq}}$ and $r_{\text{eff,ice}}$ are calculated by the local host system, using the operational IFS routines, which are provided within the ecRad software package. The source-code is attached in the Appendix. To be consistent with the deviating variable declarations in this thesis and the IFS subroutines, the List of Symbols in the Appendix provides the variable names used in the source code, the symbols used in this thesis, the describing longnames, and the according units.

In the latest version of the IFS model, monthly CCN climatologies are used, representing the spatial and temporal patterns of global CCN. All analyzed NARVAL-II and NAWDEX flights were performed over open ocean and, therefore, a fixed value of 50 cm^{-3} CCN is applied (Martin et al., 1994), which was used in the operational IFS simulations until version Cy32r1. The cloud droplet number concentration N is determined as a function of CCN, q_{liq} , and q_{rw} , and than utilized in the parameterization for $r_{\text{eff,liq}}$. For liquid water clouds $r_{\text{eff,liq}}$ is calculated as a function of q_{liq} , q_{rw} , the cloud condensation nuclei (CCN) concentration, and the cloud droplet size dispersion k_{cld} based on Martin et al. (1994).

Ice effective radius $r_{\text{eff,ice}}$, effective diameter D_{eff} , the mass-size-relation, and according cloud optical properties of an ice particle are described and calculated according to the definitions of Fu (1996) and Fu et al. (1998a). Detailed descriptions of $r_{\text{eff,liq}}$ and $r_{\text{eff,ice}}$ are given in ECMWF (2016b) and ECMWF (2016a).

5.2.2 Output from ecRad Simulations

Resulting simulated vertical profiles of spectral and broadband $F^{\uparrow\downarrow}$ are stored in individual NetCDF files for every time-step. A detailed list of the output parameters and the structure are given in Tab. 5.3.

Preparation of the Simulated Irradiance profiles

For the comparison with the aircraft observations the vertical profiles of $F^{\uparrow\downarrow}$ are loaded from `spectral_flux_up_sw` and `spectral_flux_dn_sw` of the individual simulations. The vertical spectral fluxes of $F^{\uparrow\downarrow}$ are extracted and linearly interpolated onto the HALO flight altitude. For broadband comparison the spectral bands #12 (263.2 nm) to #4 (2150 nm) (see Fig. 2.6) are integrated and refereed as broadband $F_{\text{BB,eR}}^{\uparrow\downarrow}$ in the following. Band resolved $F^{\uparrow\downarrow}$ are denoted with $F_{\text{Bi,eR},x}^{\uparrow\downarrow}$, with i the band number and x the applied ice parameterization.

Modeled Total Cloud Cover

The total cloud cover $f_{\text{tot,eR}}$ in ecRad is diagnosed by the radiative transfer solver from the fractional cloud cover f of each vertical level in the model column and depends on the selected cloud overlap assumption (COA). Detailed description of the COAs are given in ECMWF (2016b).

Cloud Top Height Determination from ecRad

Radiation measured above homogeneous, optically thick clouds ($\tau > 2$) is predominantly influenced by the upper most cloud layers. In the visible wavelength range the influence on upward F due to underlying multiple cloud layers is assumed to be negligible. Therefore, the macrophysical and microphysical properties, e.g., N , LWC , and r_{eff} , at cloud top mostly determine F^{\uparrow} and are extracted from the upper most cloud-containing grid-box in the IFS AD.

The cloud top height (CTH) is determined by allocating the upper most model level with measurable

Table 5.3: List of output variables from ecRad simulations. Variable names from ecRad, array dimensions and descriptions are given. Description is shortened with up = upward, dn = downward, sw = shortwave

Variable	Dimension	Description
pressure_hl	col, half_level	Pressure at half levels (Pa)
flux_up_sw	col, half_level	Up sw flux (W m^{-2})
flux_dn_sw	col, half_level	Down sw flux (W m^{-2})
flux_dn_direct_sw	col, half_level	Down direct sw flux (W m^{-2})
flux_up_sw_clear	col, half_level	Up clear-sky sw flux (W m^{-2})
flux_dn_sw_clear	col, half_level	Down clear-sky sw flux (W m^{-2})
flux_dn_direct_sw_clear	col, half_level	Down clear-sky direct sw flux (W m^{-2})
spectral_flux_up_sw	col, half_level, band	Spectral up sw flux (W m^{-2})
spectral_flux_dn_sw	col, half_level, band	Spectral down sw flux (W m^{-2})
spectral_flux_dn_direct_sw	col, half_level, band	Spectral down direct sw flux (W m^{-2})
spectral_flux_up_sw_clear	col, half_level, band	Spectral up clear-sky sw flux (W m^{-2})
spectral_flux_dn_sw_clear	col, half_level, band	Spectral down clear-sky sw flux (W m^{-2})
spectral_flux_dn_direct_sw_clear	col, half_level, band	Spectral down clear-sky direct sw flux (W m^{-2})
cloud_cover_sw	col, half_level	Total cloud cover diagnosed by sw solver

radiative impact on the profile of F . For each column of F_{eR}^\uparrow the first

$$F_{\text{eR}}^{\uparrow'} = \frac{F_{\text{eR}}^\uparrow}{dh}$$

and second

$$F_{\text{eR}}^{\uparrow''} = \frac{d^2 F_{\text{eR}}^\uparrow}{dh^2}$$

derivative is calculated. The first derivation is the change of F_{eR}^\uparrow with height. The upper most local maxima in vertical $F_{\text{eR}}^{\uparrow'}$ approximates the middle of the cloud layer. $F_{\text{eR}}^{\uparrow''}$ gives the position of the inflection point of F_{eR}^\uparrow , which is assumed to represent the upper part of the designated cloud layer. In case of multiple cloud layers within a single column the highest model layer is flagged as cloudy, where a threshold of $F_{\text{eR}}^{\uparrow''} > \pm 1 \cdot 10^{-5}$ is exceeded.

Cloud Top Phase Determination from Model

The cloud top phase (CTP) is determined by the dominating fraction of specific liquid water mixing-ratio q_{liq} or specific ice water mixing-ratio q_{ice} at CTH. The CTP ratio $\chi_{\text{p,eR}}$ is calculated from:

$$\chi_{\text{p,eR}} = \frac{q_{\text{liq}}}{q_{\text{liq}} + q_{\text{ice}}}, \quad (5.2)$$

which allows to differentiate for the dominant water phase at CT. A ratio of 0 represents clouds with ice water at CT, while a $\chi_{\text{p,eR}}$ of 1 is an indicator for pure liquid water.

Cloud Top Radius from Model

Cloud top radius $r_{\text{eff,eR}}$ is extracted from the columnar profile of $r_{\text{eff,eR}}(i)$ at height level i , which is flagged as the CTH, and $i - 1$. Then $r_{\text{eff,eR}}(i)$ and $r_{\text{eff,eR}}(i - 1)$ are averaged to obtain an estimate of $r_{\text{eff,eR}}$ from the two upper most cloud layers, to account for the penetration depth of solar radiation.

5.3 Sensitivity of ecRad to Variations in IFS Input-Data

The accuracy of the simulated upward and downward irradiances $F^{\downarrow\uparrow}$ depends on the IFS AD provided by the IFS data assimilation. The comparison of measured and simulated $F^{\downarrow\uparrow}$ bases on the assumption that the IFS AD represents the actual condition of the atmosphere during the flight as close as possible. Despite a temporal resolution of one hour and a spatial resolution of $0.1^\circ \approx 11 \text{ km}$, differences between the AD and the atmospheric state on smaller scales will be present.

To estimate the influence of potential variances in temperature T , cloud fraction f , humidity q , liquid water content LWC and ice water content IWC as well as calculated liquid effective radius $r_{\text{eff,liq}}$ and ice effective radius $r_{\text{eff,ice}}$ on the simulated $F^{\downarrow\uparrow}$, a sensitivity study for a pure ice section of NAWDEX RF04 and a liquid water cloud section of NARVAL-II RF06 is performed. The selected ice cloud was measured between 13:36 and 13:53 UTC representing a homogeneous ice cloud. The liquid water cloud segment was observed between 14:10 and 14:43 UTC as an example for a heterogeneous liquid-water cloud. Both sections are averaged in time for each parameter of the IFS AD and model level. The resulting averaged vertical profile is used as the reference profile (RP), representing the chosen cloud section. The along-track variance in the IFS AD parameters represents the natural variability within the cloud. To estimate the influence of each parameter on simulated $F^{\downarrow\uparrow}$, 12 individual vertical profiles are created by changing the RP for each parameter and the along-track variance. Then $F^{\downarrow\uparrow}$ is simulated for the RP and the 12 profiles. For heterogeneous low-level liquid water trade wind cumuli, cloud-free regions are excluded to consider for cloud variances only.

Resulting relative deviations ψ for each cloud microphysical property of the ice (black) and liquid water cloud (gray) are shown in Fig. 5.1. For both cloud cases the maximum deviation in F^\uparrow of up to $\pm 12\%$ results from the fractional cloud cover f , which distributes the mean cloud water content

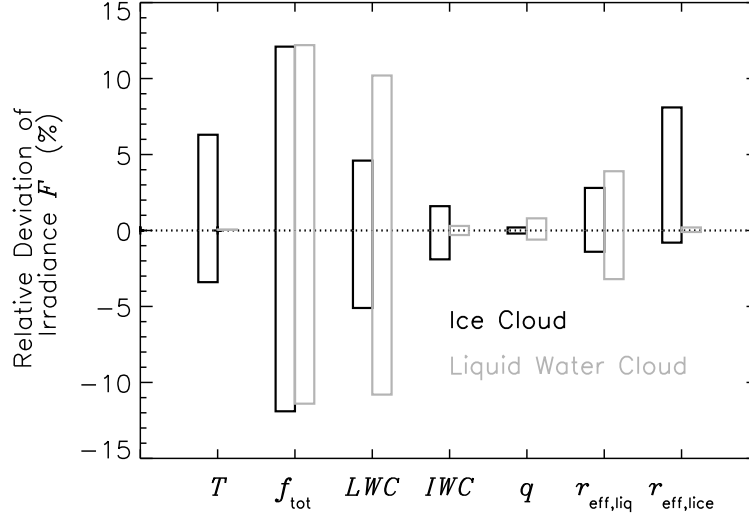


Figure 5.1: Relative deviations ψ of simulated solar upward irradiance F^\uparrow at flight altitude from ecRad between the mean atmospheric reference profile and 12 varied profiles of temperature T , cloud fraction f , humidity q , liquid water mixing-ratio q_{liq} , ice mixing-ratio q_{ice} , liquid effective radius $r_{\text{eff,liq}}$, and ice effective radius $r_{\text{eff,ice}}$. The differences for the ice cloud are plotted in black and the liquid water cloud are plotted in grey.

within the grid-box and, most important, scales simulated F within the grid-box, to account for partly filled grid-boxes. Therefore, a well prognosed f is crucial for accurate radiation calculations.

The effect of the other AD parameters on ψ is lower and is different for the ice and liquid water cloud. A change of the temperature profile has a significant impact on ψ for the ice cloud of 6 %, but is negligible for the liquid water case.

The relative deviation of F for the liquid water cloud due to changing IWC is below 0.1 %, while variations in LWC cause ψ of up to 10 %. Relative deviations of F for the ice water cloud due to changing IWC and LWC are 2 % and 5 %, respectively. Changes of the humidity profile q have only a minor influence and are assumed to be negligible compared to the other uncertainties.

For $r_{\text{eff,ice}}$ and $r_{\text{eff,liq}}$ the along-track variance was $\pm 7 \mu\text{m}$ and $\pm 5 \mu\text{m}$, respectively. In the ice cloud case this causes a relative deviation of F^\uparrow by 3 % for $r_{\text{eff,liq}}$ and 8 % for $r_{\text{eff,ice}}$. For the liquid cloud case the relative difference of F^\uparrow is 4 % for $r_{\text{eff,liq}}$ and 0.1 % for $r_{\text{eff,ice}}$.

From the sensitivity study it is concluded that f contributes to uncertainties in modeled F the most followed by the water content and calculated r_{eff} . For all 12 profiles of the cloud case a maximum absolute deviation of $\pm 50 \text{ W m}^{-2}$ and for the liquid cloud case of $\pm 20 \text{ W m}^{-2}$ is determined. For cloud-free situations the uncertainties in F^\uparrow are in the range of $\pm 5 \text{ W m}^{-2}$. These absolute differences represent the combined model uncertainties due to the IFS AD and the RTS, and are regarded as the models uncertainty range.

5.4 libRadtran

5.4.1 Input Data for libRadtran Simulations

For libRadtran simulations the extraction of vertical profiles from the 3D IFS AD is performed analog to ecRad. The vertical atmospheric structure of the pressure levels and the vertical resolution of the IFS AD are adapted for libRadtran ensuring the same vertical and spatial distribution, to be coherent with the ecRad set-up and atmosphere layering. In that way possible deviations in the simulations resulting from the simulations set-up are minimized. The specifications for the libRadtran simulations are provided by a namelist file. An example file is given in the Appendix 7.2.

Calculation of Geometric Height from Pressure Levels

Commonly, NWP models use pressure as a vertical coordinate. libRadtran requires the geometric height h_{geo} , which is calculated from the the pressure levels i on basis of the barometric formula and the International Standard Atmosphere (ISA) by:

$$h_{\text{geo}}(i) = \frac{-p_s \cdot \ln\left(\frac{p(i)}{p_s}\right)}{\rho_{\text{air}} \cdot g_{\text{geo}}} \quad (5.3)$$

with p_s the surface pressure, $p(i)$ the pressure at the given levels, $\rho_{\text{air}} = 1.292 \text{ kg m}^{-3}$ the density of air (1013.25 hPa, 15.0°), and $g_{\text{geo}} = 9.81 \text{ m s}^{-2}$ the average gravitational acceleration of the Earth.

Atmosphere and Cloud Fraction File

The atmosphere file for libRadtran contains vertical profiles of h_{geo} in km, pressure p in hPa, temperature T in K, and gas density of air, O₃, O₂, CO₂, and NO₂ in units of cm^{-3} .

The cloud fraction file specifies the vertical profile of fractional cloud cover f_i for each model level i . Data for atmosphere and cloud fraction are adapted from the IFS AD.

Liquid Water and Ice Water Files

The liquid water content $LWC(i)$ of a grid-box i is calculated from the temperature T , the specific liquid water content q_{lw} , the specific rain water content q_{rw} , the specific gas constant for dry air R_{dry} , and the air density ρ_{air} of the grid-box by

$$LWC(i) = \frac{p(i)}{R_{\text{dry}} \cdot T(i) \cdot (1 + 0.6078 \cdot q(i))} \cdot (q_{\text{lw}}(i) + q_{\text{rw}}(i)). \quad (5.4)$$

Specific liquid water content q_{lw} and q_{rw} are summed up as libRadtran does not treat them separately (ECMWF documentation Part IV (page 201)). This implicitly assumes that liquid water droplets and rain droplets have the same optical properties.

The ice water content is determined analog, whereby q_{lw} and q_{rw} are replaced by the specific ice water content q_{ice} and specific snow water content q_{sn} , respectively.

5.4.2 Output from libRadtran

Simulated F are provided in individuals files for every two seconds. The standard output-files contain spectrally resolved downward direct irradiance $F_{\text{lib,dir}}^{\downarrow}(\lambda)$ and diffuse irradiance $F_{\text{lib,dif}}^{\downarrow}(\lambda)$ as well as the upward irradiance $F_{\text{lib}}^{\uparrow}(\lambda)$ at flight altitude. The total downward irradiance $F_{\text{lib}}^{\downarrow}(\lambda)$ is obtained by $F_{\text{lib}}^{\downarrow}(\lambda) = F_{\text{lib,dir}}^{\downarrow}(\lambda) + F_{\text{lib,dif}}^{\downarrow}(\lambda)$. The simulations of $F_{\text{lib},\lambda}$ are spectrally interpolated to match the band resolution of ecRad and are denoted with $F_{B_i,\text{lib},x}$, with i the band number and x the applied ice parameterization. Broadband F are indexed with $F_{\text{BB},\text{lib},x}$.

5.5 Comparison of Modeled Albedo Sensitivity on Trade Wind Cumulus

Clouds with low optical thickness ($\tau < 10$) and $LWP < 100 \text{ g m}^{-2}$ show an increased susceptibility in radiative forcing on changes of LWP and N , and are difficult to parameterize in NWP and GCM (Sato et al., 2015; Vial et al., 2017). To quantify the capability of ecRad to simulate the Twomey effect of trade wind cumuli, calculations with combinations of LWP and N are performed and compared with libRadtran benchmark simulations based on simulations with 16-streams in the RTS. The solar cloud top albedo α is calculated for a homogeneous liquid water cloud located between 1000 and 1500 m and a solar zenith angle of 5°. LWP is varied in a range between 10 and 200 g m^{-2} , typical for shallow trade wind cumulus (Siebert et al., 2013). The cloud albedo sensitivity ζ is defined as:

$$\zeta(LWP, r_{\text{eff}}, N) = \frac{d\alpha(LWP, r_{\text{eff}}, N)}{dN}, \quad (5.5)$$

which represents the change of α with respect to an increase of N , given in units of cm^3 . ζ from libRadtran is indexed with 'lib' while results from ecRad are indexed with 'eR'. Figure 5.2a shows simulated α_{lib} as a function of N and LWP . For constant LWP and increasing N (decreasing r_{eff}), α_{lib} increases, which is described by the Twomey effect. For constant N and increasing LWP (increasing r_{eff}), α increases with different rates for N . This illustrates that different cloud regimes exert various sensitivities in terms of the Twomey effect. Therefore, LWP , N , and r_{eff} have to be considered carefully to parameterize the radiative properties of trade wind cumuli precisely. For simulated α_{eR} by ecRad (Fig. 5.2b) the resulting pattern deviates from α_{lib} with a broaden region for α_{eR} between 0.4 and 0.6, indicating for a larger fraction of moderate reflective clouds. Simultaneous, the broadening of the region reduces the number of cloud combinations with α_{eR} below 0.4 and above 0.6. The maximum α_{eR} is lower compared to α_{lib} .

Figure 5.2c displays ζ_{lib} as a function of N for different LWP . In general, ζ decreases with increasing N . For libRadtran, clouds with low LWP (black) and low N have a lower ζ compared to clouds with higher LWP (red) but same N . The lowest ζ_{lib} is obtained for clouds with the highest LWP of 200 g m^{-2} , while thinner clouds with the lowest LWP of 10 g m^{-2} have the lowest ζ . Because of $r_{\text{vol}} \propto \sqrt[3]{LWP/N}$ the change of N for constant LWP is higher for large LWP , e.g., 200 g m^{-2} , compared to lower values of LWP of 10 g m^{-2} and resulting absolute differences in simulated α_{lib} and ζ_{lib} . Due to low τ and LWP or LWC , the calculated α_{lib} and ζ_{lib} are easily affected by variations in r_{eff} resulting from the dependence of α_{lib} on the phase function (describing the angular dependence of the scattering of a liquid water droplet or ice crystal), which changes with r_{eff} , and applying 16 streams in the RTS. In Fig. 5.2d ζ_{eR} shows a similar slope compared to ζ_{lib} but with almost no difference in ζ_{eR} for different LWP , except for $LWP = 10 \text{ g m}^{-2}$. This indicates that ζ_{eR} is equal for all LWP and the Twomey effect is likely to be overestimated for low LWP and underestimated for larger LWP , explaining the widen fraction of α_{eR} in Fig. 5.2b.

In Fig. 5.2e ζ_{lib} is shown as a function of r_{eff} for clouds of different LWP . With cloud geometric thickness H and assuming a constant LWP , the effective radius determines N or vice versa following:

$$r_{\text{eff}} = \sqrt[3]{\frac{3 \cdot LWP}{4 \cdot \rho_w \cdot \pi \cdot H \cdot N}} \cdot k^{-3}. \quad (5.6)$$

For all LWP cases the sensitivity increases with increasing r_{eff} (decreasing N). This agrees with Fig. 5.2c, where low N have the highest ζ . Clouds with lower LWP show higher ζ_{lib} and, therefore, are more sensitive to changes of r_{eff} compared to clouds with higher LWP . The response of ζ on r_{eff} is present in both models, with slightly higher values and a steeper slope of ζ_{lib} for $LWP > 50 \text{ g m}^{-2}$. For Lower LWP , ζ_{eR} is higher compared to ζ_{lib} .

In Fig. 5.2g ζ is displayed as a function of τ . For all clouds with different values of LWP , ζ decreases with increasing τ . This implies that changes in N have larger effects on α for clouds with low τ . As a result, optically thin clouds with low N and large r_{eff} , which is the typical character of shallow trade wind cumulus, are subject to the strongest Twomey effect. For ecRad (Fig. 5.2h) the same pattern appears, with an overestimation ζ_{eR} for LWP below 50 g m^{-2} supporting the pattern of Fig. 5.2b.

The comparison indicates that ecRad treats a larger fraction of clouds with combinations of N and LWP equally, leading to a reduced grading of different cloud regimes and generally lower α_{eR} . While for clouds with $50 < LWP < 100 \text{ g m}^{-2}$ ζ_{eR} agrees with libRadtran, ζ_{eR} is overestimated for clouds with lower $LWP < 50 \text{ g m}^{-2}$ and underestimated for trade wind cumulus with $LWP > 100 \text{ g m}^{-2}$.

libRadtran simulations have been repeated with a two-stream solver. Only minor differences in F^\uparrow , α , and ζ with relative deviations below 1 % are detected between the libRadtran two-stream and 16-stream simulations. Therefore, differences between libRadtran and ecRad are not caused by using lower streams for the RTS. The deviations are addressed to the correlation of LWP with the cloud optical properties. The presented results are only valid for the simulated clouds and considered solar zenith angle.

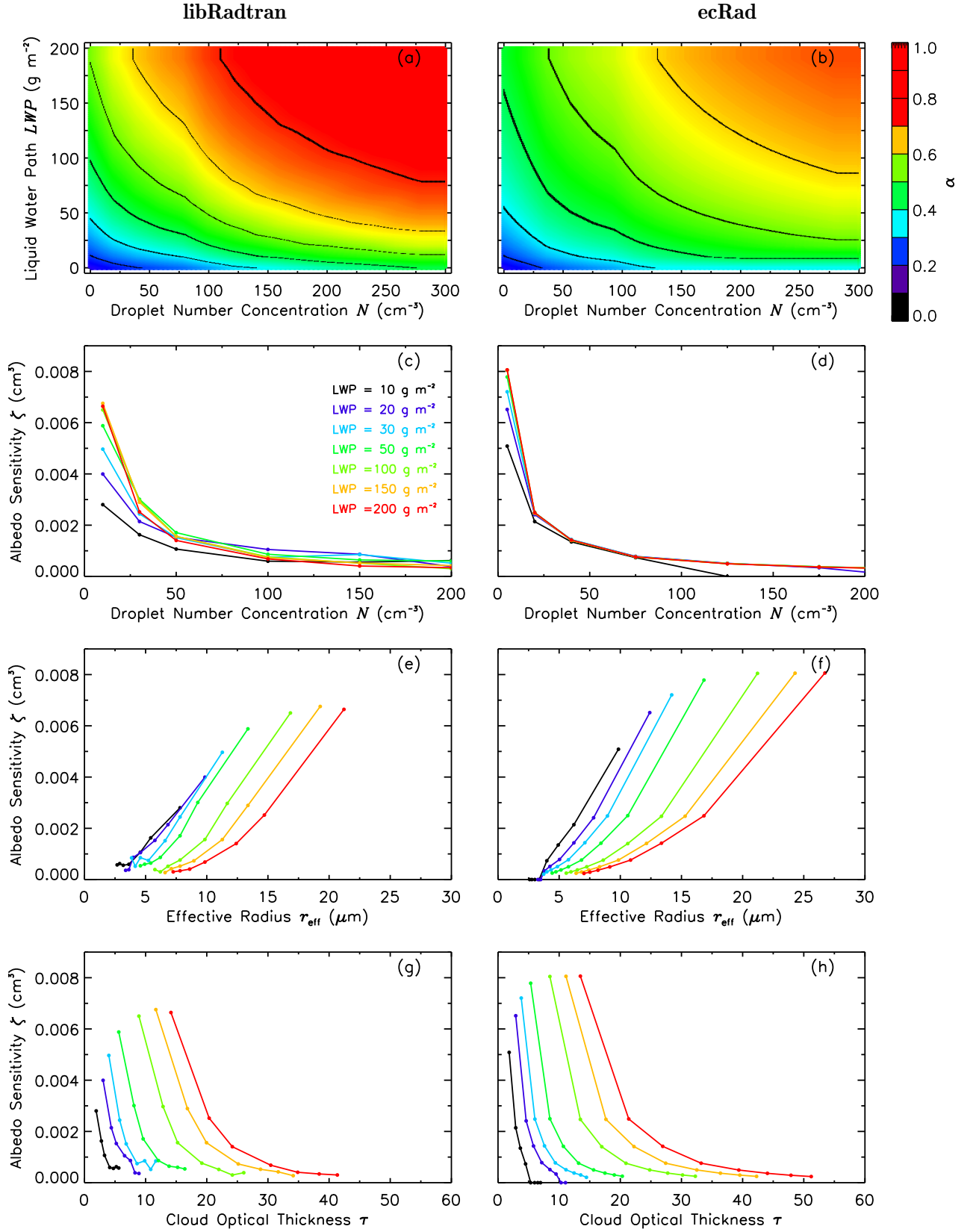


Figure 5.2: Simulations by libRadtran (left) and ecRad (right) for a liquid water cloud between 1000 and 1500 m with liquid water path LWP from 10 to 200 g m^{-2} and for a solar zenith angle θ_0 of 5° . The simulations are integrated over a wavelength range from 500 to 550 nm. Panels a) and b) show cloud top albedo α for combinations of the cloud droplet number concentration N and LWP . Panels c) and d) show cloud top albedo sensitivity ζ as a function of N for different LWP . Panels e) and f) display ζ as a function of effective radius r_{eff} and in panels g) and h) as a function of cloud optical thickness τ for both models.

5.6 Model Caveats

5.6.1 Representativeness of the Observations

During NARVAL-II and NAWDEX, HALO was operated for 200 hours, covering a period of two month with two season (late summer and autumn), two regions of the Earth (mid-latitudes and sub-tropics), and two different cloud regimes (trade wind cumuli and stratiform clouds). Despite that, airborne observations only provide a limited perspective in space and time, which inevitably limits the representativeness of the measurements with regard to other areas of the Earth or seasons of the year. Therefore, the representation of the along-track simulations with respect to the covered area is restricted.

For illustration of the limited observed area, NAWDEX RF04 from the 26 September 2016 is selected. A rectangular outline, defined by the maximum dimensions of the HALO flight pattern, encloses an area of 2831400 km². By considering a total flight time of nine hours, an average flight speed of $v_{ac} = 220 \text{ m s}^{-1}$, and a SMART FOV of 80 km² (90 % of the F^\uparrow signal), the captured area is around 570240 km², which is roughly 20 % of the total area and, thereby, represents only a minor fraction of the radiation field. In addition, during the performed RFs distinctive weather systems were targeted, which further limits the general representation of individual RFs. Conversely, the selection of specific areas allows for systematic investigation, e.g., the evolution of clouds and according radiative effects. As a result, studies based on airborne measurements are always a trade-off between the general representation and cloud-process resolved investigation. Therefore, the observations by SMART have to be understood as stochastically sampling (flight track) from a total population (entire field), requiring for statistical analysis.

5.6.2 Deviations between Modeled and Observed Irradiance

Besides errors in the cloud optical parameterizations additional discrepancies in F^\uparrow are caused by the utilized IPA model set-up, where lateral photon transport and the influence of neighboring model columns on F^\uparrow is neglected. Therefore, further calculations are performed, which include model columns around the aircraft nadir column. Despite that, horizontal photon transport between individual columns is not considered in this multi-column approach. Due to the increased number of simulated columns the comparison of the IPA and non-IPA approach is performed for ecRad only.

The required size of the simulated area around the nadir column is determined by the maximum flight altitude of HALO with 12 km and the FOV of SMART. Considering that 90 % of total F^\uparrow reaches the sensor from opening angles smaller than 71°, the according instruments footprint is 70 km in diameter (see Eq. (3.1)). This area must be entirely covered by the simulations and is selected to be $11 \cdot 0.1^\circ \times 11 \cdot 0.1^\circ$ ($\approx 99 \times 99 \text{ km}$) in size. For every time step the resulting field of F_{eR}^\uparrow is weighted with the cosine response function of the F^\uparrow inlet of SMART to mimic the optical characteristics of the sensor. The results of the simulated fields are refereed as n-IPA in the following.

Figure 5.3a shows resulting time series of broadband $F_{BB,eR}^\uparrow$ using IPA (blue), $F_{BB,eR,n-IPA}^\uparrow$ from the entire field (orange), and the SMART observations $F_{BB,mea}^\uparrow$ (black + gray). In Fig. 5.3b the total cloud cover $f_{tot,mea}$ from SMART and in Fig. 5.3c the relative deviation of $F_{BB,eR,IPA}^\uparrow$ and $F_{BB,eR,n-IPA}^\uparrow$ with respect to $F_{BB,mea}^\uparrow$ are displayed.

By considering the surrounding field, the variance of the time series of $F_{BB,eR,n-IPA}^\uparrow$ is slightly reduced due to an averaging over a larger domain and smoothing extreme values of individual nadir columns. The time series of $F_{BB,eR,IPA}^\uparrow$ and $F_{BB,eR,n-IPA}^\uparrow$ are almost identical. Related relative differences between the two simulation approaches are below 3 %. This shows that the IPA simulations sufficiently represent a larger domain under the given observation constrains of stratiform clouds. The homogeneity of the section is confirmed by average $f_{tot,mea}$ above 75 % (Fig. 5.3b). Despite that, larger relative differences among the IPA and non-IPA appear for increasing cloud field heterogeneity, e.g., in the sub-tropics for trade wind cumuli.

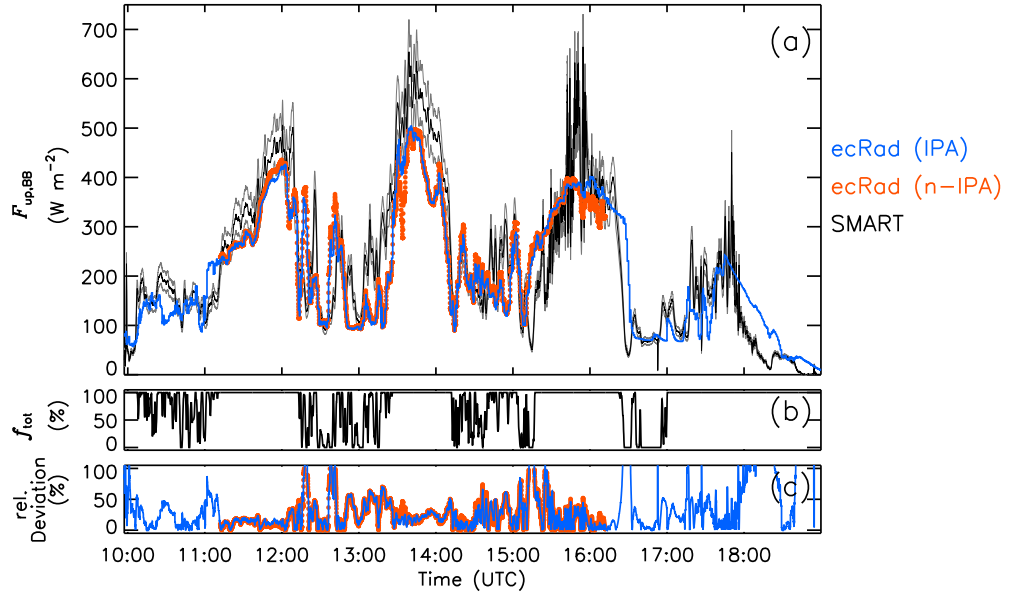


Figure 5.3: Panel a) shows time series of upward broadband irradiance F_{BB}^{\uparrow} of NAWDEX flight 26 September 2016 from the independent pixel simulations with ecRad (blue), the ecRad simulated radiation field of F_{BB}^{\uparrow} (orange), and the SMART observations and uncertainties (black + gray). In panel b) observed total cloud cover f_{tot} from SMART and in panel c) the relative deviations between observed F_{BB}^{\uparrow} and the simulations as well as $F_{\text{BB,eR,IPA}}^{\uparrow}$ (blue) and $F_{\text{BB,eR,n-IPA}}^{\uparrow}$ (orange) are shown.

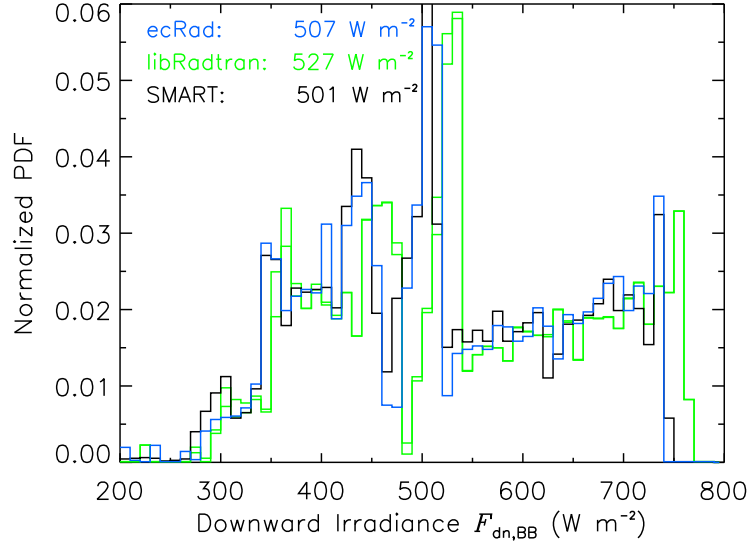


Figure 5.4: Probability density function of downward broadband irradiance $F_{\text{BB}}^{\downarrow}$ of ecRad (blue), libRadtran (green), and SMART (black) of research flight (RF04) conducted on 26 September 2016 during NAWDEX.

5.7 Comparison of Along-Track Measured and Simulated Irradiance

In this chapter a detailed analysis of measured and simulated irradiance F from NARVAL-II RF06 and NAWDEX RF04 is presented. Comparing downward F^{\downarrow} from ecRad, libRadtran, and the measurements the model set-up and the appropriate representation of F^{\downarrow} at TOA are verified. Afterwards, spectral and broadband F^{\uparrow} and α of both flights are investigated.

5.7.1 Downward Irradiance

To test the general performance of the radiative transfer models without significant impact of clouds the downward irradiance in flight level is simulated and compared to the observation. Above HALO, cloud free conditions prevailed during both flights. Figure 5.4 shows the normalized probability density function (PDF) of downward solar irradiance simulated by ecRad $F_{\text{BB,eR}}^{\downarrow}$ (blue), libRadtran $F_{\text{BB,lib,Ba}}^{\downarrow}$ (green), and measured by SMART $F_{\text{BB,mea}}^{\downarrow}$ (black). The width of the distributions is determined by changes of the solar zenith angle θ_0 along the flight track of HALO. The PDFs of $F_{\text{BB}}^{\downarrow}$ agree with respect to the features of the distribution, indicating that $F_{\text{BB}}^{\downarrow}$ is simulated and measured consistent. The mean values of the different models slightly differ, with the libRadtran PDF being shifted to higher values by 20 W m^{-2} , exhibiting a systematic offset whereby PDFs of ecRad and SMART match with each other. The systematic bias of $F_{\text{BB,lib}}^{\downarrow}$ results from slightly deviating atmospheric profiles of temperature T , pressure p , and humidity q above 20 km height. The offset of 20 W m^{-2} is within the model and measurement uncertainty of $\pm 5\%$ and regarded to be negligible with respect to the strong radiative effects of clouds.

Analog, resulting PDFs for NARVAL-II RF06 are shown in Fig. 5.5. For SMART a median of 1077 W m^{-2} is measured while the median for ecRad is 1075 W m^{-2} and for libRadtran is 1097 W m^{-2} . Simulated $F_{\text{BB,eR}}^{\downarrow}$ and $F_{\text{BB,lib}}^{\downarrow}$ agree with observed $F_{\text{BB,mea}}^{\downarrow}$ within the SMART measurement uncertainty.

5.7.2 Upward Irradiances of Stratiform Cloud Fields

The upward F^{\uparrow} is predominantly determined by the general presence of clouds quantified by the total cloud cover. In the simulations the horizontal distribution of clouds in partly cloud covered grid-boxes

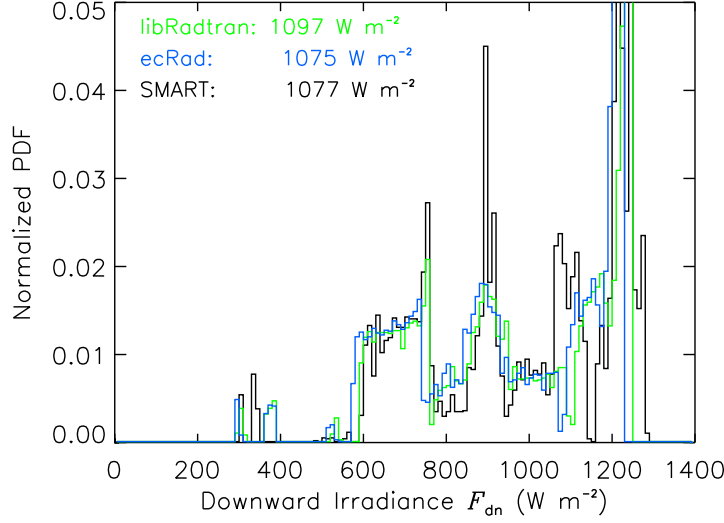


Figure 5.5: Probability density function of downward broadband irradiance $F_{\text{BB}}^{\downarrow}$ of ecRad (blue), libRadtran (green), and SMART (black) of research flight 06 (RF06) conducted on 19 August 2016 during NARVAL-II.

is specified by the cloud overlap assumption (COA). To evaluate the applied 'EXP-RAN' COA in the simulations the derived $f_{\text{tot,eR}}$ is compared with observations by SMART.

Figure 5.6 shows the normalized PDF of $f_{\text{tot,eR}}$ diagnosed from the ecRad solver (blue), applying the 'EXP-RAN' COA, and SMART derived $f_{\text{tot,mea}}$ (black) for the entire RF04. The PDF of $f_{\text{tot,mea}}$ is homogeneously distributed for all values of $f_{\text{tot,mea}}$ while the distribution of $f_{\text{tot,eR}}$ is skewed to the right, indicating a systematically higher frequency of larger $f_{\text{tot,eR}}$. The median total cloud cover of the simulations and the observations amount to $f_{\text{tot,eR}} = 79.7\%$ and $f_{\text{tot,mea}} = 76.6\%$, implying that the location and distribution of the modeled cloud field was very close to reality. From the remaining difference of 4% it is concluded that the applied COA 'EXP-RAN' in ecRad causes only a slight overestimation for the stratiform cloud conditions during RF04.

Figure 5.7 shows a centered time series of RF04 between 10:00 and 19:00 UTC to illustrate differences of the liquid water and ice cloud sections. During the selected time HALO crossed the warm conveyor belt (WCB) of a low-pressure system from south-east to north-west, flew over an area with heterogeneous stratus patches, and then crossed the WCB further north in the opposite direction. After following the low-pressure system, the WCB was crossed twice again. Three sections of RF04 are selected for more detailed analysis and are marked by the gray boxes. For RF06 a MODIS satellite overpass is available captured around 12:50 UTC when HALO was close to the center of the satellite covered area. The MODIS data is used to compare the CTP and cloud top effective radius r_{eff} with the SMART observations and the IFS AD.

At the top of Fig. 5.7 the covered distance is provided in kilometers. In Fig. 5.7a the CTP indicates ice (blue) and liquid water (red). The first line shows CTP from SMART, the second line from the MODIS satellite overpass, and the third line the CTP ratio $\chi_{\text{p,eR}}$ from ecRad. Subsequently, Fig. 5.7b shows broadband solar F_{BB}^{\uparrow} from SMART $F_{\text{BB,mea}}^{\uparrow}$ (black + gray uncertainties), ecRad simulations using the Fu parameterization $F_{\text{BB,eR,Fu}}^{\uparrow}$ (blue), libRadtran Fu results $F_{\text{BB,lib,Fu}}^{\uparrow}$ (orange), and libRadtran $F_{\text{BB,lib,Ba}}^{\uparrow}$ (green) using the Baum ice parameterization. Figure 5.7c and Fig. 5.7d show spectral F_{B6}^{\uparrow} (1298 - 1626 nm) and F_{B9}^{\uparrow} (625 - 778 nm), respectively. MODIS retrieved $r_{\text{eff,mod}}$ as well as calculated r_{eff} are plotted in Fig. 5.7e. Vertical profiles of LWC and IWC from the IFS AD are displayed in Fig. 5.7f and Fig. 5.7g, respectively. Radar reflectivity Z_{mea} measured by HAMP is plotted in Fig. 5.7h. The red line indicates the CTH determined from the ecRad simulations. Below, Fig. 5.7i presents vertical profiles of the IFS cloud cover.

For the first crossing of the WCB (10:45 - 14:45 UTC) simulated and observed F_{BB}^{\uparrow} and F_{B9}^{\uparrow} agree

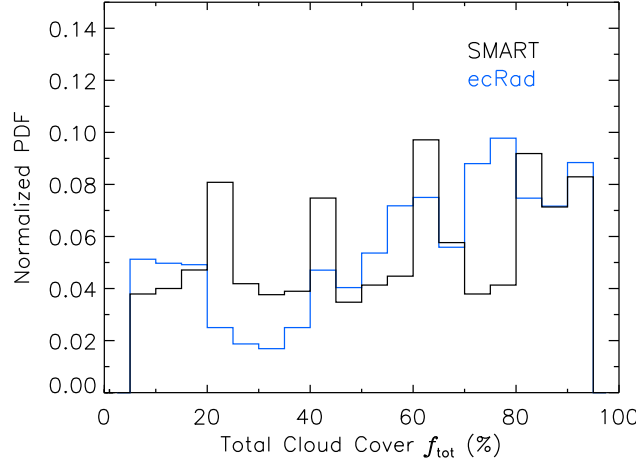


Figure 5.6: Normalized probability density function (PDF) of the total cloud cover f_{tot} diagnosed by ecRad (blue) and derived from the SMART observations (black).

within the SMART measurement uncertainty of $\pm 5\%$. For F_{B6}^{\uparrow} a significant underestimation appears by $F_{\text{BB,eR,Fu}}^{\uparrow}$ and is followed by $F_{\text{BB,lib,Fu}}^{\uparrow}$. Both sections are characterized by clouds with dominant presence of ice at cloud top. Good agreement is present for $F_{\text{BB,lib,Ba}}^{\uparrow}$ ranging within the SMART uncertainty. The same spectral features are observed for the second crossing of the WCB (13:40 - 14:25 UTC) and the remaining ice topped parts of RF04. The appearance of the deviation in the ice sections is an indicator for deficiencies in the ice cloud representation by ecRad and the libRadtran Fu ice optics parameterization, which requires a more detailed investigation.

In addition to misrepresented clouds in the IFS AD, further model shortcomings contribute to the observed deviations between SMART and the model simulations. Due to the nature of the definition of F , SMART receives radiation from an area, which is larger than a single grid-box size (IPA simulations). Flying above heterogeneous cloud scenes $F_{\text{BB,mea}}^{\uparrow}$ can be positively biased due to 3D scattering effects, contradicting the IPA used in the simulations. These effects are not simulated by the radiative transfer solver ecRad, which bases on plane-parallel model layers. The potential 3D scattering characteristics mostly affect radiation for wavelength below 1400 nm (Marshak et al., 1995), which is the part of the solar spectrum containing the majority of total $F_{\text{TOA}}^{\downarrow}$ (Liou, 2002) and, therefore, contribute to deviations in $F_{\text{BB,mea}}^{\uparrow}$ significantly.

A second factor for differences in F is the number of applied streams in the RTS. In the presented ecRad set-up two-stream calculations are applied and the scattering phase function of non-spherical particles is treated by the Delta-Eddington-Approximation (Joseph et al., 1976). In both libRadtran benchmark runs 16-stream calculations are used better considering the forward peak for cloud droplets and sideward scattering in case of ice crystals. For reference, the number of streams in libRadtran was reduced to two, whereby no significant differences for F_{BB}^{\uparrow} among the libRadtran two-stream and 16-streams as well as the ecRad simulations are found. Therefore it is concluded, that the deviations between ecRad and libRadtran are not caused by the number of applied streams and the two-stream approximation provides sufficient accuracy for the given observation conditions of RF04.

Figure 5.8 shows PDFs of upward broadband simulated and measured irradiance from ecRad Fu $F_{\text{BB,eR}}^{\uparrow}$ (blue), libRadtran Fu $F_{\text{BB,lib,Fu}}^{\uparrow}$ (orange), libRadtran Baum $F_{\text{BB,lib,Ba}}^{\uparrow}$ (green), and SMART observed $F_{\text{BB,mea}}^{\uparrow}$ (black) of the entire RF04. The distribution of $F_{\text{BB,eR,Fu}}^{\uparrow}$ is slightly shifted to lower values with a median of 225 W m^{-2} . Higher values of F_{BB}^{\uparrow} are simulated by libRadtran using the Fu and Baum parameterization, leading to medians of similar value of 227 and 234 W m^{-2} , respectively. The observed $F_{\text{BB,mea}}^{\uparrow}$ are generally higher compared to all simulations with a median of 245 W m^{-2} .

Figure 5.7: Time series of entire flight between 10:00 and 19:00 UTC. The panels of the plot show a) cloud top phase, b) - d) measured and simulated irradiance F , e) cloud top effective radius r_{eff} , f) liquid water content LWC and g) ice water content IWC content, h) radar reflectivity Z , and i) fractional cloud cover f .

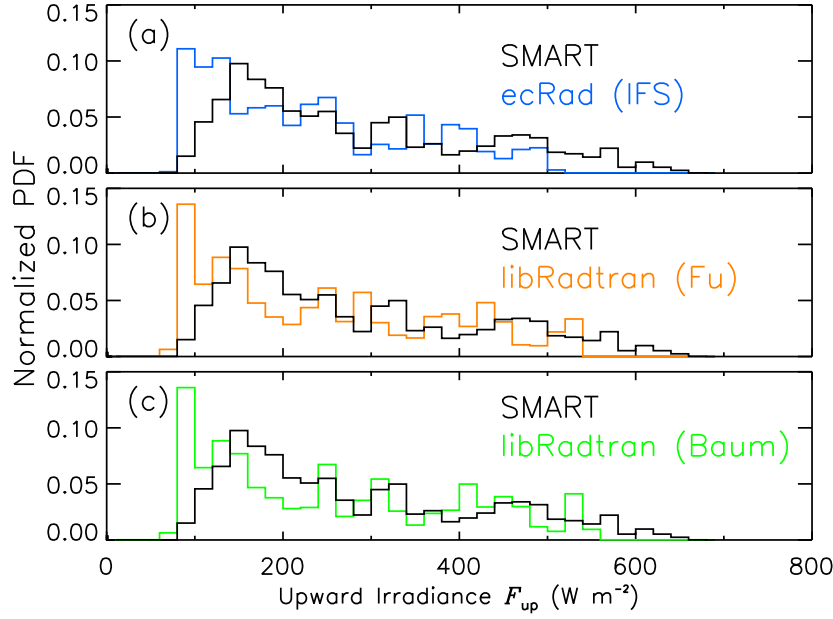


Figure 5.8: Normalized probability density function (PDF) of broadband upward irradiance in the solar wavelength range from SMART, ecRad Fu (a), libRadtran Fu (b), and libRadtran Baum (c) of the entire research flight 26 September 2016.

The relative deviation between $F_{\text{BB,eR}}^{\uparrow}$ and $F_{\text{BB,mea}}^{\uparrow}$ exceeds the SMART uncertainty range (lower F^{\uparrow} are overestimated, high F^{\uparrow} underestimated) and indicates that the model does not represent the upward directed radiation correctly. The higher amount of low F^{\uparrow} derived from the IFS AD reflects the higher frequency of occurrence of grid boxes with low cloud fractions (compare Fig. 5.6). However, the median values of $f_{\text{tot,eR}}$ indicate a higher fraction of clouds in the IFS AD while the median $F_{\text{BB,eR}}^{\uparrow}$ is lower compared to the observations. This indicates that either cloud properties such as total water path TWP and cloud phase differ from the observations, or the radiative transfer models.

The resulting median values of F_{BB}^{\uparrow} from SMART and the models of the entire flight are listed in Tab. 5.4. Relative differences are calculated with respect to the libRadtran Baum reference simulation and are given in brackets. For the full flight $F_{\text{BB,lib,Fu}}^{\uparrow}$ and $F_{\text{BB,lib,Ba}}^{\uparrow}$ are slightly deviating (-2.6%). This differences result only from ice topped clouds, as F^{\uparrow} of liquid water cloud sections are simulated identically due to the exactly same libRadtran setup.

The selection for liquid water and ice at cloud top reveals that the underestimation in $F_{\text{BB,eR}}^{\uparrow}$ (-

Table 5.4: Median values of solar upward irradiances F^{\uparrow} of the entire RF04 conducted on 26 September 2016 separated for ice and liquid water sections. Relative deviations refer to the libRadtran Baum benchmark simulation.

	ecRad	libRadtran		SMART
	Fu	Fu	Baum	
	$F_{\text{BB,eR,Fu}}^{\uparrow} (\text{W m}^{-2})$	$F_{\text{BB,lib,Fu}}^{\uparrow} (\text{W m}^{-2})$	$F_{\text{BB,lib,Ba}}^{\uparrow} (\text{W m}^{-2})$	$F_{\text{BB,obs}}^{\uparrow} (\text{W m}^{-2})$
all	225.2 (-3.7 %)	227.7 (-2.6 %)	233.8	244.9 (4.7 %)
ice	332.4 (-8.9 %)	351.3 (-3.8 %)	365.2	375.3 (2.8 %)
liquid water	141.4 (+2.7 %)	137.7 (0 %)	137.7	186.2 (32.8 %)

Table 5.5: Microphysical and macrophysical properties, solar zenith angle (SZA), and flight parameters of the selected cloud cases.

	Cloud Case #1	Cloud Case #2	Cloud Case #3
LWP (kg m^{-2})	0.422 0.500	0.341 0.133	0.051 0.041
IWP (kg m^{-2})	2.412 2.534	2.408 2.021	0.004 0.003
r_{eff} (μm)	29.3	32.1	21.3
CTH (km)	9.9	10.9	2.6
SZA ($^{\circ}$)	65.2	59.3	63.7
Flight Altitude (km)	12.4	12.5	12.0

3.7 %) is caused by regions with ice-topped clouds with relative differences of -8.9 % for 'Fu', indicating potential discrepancies in the ice optics parameterizations of ecRad. For the liquid water sections a relative good agreement among the models with +3 % is found, whereby observed $F_{\text{mea}}^{\uparrow}$ is significantly higher by +33 %.

The aforementioned cloud cases from RF04 are selected (gray boxes in Fig. 5.7) and analyzed in detail with respect to their spectral representation in the models to disentangle the spectral differences in simulated and observed F^{\uparrow} and α of liquid water and ice clouds. An overview of the microphysical and macrophysical properties, the solar zenith angle (SZA), and the flight parameters of these cloud cases is given in Tab. 5.5.

Ice Cloud Case #1

Cloud case CC#1 contains 750 simulated time-steps and 3000 individual SMART measurements. Time series of F_{BB}^{\uparrow} in Fig. 5.7b and the radar image in Fig. 5.7h as well as slight fluctuations in $F_{\text{BB,mea}}^{\uparrow}$ reveal a homogeneous cloud structure. Measured $F_{\text{BB,mea}}^{\uparrow}$ increases with time from 350 W m^{-2} to a maximum of 500 W m^{-2} around 12:01 UTC decreasing afterwards due to a fading cloud structure. All simulated F_{BB}^{\uparrow} follow the observations with $F_{\text{BB,lib,Fu}}^{\uparrow}$ and $F_{\text{BB,lib,Ba}}^{\uparrow}$ almost matching with $F_{\text{BB,mea}}^{\uparrow}$.

CTP from SMART, MODIS, and the IFS AD indicate the presence of ice at any time, which is supported by the absence of LWC at higher altitudes (Fig. 5.7f) and only minor concentrations of LWC below. In Fig. 5.7g the IWC is displayed with grid-box maxima up to 0.2 g m^{-3} . The locations of maximum IWC agree with sections of maximum measured Z_{mea} . However, a direct quantitative comparison of IWC and Z_{mea} is not possible but qualitatively the vertical cloud representation in the IFS AD is confirmed by HAMP.

Spectral cloud top albedo α_{λ} (defined as $F_{\lambda}^{\uparrow} / F_{\lambda}^{\downarrow}$) is a measure for the radiative impact of a cloud. Figure 5.9a - i show PDFs of α_{λ} calculated from SMART measurements (black), ecRad Fu simulations (blue), and libRadtran simulations using the Fu (orange) and Baum (green) parameterization. The first column shows broadband α_{BB} and subsequent columns present α for spectral band B9 (dominated by scattering) and band B6 (dominated by absorption). In Tab. 5.6 the mean and median values of simulated and observed F^{\uparrow} and α for CC#1 are listed.

Broadband $\alpha_{\text{BB,mea}}$ from SMART is generally higher, which is indicated by the peak of the PDF around 0.83. Simulated $\alpha_{\text{BB,eR,Fu}}$ shows a similar slope but is shifted to lower values by 0.09 with a peak around 0.74, analog to the PDF of libRadtran Fu $\alpha_{\text{BB,lib,Fu}}$. $\alpha_{\text{BB,lib,Ba}}$ is shifted to lower values by 0.07 compared to $\alpha_{\text{BB,mea}}$ with a peak at 0.79.

In the second column, α_{B9} for spectral band B9 is shown. $\alpha_{\text{B9,mea}}$ shows highest values with a peak at 0.91 while all models have lower median values of $\alpha_{\text{B9,eR,Fu}} = 0.85$, $\alpha_{\text{B9,lib,Fu}} = 0.87$, and $\alpha_{\text{B9,lib,Ba}} = 0.89$. The shapes of $\alpha_{\text{B9,eR,Fu}}$ and $\alpha_{\text{B9,lib,Fu}}$ appear to be nearly identical, similar to α_{BB} , whereby $\alpha_{\text{B9,lib,Ba}}$ shows slightly higher values compared to $\alpha_{\text{B9,eR,Fu}}$ (+0.04) and $\alpha_{\text{B9,lib,Fu}}$ (+0.01).

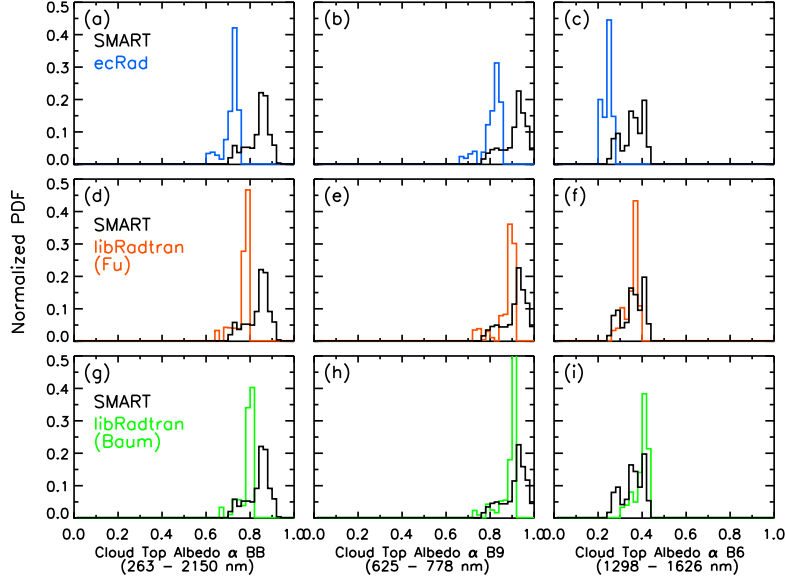


Figure 5.9: Probability density functions (PDF) of broadband and spectral cloud top albedo α from ecRad Fu, libRadtran Fu, libRadtran Baum model set-ups, and SMART observations of CC#1.

In contrast to α_{B9} , significant differences appear for α_{B6} from the ecRad simulations. $\alpha_{B6,ecR,Fu}$ peaks at 0.25 and is lower by 0.11 compared to $\alpha_{B6,mea}$, which has its maximum around 0.36. Calculated $\alpha_{B6,lib,Fu}$ is shifted to lower values by 0.05 compared to $\alpha_{B6,obs}$ and $\alpha_{B6,lib,Ba}$ is matching the observations of $\alpha_{B6,mea}$.

To exploit the full spectral capability of SMART the spectral analysis of CC#1 is extended for all ecRad spectral bands in the solar wavelength range, allowing to separate for the impact of LWC and IWC , and the particle effective size r_{eff} on the cloud top albedo. While the LWC and IWC predominantly determine scattering wavelengths (e.g. 645 and 858 nm), r_{eff} determines the spectrum of absorbing wavelengths (e.g. 1640 and 2200 nm). To demonstrate this capability, measurements from the homogeneous part of CC#1 are selected and averaged in time, assuming that the SZA is constant within the ten-minute period. Figure 5.10a shows the averaged spectra of F^\uparrow from ecRad (blue), libRadtran Fu (red) and Baum (green), and SMART (black) interpolated on the ecRad spectral resolution.

Table 5.6: Mean and median values of microphysical / macrophysical properties, upward irradiances F^\uparrow , solar zenith angle (SZA), and flight parameters of ice cloud #1.

	SMART	ecRad	libRadtran	
			Fu	Baum
F_{BB}^\uparrow (W m^{-2})	428 435	391 407	413 428	425 435
F_{B9}^\uparrow (W m^{-2})	80 81	75 78	76 81	77 82
F_{B6}^\uparrow (W m^{-2})	16 16	11 11	14 15	16 17
α_{BB}	0.84 0.85	0.75 0.77	0.79 0.79	0.79 0.81
α_{B9}	0.91 0.92	0.85 0.87	0.87 0.90	0.89 0.91
α_{B6}	0.36 0.36	0.24 0.25	0.35 0.36	0.40 0.40

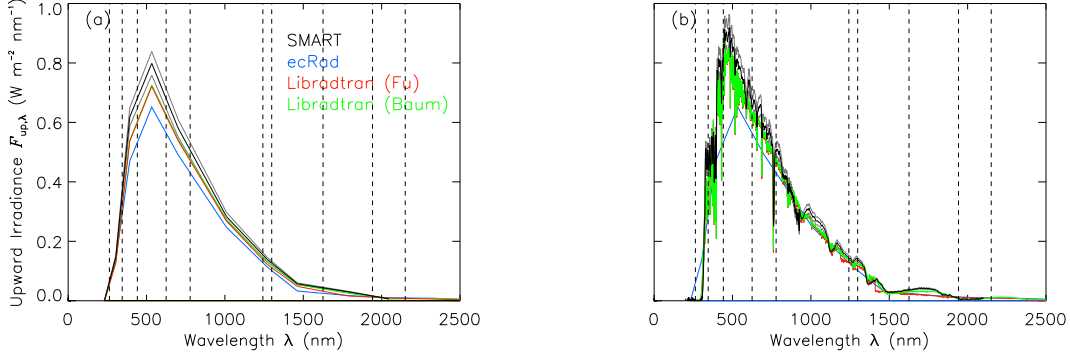


Figure 5.10: Exemplary spectra at 11:54 UTC from CC#1 averaged over five consecutive samples. Colored lines show spectra from SMART (black), ecRad (blue), libRadtran Fu (red), and libRadtran Baum (green) on basis of the ecRad band resolution.

All three simulations of $F_{\text{mea}}^{\uparrow}$ are lower compared to SMART and are outside of the indicated SMART uncertainty range (gray). The lowest values are reported for F_{eR}^{\uparrow} . Simulated $F_{\text{lib}}^{\uparrow}$ from the libRadtran Fu and Baum parameterization are matching among each other, except for wavelength larger than 1000 nm with lower values for F_{Fu}^{\uparrow} . Due to the selection of a homogeneous cloud and a total cloud cover close to 100 %, an influence by f_{tot} is excluded and the systematic underestimation of F^{\uparrow} by all models is related to a lack of IWC in the IFS AD.

Figure 5.10b shows the same spectra with their native spectral resolution of SMART and libRadtran (1-10 nm). The highest values appear for $F_{\text{mea}}^{\uparrow}$, being followed by the Baum and Fu parameterization. The libRadtran Baum benchmark simulation shows larger relative differences for wavelength below 1000 nm, further indicating for too low concentrations of IWC at CT. Simultaneously, the missing IWC in the IFS AD, leads to smaller parameterized $r_{\text{eff,eR}}$ in the model (see 5.7e), which increases F^{\uparrow} and partly counterbalances the lack of IWC . The compensating effect is larger for wavelength above 1000 nm, hence, leading to the lower relative differences in F^{\uparrow} between the observation and the models for the VIS wavelength range.

Besides missing IWC in the IFS AD, deviations among the model simulations are caused by the ice optics parameterization and RTS. For CC#1 the deviations between $F_{\text{lib,Ba}}^{\uparrow}$ and $F_{\text{lib,Fu}}^{\uparrow}$ are below 5 % with respect to the entire solar wavelength range. For wavelength below 900 nm the calculated $F_{\text{lib}}^{\uparrow}$ by Baum and Fu are matching with the observations and the deviations are below 3 %. These differences increase towards larger wavelength and are largest for $\lambda > 1200$ nm with $F_{\lambda,\text{Fu}}^{\uparrow}$ underestimating $F_{\lambda,\text{Ba}}^{\uparrow}$ by up to 40 %. This is addressed to the smoothed $\tilde{\omega}$ in the Fu parameterization, where the ice and liquid water absorption features of $\tilde{\omega}$ are neglected (see Fig. 2.4). In spite of the minor relative error (< 5 %) in simulated F^{\uparrow} resulting from the Fu parameterization, absorption of solar radiation by ice crystals for wavelength above 1200 nm is important as they are responsible for local heating, which is expected to alter cloud evolution (Madonna et al., 2014) and provokes a feed back into the cloud optical properties of scattering and absorption also for wavelength in the VIS wavelength range.

The analysis of the spectral F^{\uparrow} of ice clouds from CC#1 is repeated for α to omit the effect of potential biases in F^{\downarrow} . Figure 5.11 shows absolute differences between simulated and observed α for CC#1. Median values of α_{eR} and median differences between libRadtran Fu and SMART are marked by the blue and red dots, respectively. For reference the median deviation between ecRad and the libRadtran Baum benchmark simulations (green) are included. The direct validation among both models eliminates potential biases due to the IFS AD and differences result from the ice optics parameterization only. Values around the zero-line indicate equal α while values larger than zero indicate for higher α_{eR} compared to α_{mea} or $\alpha_{\text{lib,Ba}}$, and vice versa.

Figure 5.11 shows a systematic underestimation of α_{eR} for all wavelength, except for bands B9 to B11 (344 - 778 nm). On average, the difference in α is smaller than -0.075. For spectral band 8

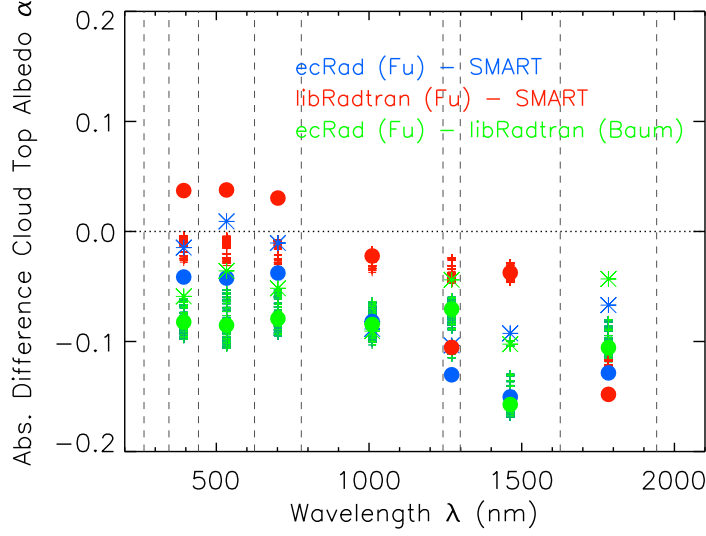


Figure 5.11: Absolute differences of spectral cloud top albedo α between the simulations and SMART observations of CC#1. The red, blue, and green dots represent median values along cloud case CC#1 and colored crosses represent individual α of each individual time point.

ongoing, the deviation increases for longer wavelength, reaching a maximum of up to -0.15 for spectral band 6. The same spectral pattern appears for the absolute difference between libRadtran Fu and SMART. By that, the weakness of the Fu ice optics parameterization in $\tilde{\omega}$ is independently confirmed by the libRadtran Baum simulations and the SMART observations.

To further separate for cloud optical and cloud microphysical properties, α_{B9} is regarded as a proxy for the cloud optical thickness τ and related IWC at cloud top. Individual spectral α are binned for values of α_{B9} between 0.6 and 1.0 with bin sizes of 0.1, are averaged within each τ -bin, and are normalized with respect to α_{B9} . Figure 5.12a - d shows resulting spectral α_λ for the entire CC#1. The vertical lines mark each spectral band of ecRad. The solid black lines represent SMART derived $\alpha_{B9,mea}$ and the blue lines are calculated from ecRad Fu. Additionally, the libRadtran Fu (red) and Baum (green) benchmark parameterizations are included. For all simulated and observed α_λ a decrease with increasing wavelength is present, which is determined by $\tilde{\omega}$. The characteristic spectral slope is declining for lower α_{B9} (analog lower τ , LWC , and IWC) due to reduced IWC , less scattering, and the growing influence of the underlying sea surface. Figure 5.12a shows identical spectral slopes for α_{mea} and $\alpha_{lib,Ba}$. α_{eR} is lowest for wavelength above 1500 nm and slightly higher than $\alpha_{lib,Fu}$. For wavelength below 1500 nm measured and simulated spectral α_λ are matching. In Fig. 5.12b observed α_{mea} is below both libRadtran simulations. For the entire wavelength range simulated α_{eR} is lowest and followed by α_{mea} , $\alpha_{lib,Fu}$, and $\alpha_{lib,Ba}$ in increasing order with the best agreement for the Baum parameterization. Contrarily, in Fig. 5.12c, with α_{B9} between 0.7 and 0.8 the observations mostly confirm simulated α_{eR} and $\alpha_{lib,Fu}$, whereby $\alpha_{lib,Ba}$ is systematically larger. In Fig. 5.12d, with the lowest α_{B9} bin, α_{eR} agree well with the measurements while the libRadtran simulations are systematically higher in the wavelength range between 1000 and 2000 nm.

From CC#1 it is concluded that SMART generally observed higher broadband and spectral α compared to all simulations. The differences in upward F^\uparrow and α between the models and the observations predominantly results from the ice optics parameterization. In general, the best agreement with measured F_{mea}^\uparrow and α_{mea} appears for the libRadtran Baum parameterization, while libRadtran Fu and ecRad Fu suffer from the representation of $\tilde{\omega}$ above 1200 nm wavelength. The scattering and absorption coefficients as well as the asymmetry parameter of the Fu parameterization in ecRad and libRadtran are reviewed and found to be identical. Therefore, the deviations between libRadtran Fu and ecRad Fu are caused by the interpretation of the cloud macrophysical parameters by the RTS and the internal spectral resolution of the simulations. Considering the relative good agreement of

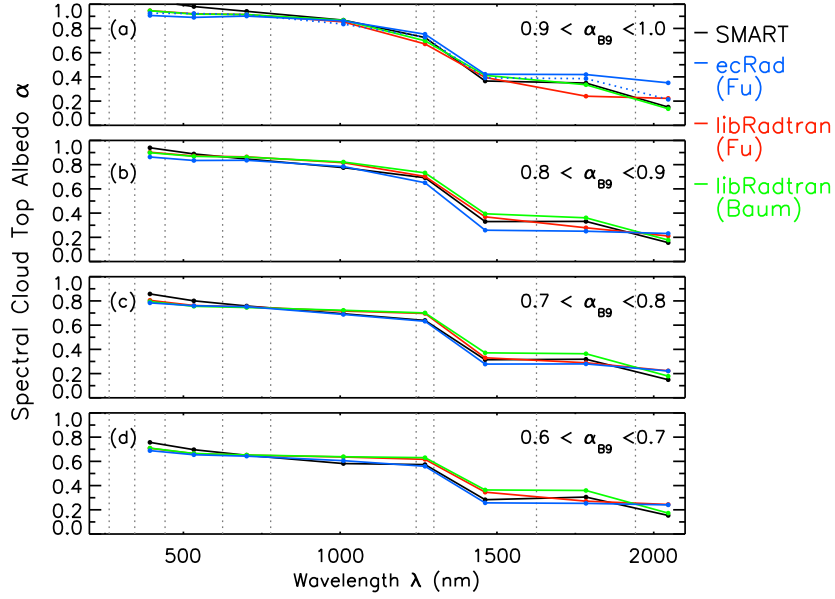


Figure 5.12: Spectral cloud top albedo α of SMART (black), ecRad Fu (blue), libRadtran Fu (orange), and libRadtran Baum (green) binned for α_{B9} . Each point of the functions represents a discrete band average, connected for better legibility.

spectral $\alpha_{BB,lib,Ba}$ with $\alpha_{BB,mea}$, it is further concluded that the cloud top is sufficiently represented in the IFS AD, causing negligible errors compared to the effect of $\tilde{\omega}$.

Ice Cloud Case #2

The second ice cloud case was observed between 13:36 and 13:58 UTC and includes 660 simulated model columns. During this time the WCB was crossed further north-east in the opposite direction of CC#1. The CTP derived from SMART, MODIS, and ecRad indicate ice for the entire section.

Fluctuation in the time series of F_{BB}^{\uparrow} and the radar image (Fig. 5.7h) indicate that CC#2 is more heterogeneous compared to CC#1 with a higher variability in the cloud microphysical and macrophysical parameters. MODIS observed $r_{eff,mod}$ shows fluctuations at 13:46 UTC with a peak of $55 \mu m$ not being represented by the model. For the entire section the mean of $r_{eff,eR}$ is $32.6 \mu m$ and the MODIS mean $r_{eff,mod}$ is $34.4 \mu m$, implying a reasonable parameterization of the ice effective radius by the IFS r_{eff} parameterization. Figure 5.7f and Fig. 5.7g show vertical profiles of LWC and IWC , which are dominated by the presence of ice but also containing minor amounts of LWC in the first part between 13:37 and 13:44 UTC for altitudes below 8 km. Simulated $F_{BB,lib,Fu}^{\uparrow}$ and $F_{BB,lib,Ba}^{\uparrow}$ agree among each other, whereby deviations increase with time and reach highest values around 13:55 UTC with $10 W m^{-2}$ for the optically thinner part of the cloud. In spite of that, simulated $F_{BB,lib}^{\uparrow}$ by Fu and Baum is in good agreement with the observations for the optical thicker section. Contemporaneous, measured $F_{BB,mea}^{\uparrow}$ ranges between 500 and $620 W m^{-2}$. Deviations between $F_{BB,mea}^{\uparrow}$ and the simulations increase with time leading to differences of up to $100 W m^{-2}$. Both libRadtran reference simulations follow the observations just within the measurement uncertainty range. The fading cloud structure at the end of CC#2 is not sufficiently represented. The increasing underestimation of F_{BB}^{\uparrow} by ecRad and libRadtran Fu with time is directly correlated with decreasing cloud geometrical and cloud optical thickness. As a result of lower τ , size and shape effects of individual ice particles become relevant, which are better resolved by the libRadtran Baum than in libRadtran Fu or ecRad Fu simulations. Further on, the Baum parameterization includes various ice crystal shapes, being closer

Table 5.7: Mean and median values of microphysical / macrophysical properties, irradiances F , solar zenith angle (SZA), and flight parameters of ice cloud #2.

	SMART	ecRad	libRadtran			
			Fu		Baum	
F_{BB}^\uparrow (W m^{-2})	545 541	446 446	464 503	484 516		
F_{B9}^\uparrow (W m^{-2})	102 101	85 89	88 96	90 97		
F_{B6}^\uparrow (W m^{-2})	20 20	12 13	17 17	20 20		
α_{BB}	0.85 0.84	0.69 0.72	0.72 0.76	0.73 0.78		
α_{B9}	0.92 0.92	0.78 0.82	0.79 0.87	0.82 0.87		
α_{B6}	0.36 0.37	0.24 0.25	0.33 0.33	0.37 0.38		

to the natural shape variety of ice clouds. In Tab. 5.7 the mean and median values of F^\uparrow and α of CC#2 are summarized.

PDFs of broadband and spectral α for CC#2 are presented in Fig. 5.13. The distributions of α_{BB} and α_{B9} of all simulations are shifted to lower values compared to the observations. The largest bias is present between $\alpha_{BB,mea}$ and $\alpha_{BB,eR}$ with -0.16 followed by $\alpha_{BB,lib,Fu}$ (-0.13) and $\alpha_{BB,lib,Ba}$ (-0.12). The general underestimation of broadband F^\uparrow and α by the models compared to the observations is related to an underestimation IWC in the IFS AD. However, with the same spectral bias as present in CC#1 significant deviations appear for $\alpha_{B6,eR}$, underestimating α by 0.12 compared to all other simulations and the measurements. This further points out the weakness of ecRad to account for ice absorption properly particularly for thin ice clouds.

Boundary Layer Clouds

The separation for ice and liquid water clouds shows significant relative differences of 33 % in F_{BB}^\uparrow between the observations and both models for the liquid water section, which was dominated by low-level boundary layer clouds (BLC). Appropriate representation of BLC in NWP is challenging as the IFS cloud module is known for its deficiency to maintain sufficient LWC in the lowest model grid-boxes (Forbes and Ahlgrimm, 2014). By that, no supersaturation is reached and the cloud module does not diagnose a cloud in the grid-box and, hence, neither represents the cloud in cloud fraction nor in LWC . Both results in an underestimation of F_{BB}^\uparrow and α_{BB} by the models compared to reality. The systematic underestimation of F_{BB}^\uparrow of BLC is clearly visible in the time series of Fig. 5.7b. To investigate the representation of these clouds in the IFS AD and the ecRad simulations a characteristic flight section between 14:10 and 14:43 UTC is selected, which is refereed as CC#3 in the following. Besides CC#3, similar cloud scenes were overflown between 12:16 and 13:22 UTC, as well as between 16:16 and 17:22 UTC.

For the aforementioned BLC sections the simulated F_{BB}^\uparrow by ecRad and libRadtran (benchmark) are systematically lower compared to the observations. For distinctive periods, e.g., around 13:10 UTC, the relative differences between the models and $F_{BB,mea}^\uparrow$ are up to 47 %. Since even libRadtran is not able to correctly simulate F_{BB}^\uparrow the spectrally independent disparity is directly related to error-prone cloud representation by LWC and f in the IFS AD.

The vertical profiles of LWC and f (Fig. 5.7f and Fig. 5.7g) indicate the limited cloud occurrence. For CC#3 a mean LWP_{eR} of 54.5 g m^{-2} is calculated, which is 30 % lower than the MODIS retrieved mean LWP_{mod} of 77.4 g m^{-2} . Evaluation of the IFS AD by HAMP radar and microwave measurements is limited as no retrievals of LWP_{mea} are available and the observed radar reflectivity Z is restrained as the radar echo of these BLC is below the instruments sensitivity.

Directly related to an underestimation of LWC and f is a systematically smaller $r_{eff,eR}$ (Fig. 5.7e) compared to the MODIS retrieved $r_{eff,mod}$ confirming the cloud miss-representation. Nevertheless, the MODIS retrieval is potentially shifted towards larger values by the cloud field heterogeneity and the clouds sub-pixel sizes below 250 m, which bias $r_{eff,mod}$ (Oreopoulos and Davies, 1998a,b). Therefore,

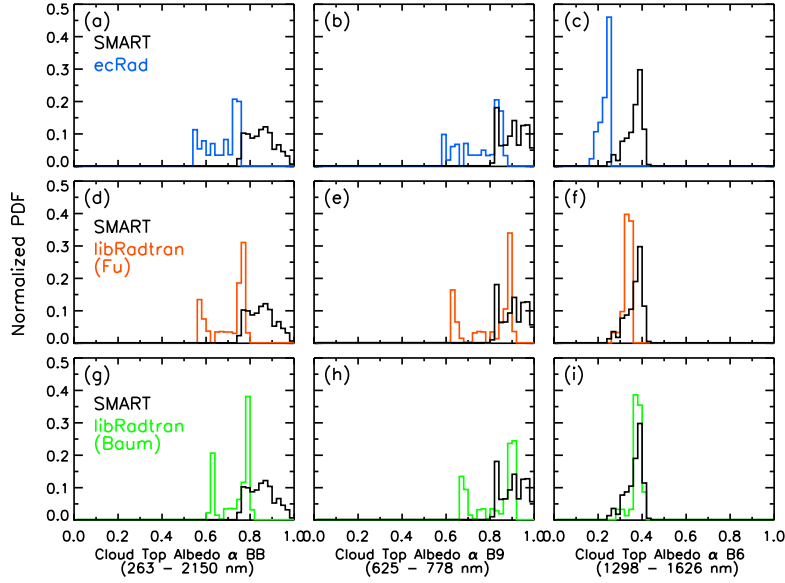


Figure 5.13: Probability density functions (PDF) of broadband and spectral cloud top albedo α from SMART observations and ecRad Fu, libRadtran Fu, and libRadtran Baum model set-ups of CC#2.

$r_{\text{eff},\text{mod}}$ is regarded as a first indication only.

In accordance to lower F^\uparrow the PDFs of simulated broadband and spectral α are also affected by the erroneous cloud representation. The resulting distributions are given in Fig. 5.14a–i and Tab. 5.8 lists the mean and median values of broadband and spectral F^\uparrow and α .

In general, the PDFs of simulated α_{BB} are broaden and shifted towards lower values by approximately 0.13 compared to $\alpha_{\text{BB},\text{mea}}$. The distributions of ecRad Fu, libRadtran Fu, and libRadtran Baum are characterized by bi-modal (B6) or tri-modal distributions (BB and B9). The lowest peak is caused by cloud-free model columns and determined by the sea surface albedo. The other two peaks are related to individual cloud cells (second mode) and to more aggregated cloud fields (third mode). Contrarily, the PDFs of α_{mea} are characterized by mono-modal (B6) and bi-modal (BB and B9) distributions, missing the lowest peak as SMART received scattered radiation from clouds almost all the time.

The number of cloud-free columns in the simulations bias the mean and median values of α towards smaller values. However, comparing only the second and third mode of the distributions, a good agreement is found. While $\alpha_{\text{BB},\text{eR}}$ is shifted to lower values by approximately -0.05, the libRadtran Fu and Baum parameterization are matching with SMART. An exception appears for B6 where the second mode (individual clouds) of ecRad agrees with the measurements, whereby libRadtran Fu and Baum overestimate SMART derived $\alpha_{\text{B6},\text{mea}}$ by up to 0.1. One reason could be the lower $r_{\text{eff},\text{eR}}$ in the model, which artificially enhances scattering and can explain the lower frequency of occurrence in α of the second mode in the simulations.

From CC#3 it is concluded that BLC are not appropriately represented in the IFS AD, leading to cloud-free model grid-boxes and to an underestimation of F^\uparrow and α for regions, where optically thin clouds are diagnosed. For combinations of f and LWC the parameterized $r_{\text{eff},\text{eR}}$ by IFS is lower than the observed estimate of r_{eff} , which partly counterbalances the missing f and LWC by enhanced scattering on smaller cloud particles. Therefore it is suggested, to revise the IFS cloud module to better simulate BLC with respect to LWC and f . Further on, the dependence of different combinations of f and LWC on estimated $r_{\text{eff},\text{eR}}$ as well as simulated F^\uparrow and α must be investigated in separate sensitivity studies.

5.7.3 Upward Irradiance of Trade Wind Cumuli

Fields of trade wind cumuli in the (sub-)tropical Atlantic basin are characterized by horizontal sizes of only several hundreds of meters but well below the grid-box size of IFS. These clouds are heterogeneously distributed and show tendencies for self-aggregation (Bony et al., 2017). Under these circumstances it is difficult to obtain representative simulations of F^\uparrow and on a basis of the IFA. This

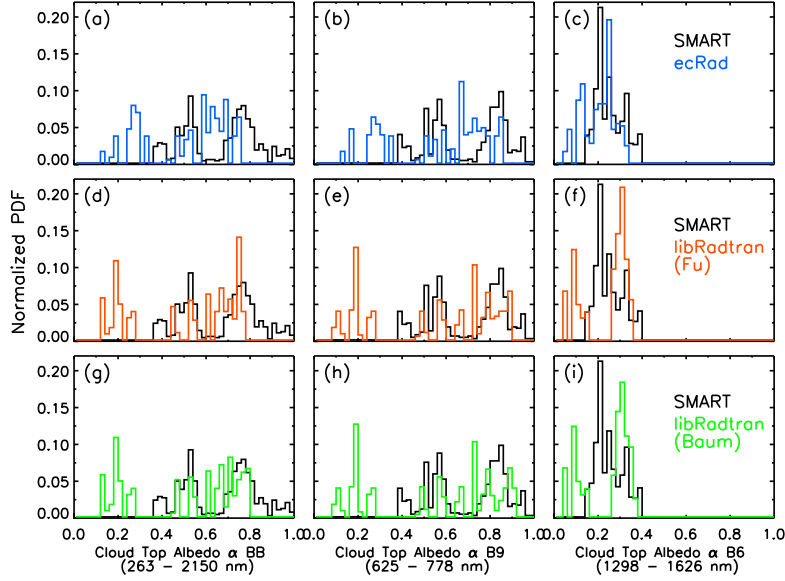


Figure 5.14: Probability density functions (PDF) of broadband and spectral cloud top albedo α from SMART observations and ecRad Fu, libRadtran Fu, and libRadtran Baum model set-up of the boundary layer cloud case (CC#3).

Total Cloud Cover

The ecRad sensitivity study in section 5.3 showed that simulated F^\uparrow is predominantly determined by the total cloud cover f_{tot} . It is used as an indicator for the along-track cloud distribution. Therefore, estimated $f_{\text{tot,eR}}$ from ecRad, $f_{\text{tot,lib}}$ derived by libRadtran, and SMART observed $f_{\text{tot,mea}}$ are compared in the following. The resulting PDFs are plotted in Fig. 5.15 with ecRad $f_{\text{tot,eR}}$ in blue, libRadtran $f_{\text{tot,lib}}$ given in green, and the SMART observed $f_{\text{tot,mea}}$ in black. The distribution of $f_{\text{tot,mea}}$ is characterized by a dominating fraction of cloud-free samples and measurements, where $f_{\text{tot,mea}}$ is below 20 %. For $f_{\text{tot,eR}}$ and $f_{\text{tot,lib}}$ the cloud-free mode is reduced and both PDFs are shifted to larger f_{tot} , indicating for generally higher cloud cover in the models. In particular, $f_{\text{tot,lib}}$ shows a second prominent mode at around f_{tot} of 75 %. For the entire RF06 median values of $f_{\text{tot,eR}} = 23.8 \%$, $f_{\text{tot,lib}} = 45.5 \%$, and $f_{\text{tot,mea}} = 4.0 \%$ are determined. The significant lower median of $f_{\text{tot,mea}}$ is caused by the line sampling strategy of the upward radiance and the limited instruments FOV, hence, not being able to derive representative $f_{\text{tot,mea}}$ for the entire grid-box in heterogeneous cloud conditions.

In general, libRadtran determines larger f_{tot} than ecRad or SMART. Deviations in f_{tot} between ecRad and SMART decrease with time and show better agreement for the second part of the flight. The aggregation of individual clouds leads to cloud cluster with an increased likelihood to be captured by the SMART radiance inlet, which allows to derive more representative $f_{\text{tot,mea}}$ with respect to the entire grid-box. However, the differences among libRadtran and ecRad result from the interpretation of the COA parameterization in the RTS and emphasize the importance of cloud scene dependent COA.

Due to diurnal cycle of tropical clouds, as a result of the intense insolation, the presented RF06 is divided in two cloud scenes. The first part (P1), from 13:00 to 16:30 UTC, is characterized by limited convective activity and individual cloud cells. The second part (P2), after 16:30 UTC, shows more developed and adjoined cloud structures, which leads to an increase of f_{tot} with time.

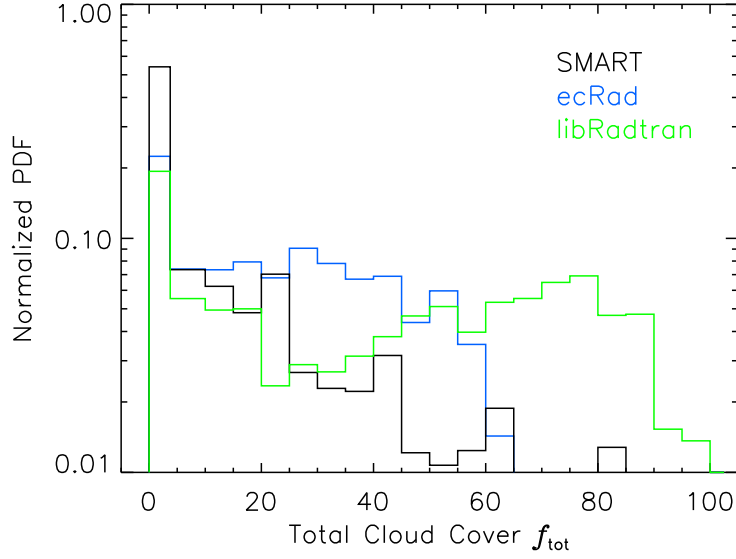


Figure 5.15: Probability density function of total cloud cover f_{tot} of ecRad (blue), libRadtran (green), and SMART (black) of the entire research flight 06 (RF06) from 19 August 2016 during NARVAL-II.

Broadband Upward Irradiance

Figure 5.16a shows simulated upward solar irradiance from ecRad $F_{\text{BB,eR}}^{\uparrow}$ (blue), the libRadtran benchmark simulation $F_{\text{BB,lib,Fu}}^{\uparrow}$ (green), and measured $F_{\text{BB,mea}}^{\uparrow}$ (black + gray uncertainties) by SMART. The same color code is applied for all following panels. Figure 5.16b and Fig. 5.16c show spectral F_{B6}^{\uparrow} and F_{B9}^{\uparrow} , respectively. Subsequently, Fig. 5.16d and Fig. 5.16e present MODIS (orange) retrieved τ_{mod} and $r_{\text{eff,mod}}$ as well as SMART (black dots) derived τ_{mea} and $r_{\text{eff,mea}}$. Simulated τ_{eR} and $r_{\text{eff,eR}}$ by ecRad are indicated in blue. Below, f_{tot} from ecRad $f_{\text{tot,eR}}$ (blue), libRadtran $f_{\text{tot,lib}}$ (green), and SMART $f_{\text{tot,mea}}$ (black) are given. In Fig. 5.16g the retrieved cloud droplet number concentration N from the synergetic SMART and HAMP retrieval is plotted in black with uncertainties given in gray. The selected N of 50 cm^{-3} activated cloud droplets, utilized in the ecRad simulations, is indicated by the blue line.

In spite of the higher f_{tot} diagnosed by the model compared to $f_{\text{tot,mea}}$, the observed $F_{\text{mea}}^{\uparrow}$ within P1 is systemically overestimating both models, when $f_{\text{tot,mea}}$ is larger than 10 %. The lowest irradiances are simulated by libRadtran. Due to the definition of hemispheric irradiance, SMART receives radiation not only from directly below the aircraft but also from cloud covered areas, which are not represented in the single column simulations. In regions where the total cloud cover exceeds 20 % the simulated F^{\uparrow} matches with the observations within the SMART uncertainty range. Individual spikes of F^{\uparrow} , e.g., at 14:00 or 16:00 UTC, are caused by rapidly developing cumulus clouds, whose fast rapid cloud evolution is not captured in the hourly IFS AD.

The relative differences between simulated and observed F^{\uparrow} are larger for F_{BB}^{\uparrow} and F_{B9}^{\uparrow} than for F_{B6}^{\uparrow} . This spectral feature is caused by aerosol particles and gases, both contributing to the scattered radiation from the cloud. To quantify the influence of aerosol particles, additional libRadtran simulations are conducted. The inclusion of aerosol in the libRadtran calculations leads to a systematic increase in F^{\uparrow} for wavelength below 1200 nm. Therefore, the larger relative differences in observed and simulated F^{\uparrow} for $\lambda < 1200 \text{ nm}$ are addressed to the presence of multiple aerosol layers, whose occurrence is confirmed by WALES backscatter measurements. Additionally, the general low cloud top height, ranging from 1000 to 1500 m, and a flight altitude around 12 km causes considerable scattering on atmospheric constituents, including the high relative humidity in the subtropical region, which contributes to the scattered radiation observed by SMART.

To exclude potential errors in simulated F^{\uparrow} due to the number of applied streams in the RTS of ecRad and libRadtran, the libRadtran simulations are repeated for two-stream calculations. By

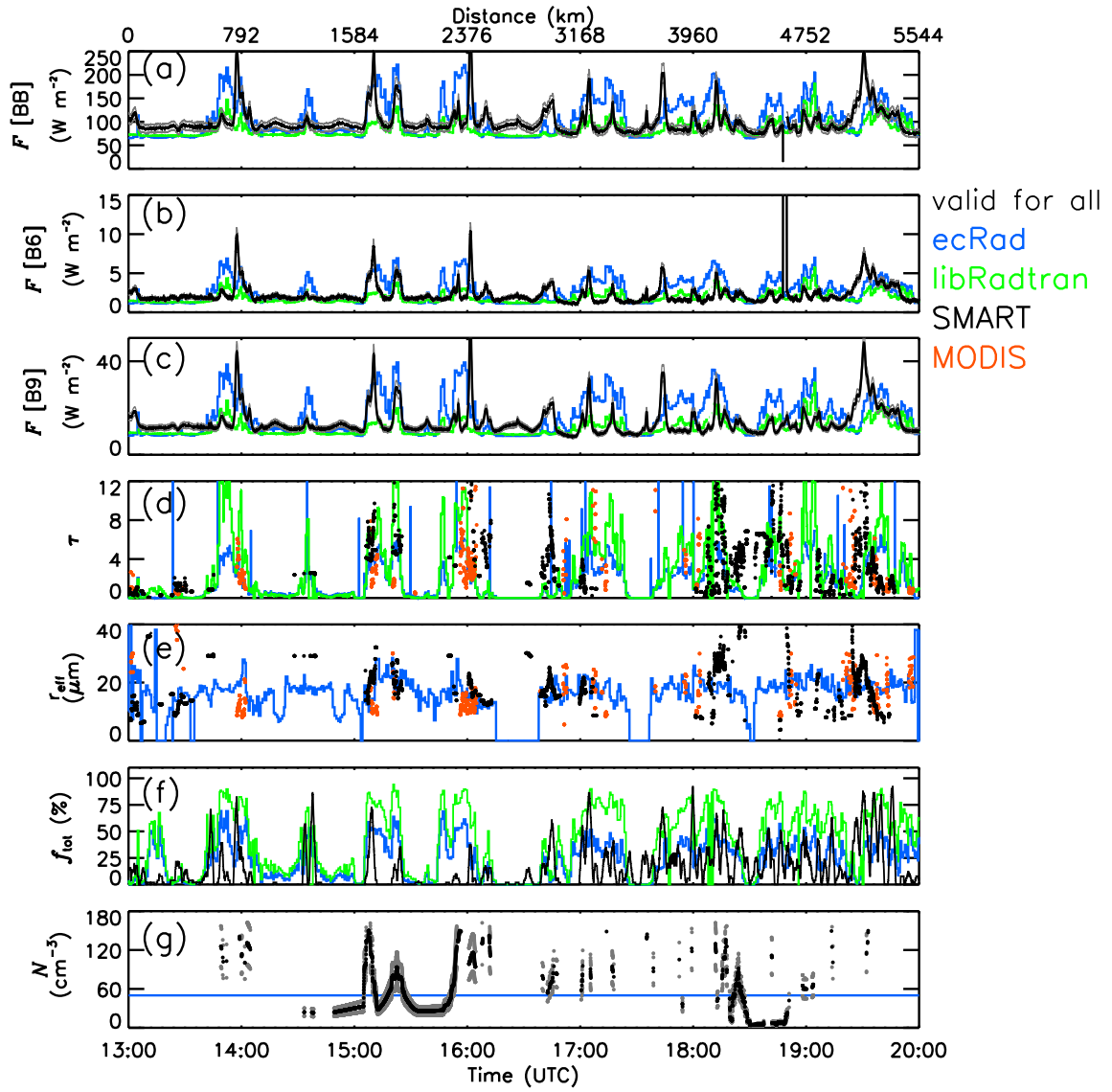


Figure 5.16: Time series of entire flight between 13:00 and 20:00 UTC, which is 09:00 to 16:00 local time. The panels of the plot show a–c) measured and simulated upward irradiance F , d) cloud optical thickness τ , e) effective radius r_{eff} f) total cloud cover f_{tot} , and in g) the estimated cloud droplet number concentration N from the synergetic SMART and HAMP retrieval.

that, maximum relative differences in F^\uparrow below 0.5 % for the VIS and NIR spectral range are found. Therefore, the influence of the number of streams is negligible and the two-stream simulations in ecRad provide reliable estimates of F for heterogeneous cloud scenes and SZA between 2 and 55°.

Figure 5.16d compares cloud optical thickness from ecRad τ_{eR} (blue) and libRadtran τ_{lib} (green) with available retrievals of τ_{mea} (black) from SMART and MODIS τ_{mod} (orange). In spite of the overestimation of F^\uparrow and underestimation of f_{tot} by ecRad in relation to libRadtran, the resulting τ_{eR} and τ_{lib} are matching for most of the time. This is caused by the counterbalancing effect, that in-cloud radiative fluxes and τ are scaled by f_{tot} within the radiation solver. Significant differences in simulated τ appear around 13:50 and 17:00 UTC, where τ_{lib} exceeds τ_{eR} by more than a factor of two. Until 18:00 UTC τ from SMART and MODIS are in the same range as ecRad and libRadtran, indicating reasonable agreement among the observations and simulations. This indicates that the optical thickness of the individual trade wind cumuli is properly determined by ecRad. Afterwards, derived τ_{mod} and τ_{mea} fluctuate and are potentially prone to errors due to the presence of multi-layer clouds, which complicates the τ retrieval. The same issues arise for the retrieved $r_{\text{eff,mea}}$ shown in Fig. 5.16e. However, the general agreement of $r_{\text{eff,eR}}$ with $r_{\text{eff,mea}}$ demonstrates, that the calculated droplet sizes $r_{\text{eff,eR}}$ are reasonable, in spite of the constant N in the simulations.

Figure 5.16f presents the timeseries of f_{tot} and shows the systematic overestimation of f_{tot} by libRadtran compared to ecRad and the SMART observations. For the first part P1 $f_{\text{tot,eR}}$ exceeds $f_{\text{tot,mea}}$ but for P2, with the aggregated cloud fields, ecRad and SMART are mostly matching.

In Fig. 5.16g, the estimated N from the synergetic retrieval is indicated by the black dots with relative uncertainties of ± 25 % (gray). Due to the variable cloud base height during RF06, only method B of the synergetic retrieval could be applied. The flight sections between 14:45 and 16:00 UTC as well as between 18:20 and 19:00 UTC are characterized by aggregated clouds, which allow to derive estimates of N . Nevertheless, the horizontal heterogeneity of the cloud field and the size of individual trade wind cumuli limit the available data set. Figure 5.16g clearly shows that the average retrieved N is below the IFS applied N of 50 cm^{-3} , implying for observed clouds, which are more pristine with larger cloud droplets. In spite of higher N in ecRad the simulated F^\uparrow agrees with the observations within the uncertainty range. Further simulations of F_{eR}^\uparrow by ecRad, utilizing constant N of 30 cm^{-3} and the retrieved N , lead to relative difference in F_{eR}^\uparrow below ± 7 % and ± 11 %, respectively. This is supported by the conclusions of the sensitivity analysis (see section 5.5), which showed that changes in N do not influence F considerably compared to variations in f_{tot} or LWP . Therefore, potential inaccuracies in F due to inaccurate estimates of N or related r_{eff} are masked by forecast errors in f and the reduced susceptibility of ecRad on N . The mean and median values of the cloud macrophysical and microphysical properties, upward irradiance F^\uparrow , and cloud top albedo α are listed in Tab. 5.9.

To statistically compare the simulated along-track radiation field with the observations, PDFs of F^\uparrow are calculated. Figure 5.17 presents the PDFs of $F_{\text{BB,eR}}^\uparrow$ (blue), $F_{\text{BB,lib}}^\uparrow$ (green), and $F_{\text{BB,mea}}^\uparrow$ (black) of the entire RF06. All distributions of F_{BB}^\uparrow are skewed to the right and are dominated by F_{BB}^\uparrow below 100 W m^{-2} due to the majority of flight sections with f_{tot} below 20 %. The lowest peak appears for $F_{\text{BB,eR}}^\uparrow$ with a median of 87.2 W m^{-2} while the PDF of $F_{\text{BB,lib}}^\uparrow$ shows a median of 77.1 W m^{-2} and a SMART median of 90.4 W m^{-2} . The contradicting values of the maximum peak, the median and the mean of the distributions, depicts the skewness of the PDFs. In general, the relative difference of F_{BB}^\uparrow between ecRad and SMART is within the measurement uncertainty range, indicating that the IFS AD captures the cloud situation reasonable well and the RTS are able to represent the observed radiation pattern. Contrarily, the relative differences between libRadtran and SMART are larger, on average by -14.7 %, pinpointing for too low cloud top reflectivity.

Spectral Upward Irradiance

To identify systematic spectral offsets, Fig. 5.18a-f shows PDFs of broadband and spectral α from ecRad (orange), libRadtran (green), and SMART (black) of the entire flight. In spite of the differences in observed and simulated f_{tot} , the shapes of the distributions of α are generally matching. All distributions are dominated by low α , causing the mode around α 0.08, which is close to the model sea surface albedo. PDFs of α_{BB} and α_{B9} are shifted towards larger values of α and are more broaden compared to the narrow distribution of α_{B6} . BB and B9 are more affected by scattering processes and are more sensitive to optical thin clouds ($\tilde{\omega} \approx 1$) compared to B6, where absorption prevails.

Table 5.9: Mean and median values of microphysical and macrophysical properties, upward irradiance F^\uparrow , and cloud top albedo α for the entire research flight 06 and filtered for clouds with total cloud cover $f_{\text{tot}} < 20\%$.

	SMART	ecRad	libRadtran	MODIS
	Fu			
TCC	0.56	0.39	0.61	0.88
Flight Altitude (m)	12049			-
F_{BB}^\uparrow (W m^{-2})	100 90	83 77	101 87	-
F_{B9}^\uparrow (W m^{-2})	14 12	16 13	11 10	-
F_{B6}^\uparrow (W m^{-2})	2 2	3 2	2 2	-
α_{BB}	0.10 0.09	0.10 0.09	0.09 0.07	-
α_{B9}	0.08 0.07	0.09 0.07	0.07 0.06	-
α_{B6}	0.03 0.03	0.03 0.03	0.02 0.02	-
LWP (kg m^{-2})	0.0297	0.0131	0.0505	
r_{eff} (μm)	16.4	15.7	19.0	
CTH (m)	-	4938	2310	
cloud only $f_{\text{tot}} > 20\%$				
F_{BB}^\uparrow	121 109	125 123	88 86	-
F_{B9}^\uparrow	19 16	21 20	13 12	-
F_{B6}^\uparrow	3 3	3 3	2 2	-
α_{BB}	0.14 0.13	0.14 0.14	0.10 0.10	-
α_{B9}	0.12 0.10	0.14 0.13	0.08 0.08	-
α_{B6}	0.05 0.04	0.05 0.05	0.03 0.03	-
LWP (kg m^{-2})	0.0537	0.0240	0.0463	
r_{eff} (μm)	16.2	17.8	18.5	
CTH (m)	-	3250	1599	

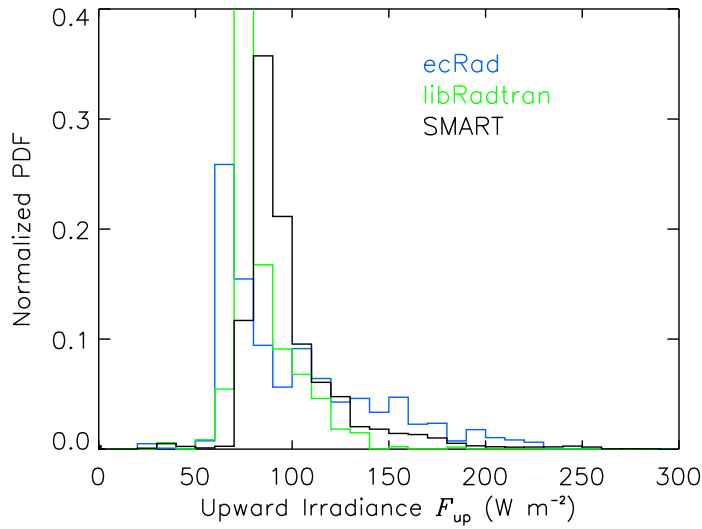


Figure 5.17: Probability density functions of upward broadband irradiance F_{BB}^\uparrow of ecRad (blue), libRadtran (green), and SMART (black) of the entire research flight 06 (RF06) conducted on 19 August 2016 during NARVAL-II.

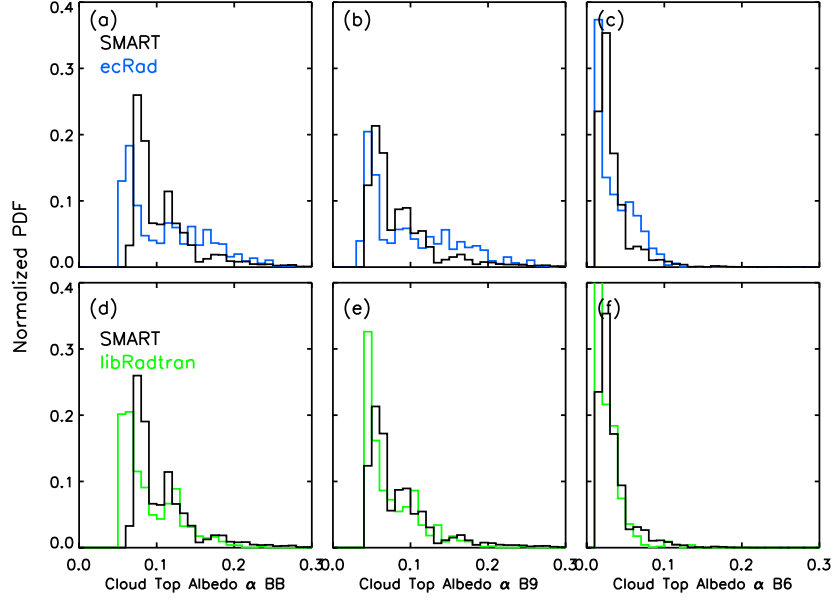


Figure 5.18: Probability density functions (PDF) of the spectral and broadband albedo α from ecRad (blue), libRadtran (green), and SMART (black) for the entire RF06 conducted on 19 August 2016.

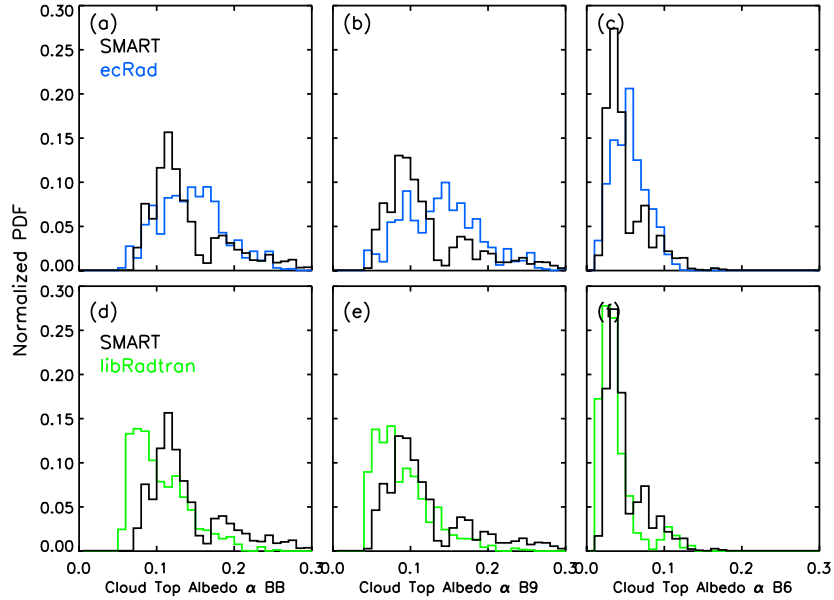


Figure 5.19: Probability density functions (PDF) of the spectral and broadband cloud top albedo α from the SMART observations and the different model set-ups filtered for total cloud fraction $f_{\text{tot}} > 20\%$ of the entire RF06 from the 19. August 2016.

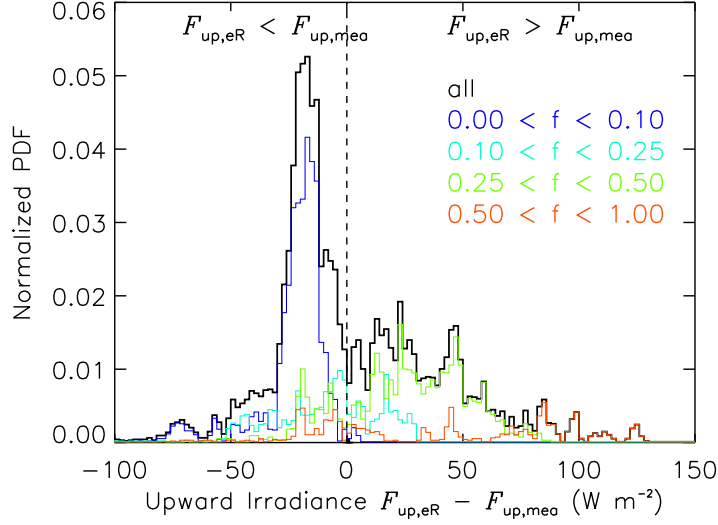


Figure 5.20: Probability density functions (PDF) of absolute difference between simulated $F_{\text{BB,eR}}^{\uparrow}$ and observed $F_{\text{BB,mea}}^{\uparrow}$ upward irradiance of RF06. The black line represents the entire flight. Color coded histograms separate for different total cloud cover $f_{\text{tot,eR}}$ diagnosed by the ecRad scheme.

Due to the dominance of cloud-free sections and to focus on the cloud representation, pixels with $f_{\text{tot,eR}} < 20\%$ are excluded. By that, only cloud samples are selected, which are regarded to be present in the IFS AD and are captured by SMART at the same time and location. The filtered PDFs are shown in Fig. 5.19a-f. The according mean and median values are given in Tab. 5.9. The removal of cloud-free columns generally broadens the PDFs and shifts them towards larger α . Additionally, a second mode at around 0.18 is enhanced, representing cloud covered model columns.

The libRadtran and SMART distributions of α for BB and B9 are systematically lower than ecRad and are skewed to the right, while PDFs of α_{eR} of BB and B9 are normally distributed. This spectral feature follows the results from the ecRad sensitivity study, where ecRad simulates trade wind cumuli, with LWP between 50 and 100 g m^{-2} , with a reduced susceptibility on variations in LWP and f_{tot} . By that, a higher frequency of occurrence in intermediate α arises. The bi-model distribution of SMART and libRadtran are matching in shape, which indicates that the latter one, on basis of the IFS AD, is able to represent the observed natural variability in α .

Form the spectral analysis of F^{\uparrow} and α it is concluded, that ecRad is able to represent the observed trade wind cumuli cloud field in general, whereby local radiative effects of cloud clusters are likely underestimated for LWP below 50 g m^{-2} and overestimated for LWP above 100 g m^{-2} .

Influence of Total Cloud Cover and Liquid Water Path on Upward Irradiance

To analyze the influence of different cloud scenarios, represented by f_{tot} , the PDFs of absolute difference $\Delta F^{\uparrow} = F_{\text{BB,eR}}^{\uparrow} - F_{\text{BB,mea}}^{\uparrow}$ are separated for bins of $f_{\text{tot,eR}}$. Figure 5.20 shows the distributions, where the solid black line represents the entire RF06, while different bins of $f_{\text{tot,eR}}$ are color coded. The dashed black line at 0 W m^{-2} indicates similar values of F_{BB}^{\uparrow} from the simulations and the observations. The PDF of the entire flight (black) shows a dominant peak at -20 W m^{-2} and reveals that the model generally underestimates the observed $F_{\text{BB,mea}}^{\uparrow}$. This peak is caused by flight sections where $f_{\text{tot,eR}}$ is below 10 %, confirmed by the PDF for binned $f_{\text{tot,eR}} < 10\%$ (blue line), representing almost cloud-free columns. For $10\% < f_{\text{tot,eR}} < 25\%$ no distinctive peak of the PDF (light blue) is present and the distribution spreads between -50 and 30 W m^{-2} . With further increasing $f_{\text{tot,eR}}$ (green), ranging from 25 to 50 %, the second mode of the black curve is explained. This local maximum indicates for a potential bias in the model of approximately 20 to 50 W m^{-2} towards larger

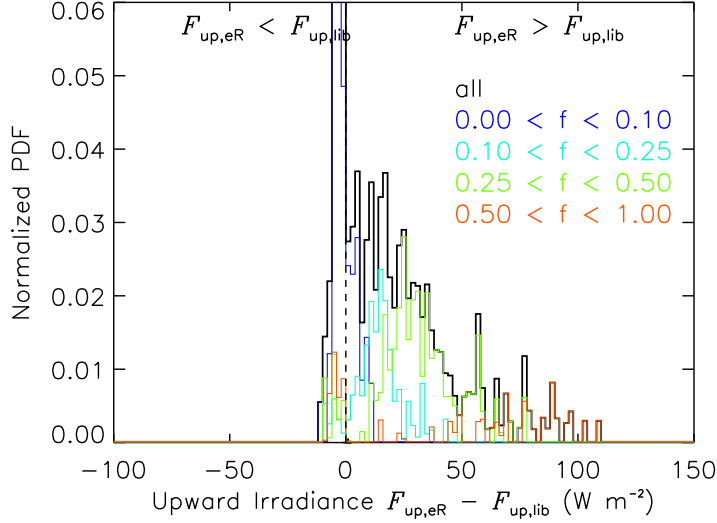


Figure 5.21: Probability density functions (PDF) of absolute difference between simulated $F_{\text{BB,eR}}^{\uparrow}$ and $F_{\text{BB,lib}}^{\uparrow}$ of upward irradiance during RF06. The black line represents the entire flight. Histograms are separated and color coded for total cloud cover $f_{\text{tot,eR}}$ diagnosed by ecRad.

F_{BB}^{\uparrow} compared to the observed $F_{\text{BB,mea}}^{\uparrow}$. Model columns with $f_{\text{tot,eR}} > 50\%$ contribute to the largest positive bias in the model by dominating the shape of the solid black PDF for F_{BB}^{\uparrow} above 80 W m^{-2} . This indicates that regions with low cloud cover underestimate F^{\uparrow} , while areas with cloud cover above 50 % overestimate F^{\uparrow} .

Figure 5.21 shows PDFs of absolute differences in F_{BB}^{\uparrow} between ecRad and libRadtran separated for $f_{\text{tot,eR}}$. The evaluation among both models guarantees the collocation of clouds and potential biases in F^{\uparrow} due to errors in the IFS AD are omitted. The PDF of the entire flight (black) is shifted to positive values with a median around 30 W m^{-2} , indicating for systematically higher $F_{\text{BB,eR}}^{\uparrow}$ compared to libRadtran. Both models agree for $f_{\text{tot,eR}}$ below 10 % (blue). The differences in F_{BB}^{\uparrow} among the models are getting larger with increasing $f_{\text{tot,eR}}$. The PDF of the entire flight is dominated by model columns with $f_{\text{tot,eR}}$ between 25 and 50 % (green), indicating that these $f_{\text{tot,eR}}$ are responsible for most (in frequency) of the deviations among the models. The largest bias between ecRad and libRadtran is related to model columns with $f_{\text{tot,eR}}$ above 50 %, potentially caused by the different interpretation of the COA in the RTS.

By comparing the PDFs of Fig. 5.20 and Fig. 5.21 it is concluded, that the majority of the samples in Fig. 5.20 with absolute differences in F_{BB}^{\uparrow} below -20 W m^{-2} are caused by cloud-free model columns, where SMART received reflected radiation from clouds, which are not present in the simulations either due to the IPA, a displacement of clouds, or a misrepresentation in IFS AD by f_{tot} and LWC .

Figure 5.22 shows absolute differences of F_{BB}^{\uparrow} between ecRad and the observations ($F_{\text{BB,eR}}^{\uparrow} - F_{\text{BB,mea}}^{\uparrow}$, color coded). An overestimation of F_{BB}^{\uparrow} by ecRad compared to SMART is indicated by blue and light blue, while an underestimation by ecRad is represented by dark blue and black colors. Estimates of LWP_{mea} are provided by the HAMP microwave profiler. The plotted LWP - f -space is divided in four regimes. The first quadrant (upper right) with $f_{\text{tot,eR}} > f_{\text{tot,mea}}$ and $LWP_{\text{eR}} > LWP_{\text{mea}}$ comprises model clouds overestimating f_{tot} and LWP of the grid-box. Contrarily, quadrant III (lower left) contains cloud segments, which are underrepresented in f and LWP in the IFS AD with respect to the HALO observations. The other two quadrants separate for f and LWP accordingly. The black area in the center marks the confidence area, resulting from the measurement uncertainties in f_{tot} of $\pm 5\%$ and in LWP of 30 g m^{-2} . In this area, differences in F_{BB}^{\uparrow} can not be clearly separated for f and LWP .

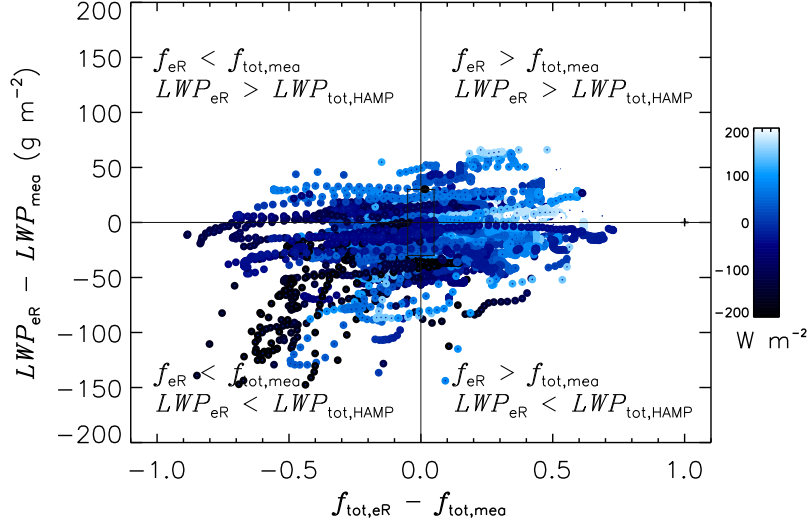


Figure 5.22: Absolute differences in simulated and observed broadband upward irradiance F_{BB}^{\uparrow} between ecRad and SMART (color coded in blue), separated for absolute differences in total cloud cover f_{tot} and liquid water path LWP between IFS model data and SMART and HAMP, respectively.

For RF06, a total of 15102 individual simulations are available. 2352 cloud pixels (15.6 %) are inside the confidence area and removed from the total population. In quadrant IV the most cloud samples are found with 5326 (41.8 %) out of the total population, which indicates that the majority of the clouds in ecRad tend to have higher values of f and, simultaneously, lower LWP compared to the observations. This results in an underestimation of F_{BB} by ecRad shown by the colors ranging from dark blue to black. Quadrant I contains 2844 cloud pixels (22.3 %) of the total pixel number and is the second frequent error combination. Due to $LWP_{\text{eR}} > LWP_{\text{mea}}$ and $f_{\text{tot,eR}} > f_{\text{tot,mea}}$, simulated $F_{\text{BB,eR}}^{\uparrow}$ is larger compared to $F_{\text{BB,mea}}^{\uparrow}$, which is indicated by the colors ranging from blue to white. Quadrant III contains 2396 (18.8 %) pixels and quadrant II contains 781 pixels (6.1 %), only contributing to a minor fraction to the deviations. In these LWP - f -spaces the counterbalancing effects of f_{tot} and LWP lead to minor absolute differences in the simulated radiation, which are in the range of $\pm 30 \text{ W m}^{-2}$.

The comparison of Quadrant I and Quadrant IV (larger model f_{tot}), which comprise 64.1 % of all pixels, with Quadrant II and Quadrant III (smaller model f_{tot}), which include 24.9 % of all pixel, supports the previous conclusion that the simulated trade wind cumuli are more sensitive on changes in f_{tot} than LWP , independent of absolute values of LWP . However, the separation for f_{tot} is prone to errors, as the representativeness of SMART derived $f_{\text{tot,mea}}$ remains questionable.

6 Summary and Conclusions

Within this work measurements from the Next Generation Remote Sensing for Validation Studies (NARVAL-II, Stevens et al. 2019) and the North Atlantic Waveguide and Downstream impact Experiment (NAWDEX, Schäfler et al. 2018) field campaigns are analyzed. During these campaigns measurements of upward and downward irradiance F in the solar wavelength range from 266 to 2050 nm are conducted by the Spectral Modular Airborne Radiation measurements sysTem (SMART) on board of the High Altitude and Long Range Research Aircraft (HALO) of the German Aerospace Center (DLR). Additional observations of the atmosphere below HALO are acquired by a combination of an active cloud radar and a microwave profiler, called HALO Microwave Package (HAMP). The suite of remote sensing instruments is completed by the Water Vapour Lidar Experiment in Space (WALES), the spectrometer of the Munich Aerosol Cloud Scanner (specMACS), and a dropsonde measurement system.

Upward and downward F measured along the flight path of HALO are compared with respective simulated along-track F in flight altitude. The simulations are performed with the ecRad radiation module of the Integrated Forecast System (IFS) of the European Centre for Medium Range Weather Forecast (ECMWF). ecRad is run as an offline version independently of the IFS host system. This requires the set-up of a local system, handling the import of the IFS analysis data (IFS AD), controlling the Radiative Transfer Simulations (RTS), and directing the output of the calculated F profiles.

Additional simulations of F with the library for Radiative transfer (libRadtran) are performed for several ice crystal shape parameterizations following Fu (1996) and Fu et al. (1998a), and Baum et al. (2005a). libRadtran simulations provide along-track simulated F on basis of spectrally higher resolved ice crystal parameterizations and, therefore, results from this radiative transfer model are regarded as a benchmark for ecRad. Both RTS are initialized with the same IFS AD. By that, differences among simulated and observed F are separated for cloud errors in the IFS AD and issues within the cloud optics parameterizations.

All simulations base on the Independent Pixel Approximation (IPA), where vertical photon transport within the column is allowed but no lateral exchange with neighboring columns. In case of large-scale stratiform clouds, this assumption is justified (Marshak et al., 1995).

The observations are spectrally interpolated to coincide with the ecRad spectral band resolution.

From NARVAL-II (RF06: 19 August 2016) and NAWDEX (RF04: 26 September 2016) one flight is chosen. By investigating three characteristic cloud sections of RF04 and the entire RF06 the following questions are answered:

- How well are ice topped clouds represented by the current optical ice parameterization of ecRad?
- How well are mid-latitude and tropical low-level liquid water clouds represented in the IFS AD?
- How does total cloud cover, liquid water content, cloud droplet number concentration, and cloud heterogeneity influence the radiative forcing of trade wind cumuli?

Uncertainties and Sensitivity of ecRad due to IFS Analysis Data

To estimate uncertainties in simulated along-track F by ecRad a sensitivity study is conducted. For each of the investigated cloud cases an average atmospheric reference profile is created and varied by the along-track variability in temperature T , pressure p , humidity q , liquid water content LWC , ice water content IWC , and total cloud cover f_{tot} . These profiles are used as input for ecRad. Resulting relative differences in simulated F for each of the aforementioned parameters with respect to the other reference profile are determined. The study shows that ecRad is most sensitive on f_{tot} ($\Delta F = \pm 12\%$) and LWC / IWC ($\Delta F = \pm 8\%$), whereby relative uncertainties from the other parameters are almost negligible. For the ecRad simulations of F an uncertainty range of $\pm 5\%$ is determined.

Uncertainties in Simulated Irradiance due to the Independent Pixel Approximation

The model set-up on basis of the IPA leads to potential differences between observed and measured F . To partly account for this shortcoming further ecRad simulations of F are performed for a field of 11×11 model columns around the aircraft nadir point. The field of simulated F is weighted with the cosine response of the SMART irradiance sensor to consider the observation geometry. By weighing and averaging over several model columns individual peaks of F^\uparrow from one column are smoothed.

The method was applied to NAWDEX RF04. For flight sections with f_{tot} close to 100 % an agreement between the IPA and non-IPA simulations as well as the observations is found, with average relative differences below $\pm 5\%$ and maximum relative differences of $\pm 7\%$. This enables to compare the IPA simulations with the along-track observations of F in case of homogeneous cloud field. However, for heterogeneous cloud scenes and decreasing f_{tot} of NAWDEX RF04 and NARVAL-II RF 06 the relative uncertainties increase but the deviations remain small compared to the cloud radiative forcing and still allow to compare simulated and measured F^\uparrow .

Ice Water Clouds

The representation of stratiform ice topped clouds in ecRad and libRadtran is analyzed on basis of two cloud cases from NAWDEX RF04. For both sections a general underestimation of broadband upward F_{BB}^\uparrow by ecRad $F_{\text{BB,eR}}^\uparrow$ and libRadtran $F_{\text{BB,lib}}^\uparrow$ between 4 % and 9 % is observed. The underestimation of F_{BB}^\uparrow is partly caused by too low F_λ^\uparrow for wavelength larger than 1200 nm. The same spectral features appear for $F_{\text{lib,Fu}}^\uparrow$ (Fu ice parameterization) but not for $F_{\text{lib,Ba}}^\uparrow$ (Baum ice parameterization). When the libRadtran Baum ice optics parameterization is used the relative differences are smaller than $\pm 5\%$ compared to the observations, which indicates for an appropriate representation of the cloud section by the IFS AD. Therefore, differences between F_{eR}^\uparrow and $F_{\text{lib,Ba}}^\uparrow$ as well as the SMART measurements are related to the ice optics parameterization and the RTS only. This leads to the conclusion, that the Fu ice optics parameterization is incapable to simulate spectral F^\uparrow sufficiently.

For a second, more heterogeneous cloud section, the ecRad Fu and libRadtran Fu simulations show a similar underestimation in broadband and spectral F^\uparrow compared to measured F_{mea}^\uparrow with the same spectral weakness of the Fu parameterization. Relative differences in F^\uparrow between the simulations and the observations increase for the optically thinner part of the cloud, highlighting the importance of the accurate representation of single scattering effects, where the size and the shape of individual particles becomes dominant. In addition, upward broadband $F_{\text{BB,lib,Ba}}^\uparrow$ (benchmark) is just below the lower SMART uncertainty range, indicating for a lack of IWC in the IFS AD, superimposing the deficiencies of the ice optics parameterization.

Retrieval of Cloud Droplet Number Concentration

In-situ observations of the cloud droplet number concentration N are not available for NARVAL-II. Therefore, an improved remote sensing method to estimate N is developed. Using passive spectral solar radiation measurements in combination with a microwave radiometer as well as observations from an active lidar and cloud radar, the synergetic effect of these instruments is exploited. The common assumption of a vertical adiabatic cloud profile is replaced by estimates of the cloud geometric thickness and retrieved liquid water path (LWP). Synthetic measurements show that the extended method allows to estimate N closer to reality and simultaneously reduce the retrieval uncertainty.

The technique is applied to NARVAL-II RF06. Using measurements of upward radiance I_λ^\uparrow by SMART allows to retrieve the cloud optical thickness τ and cloud droplet effective radius $r_{\text{eff,A}}$ at cloud top. HAMP provides retrievals of LWP and the radar reflectivity Z , which are used to separate for bins of LWP and to discriminate between non-precipitating and precipitating cloud sections. Combining measured values of I_λ^\uparrow by SMART and LWP by HAMP, alternative values of r_{eff} are retrieved, which are less influenced by 3-dimensional cloud radiative effects. Cloud-top height h_{CT} is determined by WALES while the cloud base height h_{CB} is estimated from dropsondes or radar data.

Determination of H for NARVAL-II RF06 was not possible and only method B of the retrieval is applied.

Due to the heterogeneity of shallow trade wind cumulus fields during NARVAL-II careful data filtering is applied by a cloud homogeneity identifier. This is of importance in the retrieval of τ , r_{eff} , and N as different instrument field-of-views (FOV), being in the size range of individual clouds, complicate the retrieval. Using cloud flagging and masking, the calculation of N for RF06 can be applied to approximately 55 % of all observed clouds.

Model Sensitivity on Trade Wind Cumuli

A sensitivity study with libRadtran shows, that shallow trade wind cumuli with LWP below 200 g m^{-2} and N below 100 cm^{-3} are very sensitive to changes in N . In case of a LWP of 75 g m^{-2} an increase of N from 50 to 100 cm^{-3} leads to an increase of the cloud top albedo α by 0.1. In contrast, for ecRad the sensitivity on changes in LWP and N is reduced, leading to a lower variability in F and α . By that, ecRad underestimates clouds with $LWP < 100 \text{ g m}^{-2}$ compared to $F_{\text{lib}}^{\uparrow}$, while for clouds with LWP below 75 g m^{-2} F_{eR}^{\uparrow} overestimates $F_{\text{lib}}^{\uparrow}$. As a result, the PDFs of F_{eR}^{\uparrow} and α_{eR} from ecRad for trade wind cumuli deviates from the observed distribution.

Derived cloud droplet number concentration of RF06 is compared with the applied value of 50 cm^{-3} , which is used in the simulations. On average the observed N shows a large variability, ranging from 20 to 110 cm^{-3} , emphasize that a fixed N does not capture the natural complexity of clouds. Additionally, estimated N are applied in the ecRad simulations to determined the influence on r_{eff} and calculated F . The application of retrieved N from the synergetic retrieval in the ecRad simulations shows only minor differences in F^{\uparrow} compared to the utilized N of 50 cm^{-3} of $\pm 11 \%$, further supporting the low sensitivity of the model on variations in N .

Liquid Water Clouds

The representation of liquid water clouds is analyzed on basis of a cloud section from NAWDEX RF04 (mid-latitude boundary layer clouds) and NARVAL-II RF06 (trade wind cumuli). For NAWDEX RF04 the total cloud cover f_{tot} diagnosed by ecRad and libRadtran is lower compared to the SMART derived $f_{\text{tot,mea}}$ by 5 to 10 %, indicating for fewer clouds in the IFS AD with respect to the observations. Comparison of F_{BB}^{\uparrow} and α_{BB} shows a systematic underestimation by both models, including the libRadtran reference, compared to SMART. Probability density functions of the simulations are characterized by a tri-modal distribution. The shape of the distribution is caused by cloud-free model columns (lowest α), individual cloud cells, and more aggregated cloud fields (largest α). In contrast, the PDF of the observations exhibits a bi-modal distribution, without the lowest peak (cloud-free), and is shifted to higher values of α_{BB} by 0.1. For NAWDEX RF04 it is concluded, that optical thin boundary layer clouds are partly missing in the IFS AD and, if included, are characterized by too low f and LWC , leading to the underestimation of F_{BB}^{\uparrow} and α .

NARVAL-II RF06 is characterized by heterogeneously distributed clouds, which leads to $f_{\text{tot,eR}} = 23.8 \%$, $f_{\text{tot,lib}} = 45.5 \%$, and $f_{\text{tot,mea}} = 4.0 \%$. The differences among libRadtran and ecRad result from the deviating interpretation of the cloud overlap assumption in the RTS. Significant lower $f_{\text{tot,mea}}$ is caused by the limited representation of the line observations of $f_{\text{tot,mea}}$ with respect to the entire grid box. For the entire RF06 the measured $F_{\text{BB,mea}}$ and $\alpha_{\text{BB,mea}}$ are systematically higher compared to ecRad (5%) and libRadtran (15%). Accordingly, the SMART PDFs are shifted towards higher values compared to the simulations, whereby the shapes are matching. The peaks of the PDFs are dominated by cloud-free model columns and columns with f_{tot} below 10 %.

Exclusion of model-columns with f_{tot} below 20 % allows to identify cloud samples, which are present in the IFS AD and the observations at the same time and location. In addition, the cloud-only radiative effect becomes more clear. Resulting PDFs show an overestimation in observed $\alpha_{\text{BB,mea}}$ by $\alpha_{\text{BB,eR}}$ with +12 % and an underestimation by $\alpha_{\text{BB,eR}}$ with -22 %. A potential factor for the bias in α is the overestimation of $f_{\text{tot,eR}}$ by ecRad due to the applied cloud overlap assumption. Additionally, a lack of LWC / LWP in the IFS AD compared to MODIS retrieved LWP_{mod} is found. Similar

underestimation of F and α by the libRadtran benchmark simulations support the inappropriate representation of small scale heterogeneous clouds in the IFS AD by missing LWC / LWP .

Spectral analysis of simulated F^\uparrow and α shows good agreement with the observations within the measurement uncertainty range and indicates for an appropriate optical representation of liquid water clouds in the ecRad radiation scheme and libRadtran.

By separating absolute differences between F_{eR}^\uparrow , F_{mea}^\uparrow , and among the models for f and LWP , allows to categorize clouds with respect coverage and water content. The resulting classification supports that most of the differences in simulated and observed F^\uparrow stem from an overestimation of f , whereby the LWP in the IFS AD is lower compared to the observations.

Perspectives

In course of this work two exemplary flights from NARVAL-II and NAWDEX are analyzed, not covering the natural variability of clouds and observation conditions, e.g., solar zenith angle or different seasons of the year. Therefore, extended simulations and additional analysis of other flights is advised, increasing the statistical significance of the presented conclusions and isolating systematic model errors more precisely, e.g., with respect to total water path and cloud fraction.

Expanding the comparison from the solar wavelength range (266 - 2050 nm) to the micrometer wavelength range (22.24 - 183 GHz), by using forward simulations of radar reflectivity profiles on basis of the Passive and Active Microwave TRAnsfer model (PAMTRA), potentially enables to validate the entire atmospheric column of the IFS AD below the aircraft, not being limited to scattered radiation from cloud top.

Further on, it is planed to evaluate the recently developed IFS ice optics scheme "Yi" basing on Yi et al. (2013), which considers for aggregated ice crystals and ice crystal surface roughness.

7 Appendix

7.1 Setup up of Radiation Scheme / Configuration of Namelist

For the initialization and configuration of Numerical Weather Prediction and Global Climate Models, namelists are used. These files list variables and parameters, which can be selected for each model run. ecRad requires such a namelist file, allowing to adjust the model to the specific setup requirements with a single file instead of modifying the input data for each model run separately. If a parameter is specified in the namelist it will overwrite the default values.

To conduct representative simulations with respect to the IFS forecast, variables and parameters in the namelist are set to the IFS operational values. In Tab. 7.1 an overview of the parameters, the IFS default settings, and the selected values for the simulations are presented.

Table 7.1: Namelist parameters used to control the simulations of ecRad. Key words, values, and description are given in the table. IFS default values are print in bold. If the setup differs from the IFS operational value then the selected parameter is highlights in bold and underlined. Table follows Hogan (2018).

<i>General</i>		
directory_name	.	Directory containing NetCDF configuration files
do_sw	true	Compute shortwave fluxes
do_lw	true	Compute longwave fluxes
do_sw_direct	true	Do direct shortwave fluxes
do_clear	true	Compute clear-sky fluxes
<i>Override input variables</i>		
solar_irradiance_override	1360.0	Override solar irradiance (W m^{-2})
<i>Gas and aerosol optics</i>		
gas model name	RRTMG-IFS, Monochromatic	
use aerosols	false	Do we represent aerosols
do_lw_aerosol_scattering	true	Do longwave aerosol scattering
n_aerosol_types		Number of aerosol types
i_aerosol_type_map		-
<i>Monochromatic scheme</i>		
mono_lw_wavelength	-1.0	Wavelength of longwave radiation, or if negative, a broadband calculation will be performed
mono_lw_totalOd	0.0	Zenith longwave optical depth of clear-sky atmosphere
mono_sw_totalOd	0.0	Zenith shortwave optical depth of clear-sky atmosphere
<i>Cloud optics</i>		
liquid_model_name	SOCRATES , Slingo, Monochromatic	Liquid optics model, including the scheme in the SOCRATES radiation scheme and the older scheme of Slingo (1989)
ice_model_name	Fu-IFS , Baran2016, Yi, Monochromatic	Ice optics model, including the schemes of Fu (1996), Fu et al. (1998), Baran et al. (2016) and Yi et al. (2013)
do_lw_cloud_scattering	true	Do longwave cloud scattering

do_fu_lw_ice_optics_bug	false	Reproduce bug in McRad implementation of Fu ice optics
<hr/>		
<i>Solver</i>		
sw_solver_name	Homogeneous, McICA , Tripleclouds, SPARTACUS	Shortwave solver
lw_solver_name	SPARTACUS	Longwave solver
overlap_scheme_name	Exp-Exp , Exp-Ran , Max-Ran	Cloud overlap scheme
use_beta_overlap	false	Use Shonk et al. (2010) 'b' overlap parameter definition, rather than default 'a'?
cloud_inhom_decorr_scaling	0.5	Ratio of overlap decorrelation lengths for cloud heterogenities and boundaries
cloud_fraction_threshold	10^{-6}	Ignore clouds with fraction below this
cloud_mixing_ratio_threshold	10^{-9}	Ignore clouds with total mixing ratio below this
cloud_pdf_shape_name	Gamma , Lognormal	Shape of cloud water PDF
cloud_pdf_override_file_name	-	Name of NetCDF file of alternative cloud PDF look-up table
do_sw_delta_scaling_with_gases	false	Apply delta-Eddington scaling to particle-gas mixture, rather than particles only
<hr/>		
<i>SPARTACUS solver</i>		
do_3d_effects	true	Represent 3D effects when SPARTACUS solver selected
n_regions	2, 3	Number of regions, where one is clear sky and one or two are cloud (the Tripleclouds solver always
do_lw_side_emissivity	true	Represent effective emissivity of the side of clouds (Schäfer et al., 2016)
sw encroachment name	Minimum, Computed , Maximum	Encroachment (or 'entrapment') model (note that the behavior in ecRad version 1.0.1 was 'Maximum' encroachment)
do_3d_lw_multilayer_effects	false	Maximum encroachment for longwave radiation
max_3d_transfer_rate	10.0	Maximum rate of lateral exchange between regions in one layer, for stability of matrix exponential (where the default means that as little as e^{-10} of the radiation could remain in a region)
max_gas_od_3d	8.0	3D effects ignored for spectral intervals where gas optical depth of a layer exceeds this, for stability
max_cloud_od	18.0	Maximum in-cloud optical depth, for stability
use_expm_everywhere	false	Use matrix-exponential method even when 3D effects not represented

clear_to_thick_fraction	0.0	Fraction of cloud edge interfacing directly to the most optically thick cloudy region
overhead_sun_factor	0.0	Minimum tan-squared of solar zenith angle to allow some 'direct' radiation from overhead sun to pass through cloud sides (0.06 used by Hogan et al., 2016)
<hr/> <i>Diagnostics</i>		
iverbosesetup	0, 1, 2, 3, 4, 5	Verbosity in setup, where 1=warning, 2=info, 3=progress, 4=detailed, 5=debug
iverbose		Verbosity in execution
do_save_spectral_flux	false, <u>true</u>	Save flux profiles in each band
do_save_gpoint_flux	false	Save flux profiles in each g-point
do_surface_sw_spectral_flux	true	Save surface shortwave fluxes in each band for subsequent diagnostics
do_lw_derivatives	false	Compute derivatives for Hogan and Bozzo (2015) approximate updates
do_save_radiative_properties	false, <u>true</u>	Write intermediate NetCDF file(s) of properties sent to solver (radiative_properties*.nc)

In the operational configuration of IFS the McICA solver is selected for the shortwave and longwave calculations. This solver does not provide spectral upward and downward irradiances at all model levels. Spectral resolving $F^{\uparrow\downarrow}$ are available at the TOA and the surface of the model only, but vertical profiles are needed to extract $F^{\uparrow\downarrow}$ for any given aircraft altitude. The spectral resolution is required to match the wavelength coverage of ecRad and SMART. This necessitates to select the SPARTACUS solver. SPARTACUS can only be run together with the "EXP-RAN" cloud overlap assumption deviating from the operational IFS namelist configuration.

Further namelist changes are applied for `do_save_spectral_flux` to obtain $F^{\uparrow\downarrow}$ for the spectral bands of ecRad. The optional radiative properties are stored by setting `do_save_radiative_properties` to 'true'. By switching `do_3d_effects` to 'false' 3D effects on sub-grid scale are not parameterized and the SPARTACUS solver works on basis of the Tripleclouds solver, where cloud heterogeneity is characterized by the fractional standard deviation (FSD) of the water content. FSD is obtained by dividing the standard deviation by the mean value of adjacent cloud layers. The use `aerosols` parameter was set to 'false' because no aerosol database was available.

7.2 Set-up of libRadtran

To set-up the libRadtran simulations an input file is mandatory, which specifies the available options and controls the simulations. In course of this thesis two different set-up configurations are used for the simulations. In the first version the libRadtran simulations are set-up to match the operational IFS configuration as close as possible, including the ice crystal parameterization after Fu (1996). In the second version the more sophisticated ice crystal parameterization following Baum et al. (2005a) and Baum et al. (2005b) is used to show potential differences in simulated spectral and broadband F , which potentially occur by using higher resolving radiative transfer models (RTM) like libRadtran in comparison to simplified parameterizations currently used in IFS. Analog to the ecRad simulations the input files for libRadtran, are provided for a temporal resolution of two seconds.

To calculate the radiative transfer equations, the solver `fdisort2` after Stamnes et al. (2000) with 16 streams is used. The simulations are performed for a wavelength range from 250 to 2500 nm (set with `wavelength`), covering the same wavelength range as the SMART measurements, with a spectral resolution of 1 nm. The command `atmosphere_file` loads the atmosphere file which contains the IFS analysis data for the temperature, pressure, and humidity profiles while `radiosonde` adds a radiosonde measurement of 12 UTC of the analyzed day. According to the position of HALO,

`time`, `longitude`, `latitude`, and `altitude` specify the day, time, location, and height for which the simulation is performed. From these parameters the SZA is determined automatically and an extra-terrestrial solar flux after Kurucz (1992) defined by `source solar` is utilized. Vertical profiles of cloud fraction, the liquid water content, and ice water content are provided by additional files, which are called by `cloud_fraction_file`, `wc_file`, and `ic_file`, respectively. These files are derived from the IFS AD, too. To consider the operational COA of the IFS the `cloud_overlap` was set to the 'rand' option. For liquid water clouds pre-calculated Mie tables are applied by setting `wc_properties mie interpolate` and are interpolated to fit the selected spectral resolution of 1 nm. Simulations with libRadtran are performed for two different ice crystal shape parameterizations. If `ic_habit` is not specified and `ic_fu reff_def` is set to 'on', the default option with the parameterization and definition of the effective radius after Fu (1996) and Fu et al. (1998b) is used, corresponding to the IFS simulations. To investigate potential differences between the simplified Fu and a spectrally higher resolving ice crystal shape parameterizations, a second simulation set with `ic_habit` using 'ghm' is performed. This option represents a mixture of different ice crystal habits calculated after Baum et al. (2005a,b) by setting `ic_properties` to 'baum_v36'. The Baum V3.6 parameterization includes complete scattering phase functions and does not utilize approximations like the Henyey-Greenstein phase function. For consistency the 'ghm' simulations are performed with `ic_fu reff_def` switched to 'on' because $r_{\text{eff,ice}}$ is determined with this definition by the IFS routines from the model data.

Using the `verbose` option in libRadtran allows to obtain a detailed report of the performed RTS and to check for the expected behavior of the RT solver. From the resulting verbose files the total cloud optical thickness τ is extracted.


```

! Configuration namelists for ECRAD radiation code
!
! The following namelist controls the behaviour of the driver routine,
! including parallelization options and overriding numbers read from
! the NetCDF input file
!
! This version matches ! ! ! M O S T L Y ! ! ! the expected configuration of
ECMWF IFS Cycle 43R3
! for differences please see the explanations in the thesis Sec. 4.2.7 and
according Table 4.5
&radiation_driver
do_parallel          = true,      ! Use OpenMP parallelization?
nblocksize           = 8,         ! Number of columns to process per thread
sw_albedo             = 0.08,     ! Override shortwave albedo

! Verbosity level: 0=none, 1=warning, 2=info, 3=progress, 4=detailed, 5=debug
iverbose             = 5,

solar_irradiance_override = 1360.0, ! Total solar irradiance (W m-2)

istartcol             = 0,        ! Use full range of columns by default
iendcol               = 0,
nrepeat               = 1,
/
!
! The following namelist controls the behaviour of the ECRAD
! radiation code
!
&radiation
do_sw                 = true,      ! Compute shortwave fluxes?
do_lw                 = false,     ! Compute longwave fluxes?
do_sw_direct          = true,     ! Compute direct downward shortwave
fluxes?
do_clear              = true,      ! Compute clear-sky fluxes?
directory_name        = "/projekt3/ag_mwend/ECMWF_ECRAD/src/ecrad-
1.0.1/data/",      ! Location of configuration files
liquid_model_name     = "SOCRATES", ! Liquid droplet scattering model
ice_model_name        = "Fu-IFS",  ! Ice particle scattering model
!ice_model_name       = "Baran2017", ! Ice particle scattering model
sw_solver_name        = "SPARTACUS",
lw_solver_name        = "SPARTACUS",
overlap_scheme_name   = "Exp-Ran", ! Exp-Ran, Max-Ran or Exp-Exp
cloud_fraction_threshold = 0.001e-3, !
do_lw_aerosol_scattering = false,   ! Aerosols scatter in the longwave?
do_lw_cloud_scattering = false,     ! Clouds scatter in the longwave?
cloud_inhom_decorrr_scaling = 0.5, ! Ratio of overlap decorrr len of
inhomogeneities to boundaries
use_beta_overlap      = false,
do_save_radiative_properties = true, ! Save raw radiation properties in
radiative_properties.nc?
do_3d_effects         = false,      ! Represent 3D effects?
! Verbosity level: 0=none, 1=warning, 2=info, 3=progress, 4=detailed, 5=debug
! Separate verbosity specified for setup and ordinary execution
iverbose              = 5,
iverbosesetup         = 5,
use_aerosols          = false,      ! Include aerosols in radiation
calculations?
do_save_spectral_flux = true,       ! Save spectral fluxes in output file?
do_save_gpoint_flux   = false,     ! Save fluxes per g-point in output
file?
do_lw_derivatives     = true,      ! Hogan-Bozzo style derivatives for
approx updates
gas_model_name        = "RRTMG-IFS", ! Gas model
do_surface_sw_spectral_flux = true,

```

```

do_fu_lw_ice_optics_bug = true,
do_sw_delta_scaling_with_gases = false,
!
! 12 IFS aerosol classes stored in aerosol_ifs_rrtm.nc: 1-3 Sea salt,
! 4-6 Boucher desert dust, 7 hydrophilic organics, 8 hydrophobic
! organics, 9&10 hydrophobic black carbon, 11 ammonium sulphate, 12
! inactive SO2
!n_aerosol_types          = 12,                ! Aerosols are deactivated if this is
zero
!
! Indices to the aerosol optical properties in aerosol_ifs_rrtm.nc,
! for each class, where negative numbers index hydrophilic aerosol
! types and positive numbers index hydrophobic aerosol types
i_aerosol_type_map = -1, -2, -3, 1, 2, 3, -4, 10, 11, 11, -5, 14,
! Tegen types are rather more simple
!i_aerosol_type_map = 2, 2, 2, 3, 3, 3, 1, 1, 4, 4, 6, 5,
/

```

/

```
#####  
#libRadtran example inputfile##  
#####
```

```
# Location of internal libRadtran data  
data_files_path /opt/libradtran/2.0.2/share/libRadtran/data  
# Radiative transfer solver  
rte_solver fdisort2  
# Number of streams  
number_of_streams 16  
# Location of atmospheric profile data  
atmosphere_file  
/projekt1/ag_mwend/Data/NAWDEX/13_lib_ifs_sim/cloudy_atmosphere/atmos_56038.4_so  
d.dat4  
# Location of radiosonde data  
radiosonde  
/projekt1/ag_mwend/Data/NAWDEX/soundings/RS_for_libRadtran/keflavik/RS_NAWDEX_20  
160926a_12.dat H2O RH  
# Date and time for which the simulation is run  
time 2016 09 26 15 33 58  
# Selected surface albedo from parameterization  
albedo 0.08  
# Set latitude  
latitude N 58.0658  
# Set longitude  
longitude W 25.7954  
# Height of surface  
altitude 0  
# Output hight altitude above sea level (km)  
zout 8.55241  
# Specified wavelength range  
wavelength 250 2500  
# Extraterr. solar flux  
source solar  
/opt/libradtran/2.0.2/share/libRadtran/data/solar_flux/kurudz_1.0nm.dat  
# Required output: wavelength; solar zenith angle; Fdn,dir; Fdn,dif; Fup;  
Iup  
output_user lambda sza edir edn eup uu  
# Assumed ozon concentration  
mol_modify 03 325 DU  
# Location of cloud fraction file  
cloud_fraction_file  
/projekt1/ag_mwend/Data/NAWDEX/13_lib_ifs_sim/cloudy_atmosphere/cf_file_56038.4_  
sod.dat  
  
cloud_overlap rand #would fit to exp-ran of or max-ran from ecmwf #turn off  
cloud_overlap for ECMWF like clouds  
# Location of liquid water cloud file  
wc_file 1D  
/projekt1/ag_mwend/Data/NAWDEX/13_lib_ifs_sim/cloudy_atmosphere/wc_cloud_layer_5  
6038.4_sod.dat  
# Location of ice water cloud file  
ic_file 1D  
/projekt1/ag_mwend/Data/NAWDEX/13_lib_ifs_sim/cloudy_atmosphere/ic_cloud_layer_5  
6038.4_sod.dat  
# Use Mie for water droplets and interpolate the look-up-table  
wc_properties mie interpolate  
# Use Fu parameterization for ice crystals and interpolate the look-up-  
table  
ic_properties fu interpolate  
# Use the Fu definition of ice crystal size  
ic_fu reff_def on  
  
#end of file
```

```

, ***** liquid effective radius *****
, *
, * Calculate effective radius of liquid clouds
, * ONLY over ocean
, *
, *
, *** REQUIRED INPUT ***
, *
, * PPRESSURE      Pressure
, * PTEMPERATURE   Temperature
, * PCLLOUD_FRAC   Cloud Fraction
, * PQ_LIQ         specific liquid humidity
, * PQ_RAIN        specific rain humidity
, *
, *
, *** RETURN VALUE ***
, *
, * PRE_UM         Liquid water effective radius in mum
, *
,

```

```

function
liquid_effective_radius,PPRESSURE,PTEMPERATURE,PCLLOUD_FRAC,PQ_LIQ,PQ_RAIN

;verbose = 0          ;for error search: 0 = no output, 1 = detailed output of
parameters

;constants
PP_MIN_RE_UM = 4D      ;min radius
PP_MAX_RE_UM = 30D     ;max radius
PCCN_SEA = 50D          ; my personal assumption!!! better
estimation??????
ZCCN = PCCN_SEA
ZSPECTRAL_DISPERSION = 0.77D
R_DRY = 287D           ; J kg-1 K-1
RPI=3.1415962D
;IFS security parameters
REPSC = 1.E-04
REPSCA = 1.E-10
REPSCO = 1.E-12
REPSCQ = 1.E-12
REP SCT = 1.E-12
REPSCW = 1.E-12
REPL OG = 1.E-12

ZNTOT_CM3 = -1.15D*10E-3 *ZCCN*ZCCN+0.963D *ZCCN+5.3D
ZRATIO=(0.222D/ZSPECTRAL_DISPERSION)^(0.333D)

if ((PCLLOUD_FRAC ge 0.001) and (PQ_LIQ+PQ_RAIN gt 0.)) then begin ;Consider
only cloudy regions
    ZAIR_DENSITY_GM3 = 1000D*PPRESSURE/(R_DRY*PTEMPERATURE)
    ZLWC_GM3 = ZAIR_DENSITY_GM3*PQ_LIQ/PCLLOUD_FRAC          ;In-cloud mean
water contents found by dividing by cloud fraction
    ZRWC_GM3 = ZAIR_DENSITY_GM3*PQ_RAIN/PCLLOUD_FRAC

    if (ZLWC_GM3 gt REPSCW) then begin
        ZRAIN_RATIO = ZRWC_GM3 / ZLWC_GM3
        ZWOOD_FACTOR from Wood_et_al_2000b: Parameterization of the effect
of drizzle upon the droplet effective radius in stratocumulus clouds (Eq. 19)

        ZWOOD_FACTOR = ((1D +ZRAIN_RATIO)^(0.666D)) / (1D +0.2D * ZRATIO *
ZRAIN_RATIO)
    endif else begin
        ZWOOD_FACTOR = 1D
    endelse

```

```

ZRE_CUBED = (3D *(ZLWC_GM3 + ZRWC_GM3)) / (4D * RPI * ZNTOT_CM3 *
ZSPECTRAL_DISPERSION)

if (ZRE_CUBED gt REPLOG) then begin
  PRE_UM = ZWOOD_FACTOR*100D *exp(0.333D*alog(ZRE_CUBED))
  if (PRE_UM lt PP_MIN_RE_UM) then PRE_UM = PP_MIN_RE_UM ;make sure
calculated radius is within borders
  if (PRE_UM gt PP_MAX_RE_UM) then PRE_UM = PP_MAX_RE_UM
endif else begin
  PRE_UM = PP_MIN_RE_UM
endelse
endif else begin
  PRE_UM = PP_MIN_RE_UM ;when cloud fraction or liquid+rain water content
too low to consider this as a cloud
endelse
return,PRE_UM
end

```

```

, ***** ice effective radius *****
, *
, *
, * Calculate effective radius of ice clouds
, *
, * Ice effective radius = f(T,IWC) from Sun and Rikus (1999), revised
, * by Sun (2001)
, * Default effective radius is computed from an effective diameter of
, * 80 microns; note that multiplying by re2de actually converts from
, * effective diameter to effective radius.
, *
, *
, *** REQUIRED INPUT ***
, *
, * PPRESSURE      Pressure
, * PTEMPERATURE   Temperature
, * PCLOUD_FRAC    Cloud Fraction
, * PQ_ICE         specific liquid humidity
, * PQ_SNOW        specific rain humidity
, * PLAT           Latitude
, *
, *
, *** RETURN VALUE ***
, *
, * PRE_UM         ice effective radius in mum
, *
,

```

```

function
ice_effective_radius,PPRESSURE,PTEMPERATURE,PCLOUD_FRAC,PQ_ICE,PQ_SNOW,PLAT

;constants
RRE2DE = 0.64952D ; from suecrad.f90
;RRE2DE = 0.7698D ; from suecrad.f90
RMINICE = 60D      ; min ice radius
RTT = 273.15D      ; temperature of fusion of water
RPI = 3.1415962D
R_DRY = 287D       ; J kg-1 K-1
test_value = 129.80D

ZDEFAULT_RE_UM = 80D * RRE2DE
ZMIN_DIAMETER_UM = 20D +(RMINICE-20D)*cos((PLAT*RPI/180D))  ;! Ice effective
radius varies with latitude, smaller at poles

if ((PCLOUD_FRAC gt 0.001) and (PQ_ICE+PQ_SNOW gt 0.)) then begin ;Consider
only cloudy regions
    ZAIR_DENSITY_GM3 = 1000D*PPRESSURE/(R_DRY*PTEMPERATURE)
    ZIWC_INCLOUD_GM3 = ZAIR_DENSITY_GM3 * (PQ_ICE + PQ_SNOW) / PCLOUD_FRAC
    ZTEMPERATURE_C = PTEMPERATURE - RTT
; ! Sun, 2001 (corrected from Sun & Rikus, 1999)
    ZAIWC = 45.8966D * ZIWC_INCLOUD_GM3^(0.2214D)
    ZBIWC = 0.7957D * ZIWC_INCLOUD_GM3^(0.2535D)
    ZDIAMETER_UM = (1.2351D + 0.0105D * ZTEMPERATURE_C) * (ZAIWC +
ZBIWC*(PTEMPERATURE - 83.15D))
    ZDIAMETER_UM = MIN([MAX([ZDIAMETER_UM, ZMIN_DIAMETER_UM]),test_value])
    PRE_UM = ZDIAMETER_UM * RRE2DE
endif else begin
PRE_UM = ZDEFAULT_RE_UM
endelse

return,PRE_UM
end

```

Bibliography

- Ahlgrim, M. and Forbes, R.: Improving the Representation of Low Clouds and Drizzle in the ECMWF Model Based on ARM Observations from the Azores, *Mon. Weather Rev.*, 142, 668–685, 2014.
- Albrecht, B. A.: Fractional cloudiness and cloud-top entrainment instability, *J. Atmos. Sci.*, 48, 1519–1525, 1991.
- Baran, A., Brown, S., Foot, J., and Mitchell, D.: Retrieval of tropical cirrus thermal optical depth, crystal size, and shape using a dual-view instrument at $3.7\ \mu\text{m}$ and $10.8\ \mu\text{m}$, *J. Atmos. Sci.*, 56, 92–110, 1999.
- Baran, A. J.: On the scattering and absorption properties of cirrus cloud, *J. Quant. Spectrosc. Ra.*, 89, 17–36, 2004.
- Baran, A. J.: From the single-scattering properties of ice crystals to climate prediction: A way forward, *Atmos. Res.*, 112, 45–69, 2012.
- Barker, H. W., Cole, J. N. S., Morcrette, J.-J., Pincus, R., Räisänen, P., von Salzen, K., and Vaillancourt, P. A.: The Monte Carlo Independent Column Approximation: an assessment using several global atmospheric models, *Q. J. Roy. Meteor. Society*, 134, 1463–1478, 2008.
- Baum, B. A., Heymsfield, A. J., Yang, P., and Bedka, S. T.: Bulk scattering properties for the remote sensing of ice clouds. Part I: Microphysical data and models, *J. Appl. Meteor.*, 44, 1885–1895, 2005a.
- Baum, B. A., Yang, P., Heymsfield, A. J., Platnick, S., King, M. D., Hu, Y. X., and Bedka, S. T.: Bulk scattering properties for the remote sensing of ice clouds. Part II: Narrowband models, *J. Appl. Meteor.*, 44, 1896–1911, 2005b.
- Baum, B. A., Yang, P., Nasiri, S., Heidinger, A. K., Heymsfield, A., and Li, J.: Bulk scattering properties for the remote sensing of ice clouds. Part III: High-resolution spectral models from 100 to $3250\ \text{cm}^{-1}$, *J. Appl. Meteor.*, 46, 423–434, 2007.
- Bierwirth, E., Wendisch, M., Ehrlich, A., Heese, B., Tesche, M., Althausen, D., Schladitz, A., Müller, D., Otto, S., Trautmann, T., Dinter, T., von Hoyningen-Huene, W., and Kahn, R.: Spectral surface albedo over Morocco and its impact on the radiative forcing of Saharan dust, *Tellus*, 61B, 252–269, 2009.
- Bohren, C. F. and Huffman, D. R.: *Absorption and Scattering of Light by Small Particles*, Wiley-Interscience, New York, 1998.
- Bony, S. and Dufresne, J.-L.: Marine boundary layer clouds at the heart of tropical cloud feedback uncertainties in climate models, *Geophys. Res. Lett.*, 32, 2005.
- Bony, S., Stevens, B., Frierson, D. M. W., Jakob, C., Kageyama, M., Pincus, R., Shepherd, T. G., Sherwood, S. C., Siebesma, A. P., Sobel, A. H., Watanabe, M., and Webb, M. J.: Clouds, circulation and climate sensitivity, *Nat. Geosci.*, 8, 261–268, 2015.
- Bony, S., Stevens, B., Ament, F., Bigorre, S., Chazette, P., Crewell, S., Delanoë, J., Emanuel, K., Farrell, D., Flamant, C., Gross, S., Hirsch, L., Karstensen, J., Mayer, B., Nuijens, L., Ruppert, J. H., Sandu, I., Siebesma, P., Speich, S., Szczap, F., Totems, J., Vogel, R., Wendisch, M., and Wirth, M.: EUREC4A: A Field Campaign to Elucidate the Couplings Between Clouds, Convection and Circulation, *Surv. Geophys.*, 38, 1529–1568, <https://doi.org/10.1007/s10712-017-9428-0>, 2017.

- Bozzo, A., Pincus, R., Sandu, I., and Morcrette, J.-J.: Impact of a spectral sampling technique for radiation on ECMWF weather forecasts, *J. Adv. Model. Earth Sy.*, 6, 1288–1300, 2014.
- Brenguier, J.-L., Pawlowska, H., Schüller, L., Preusker, R., Fischer, J., and Fouquart, Y.: Radiative properties of boundary layer clouds: Droplet effective radius versus number concentration, *J. Atmos. Sci.*, 57, 803–821, 2000.
- Buehler, S. A., John, V. A., Kottayil, A., Milz, M., and Eriksson: Efficient radiative transfer simulations for a broadband infrared radiometer - Combining a weighted mean of representative frequencies approach with frequency selection by simulated annealing, *J. Quant. Spectrosc. Ra.*, 111, 602 – 615, 2010.
- Cahalan, R.: Bounded cascade clouds: albedo and effective thickness, *Nonlin. Proc. Geophys.*, 1, 156–167, 1994.
- Cahalan, R. and Joseph, J.: Fractal statistics of cloud fields, *Mon. Wea. Rev.*, 117, 261–272, 1989.
- Cahalan, R., Silberstein, D., and Snider, J.: Liquid water path and plane-parallel albedo bias during ASTEX, *J. Atmos. Sci.*, 52, 3002–3012, 1995.
- Chandrasekhar, S.: Radiative Transfer, Oxford University Press, London, UK, 1950.
- Chen, T., Rossow, W., and Zhang, Y.: Radiative effects of cloud-type variations, *J. Climate*, 13, 264–286, 2000.
- Chertock, B., Fairall, C. W., and White, A. B.: Surface-based measurements and satellite retrievals of broken cloud properties in the equatorial Pacific, *J. Geophys. Res. Atmos.*, 98, 18 489–18 500, 1993.
- Delanoe, J., Protat, A., Jourdan, O., Pelon, J., Papazzoni, M., Dupuy, R., Gayet, J.-F., and Jouan, C.: Comparison of airborne in situ, airborne Radar-Lidar, and spaceborne Radar-Lidar retrievals of polar ice cloud properties sampled during the POLARCAT campaign, *J. Atmos. Oceanic Technol.*, 30, 57–73, 2013.
- Eastman, R., Warren, S. G., and Hahn, C. J.: Variations in cloud cover and cloud types over the ocean from surface observations, 1954–2008, *J. Climate*, 24, 5914–5934, 2011.
- ECMWF: Part III: Dynamics and Numerical Procedures, no. 3 in IFS Documentation, ECMWF, <https://www.ecmwf.int/node/16647>, 2016a.
- ECMWF: Part IV: Physical Processes, no. 4 in IFS Documentation, ECMWF, <https://www.ecmwf.int/node/16648>, 2016b.
- Edwards, J. M. and Slingo, A.: Studies with a flexible new radiation code. I: Choosing a configuration for a large-scale model, *Q. J. Roy. Meteor. Soc.*, 122, 689–719, 1996.
- Ehrlich, A.: The impact of ice crystals on radiative forcing and remote sensing of Arctic boundary-layer mixed-phase clouds, Ph.D. thesis, Johannes Gutenberg University Mainz, Germany, 2009.
- Ehrlich, A., Wendisch, M., Bierwirth, E., Gayet, J.-F., Mioche, G., Lampert, A., and Mayer, B.: Evidence of ice crystals at cloud top of Arctic boundary-layer mixed-phase clouds derived from airborne remote sensing, *Atmos. Chem. Phys.*, 9, 9401–9416, 2009.
- Elsaesser, G. S., O'Dell, C. W., Lebsock, M. D., Bennartz, R., Greenwald, T. J., and Wentz, F. J.: The multisensor advanced climatology of liquid water path (MAC-LWP), *J. Climate*, 30, 10 193–10 210, 2017.
- Emde, C., Buras-Schnell, R., Kylling, A., Mayer, B., Gasteiger, J., Hamann, U., Kylling, J., Richter, B., Pause, C., Dowling, T., and Bugliaro, L.: The libRadtran software package for radiative transfer calculations (version 2.0.1), *Geosci. Model Dev.*, 9, 1647–1672, 2016.
- Espy, J. P.: Essays on meteorology. No. IV, *J. Franklin Inst.*, 22, 239 – 246, 1836.

- Forbes, R. M.: Future Directions for the Parametrization of Cloud and Precipitation Microphysics, presentation, 2010.
- Forbes, R. M. and Ahlgrimm, M.: On the Representation of High-Latitude Boundary Layer Mixed-Phase Cloud in the ECMWF Global Model, *Mon. Weat. Rev.*, 142, 3425–3445, 2014.
- Fu, Q.: An accurate parameterization of the solar radiative properties of cirrus clouds in climate models, *J. Climate*, 9, 2058–2082, 1996.
- Fu, Q., Lesins, G., Higgins, J., Charlock, T., Chylek, P., and Michalsky, J.: Broadband water vapour absorption of solar radiation tested using ARM data, *Geophys. Res. Lett.*, 25, 1169–1172, 1998a.
- Fu, Q., Yang, P., and Sun, W.: An accurate parameterization of the infrared radiative properties of cirrus clouds in climate models, *J. Climate*, 11, 2223–2237, 1998b.
- Gasteiger, J., Emde, C., Mayer, B., Buras, R., Buehler, S., and Lemke, O.: Representative wavelengths absorption parameterization applied to satellite channels and spectral bands, *J. Quant. Spectrosc. Radiat. Transfer*, 148, 99–115, 2014.
- Geer, A. J., Ahlgrimm, M., Bechtold, P., Bonavita, M., Bormann, N., English, S., Fielding, M., Forbes, R., Hogan, R., Hólm, E., Janiskova, M., Lonitz, K., Lopez, P., Matricardi, M., Sandu, I., and Weston, P.: Assimilating observations sensitive to cloud and precipitation, Tech. Rep. 815, ECMWF, <https://www.ecmwf.int/node/17718>, 2017.
- Goody, R., West, R., Chen, L., and Crisp, D.: The correlated-k method for radiation calculations in non-homogeneous atmospheres, *J. Quant. Spectrosc. Radiat. Transfer*, 42, 539–550, 1989.
- Grenfell, T. C. and Warren, S. G.: Representation of a nonspherical ice particle by a collection of independent spheres for scattering and absorption of radiation, *J. Geophys. Res.*, 104, 31.697–31.709, 1999.
- Grosvenor, D. P., Sourdeval, O., Zuidema, P., Ackerman, A., Alexandrov, M. D., Bennartz, R., Boers, R., Cairns, B., Chiu, J. C., Christensen, M., Deneke, H. M., Diamond, M. S., Feingold, G., Fridlind, A., Hünerbein, A., Knist, C. L., Kollias, P., Marshak, A., McCoy, D., Merk, D., Painemal, D., Rausch, J., Rosenfeld, D., Russchenberg, H., Seifert, P., Sinclair, K., Stier, P., van Diedenoven, B., Wendisch, M., Werner, F., Wood, R., Zhang, Z., and Quaas, J.: Remote sensing of droplet number concentration in warm clouds: A review of the current state of knowledge and perspectives, *Rev. Geophys.*, 56, 409–453, 2018.
- Hansen, J. and Travis, L.: Light scattering in planetary atmospheres, *Space Sci. Rev.*, 16, 527–610, 1974.
- Hersbach, H., de Rosnay, P., Bell, B., Schepers, D., Simmons, A., Soci, C., Abdalla, S., Alonso-Balmaseda, M., Balsamo, G., Bechtold, P., Berrisford, P., Bidlot, J.-R., de Boissésón, E., Bonavita, M., Browne, P., Buizza, R., Dahlgren, P., Dee, D., Dragani, R., Diamantakis, M., Flemming, J., Forbes, R., Geer, A. J., Haiden, T., Hólm, E., Haimberger, L., Hogan, R., Horányi, A., Janiskova, M., Laloyaux, P., Lopez, P., Muñoz-Sabater, J., Peubey, C., Radu, R., Richardson, D., Thépaut, J.-N., Vitart, F., Yang, X., Zsótér, E., and Zuo, H.: Operational global reanalysis: progress, future directions and synergies with NWP, Tech. rep., European Centre for Medium-Range Weather Forecasts, 2018.
- Herwehe, J. A., Alapaty, K., Spero, T. L., and Nolte, C. G.: Increasing the credibility of regional climate simulations by introducing subgrid-scale cloud-radiation interactions, *J. Geophys. Res. Atmos.*, 119, 5317–5330, 2014.
- Hogan, R., Illingworth, A., and Sauvageot, H.: Measuring crystal size in cirrus using 35- and 94-GHz radars, *J. Atmos. Oceanic Technol.*, 17, 27–37, 2000.
- Hogan, R. J.: ecRAD radiation scheme: User Guide, Tech. rep., European Center for Medium Range Forecast, 2018.

- Hogan, R. J. and Bozzo, A.: A Flexible and Efficient Radiation Scheme for the ECMWF Model, *J. Adv. Model Earth Sy.*, 10, 2018.
- Hogan, R. J., Schäfer, S. A. K., Klinger, C., Chiu, J. C., and Mayer, B.: Representing 3-D cloud radiation effects in two-stream schemes: 2. Matrix formulation and broadband evaluation, *J. Geophys. Res. Atmos.*, 121, 8583–8599, 2016.
- Hogan, R. J., Ahlgrimm, M., Balsamo, G., Beljaars, A., Berrisford, P., Bozzo, A., Di Giuseppe, A., Forbes, F. M., Haiden, T., Lang, S., Mayer, M., Polichtchouk, I., Sandu, I., Vitart, F., and Wedi, N.: Radiation in numerical weather prediction, Technical Memorandum 816, European Centre for Medium-Range Weather Forecast, Shinfield Park, Reading, RG2 9AX, England, 2017.
- Jäkel, E., Walther, J., and Wendisch, M.: Thermodynamic phase retrieval of convective clouds: Impact of sensor viewing geometry and vertical distribution of cloud properties, *Atmos. Meas. Tech.*, 6, 539–547, 2013.
- Jensen, E. J., Kinne, S., and Toon, O. B.: Tropical Cirrus Cloud Radiative Forcing - Sensitivity Studies, *Geophys. Res. Lett.*, 21, 2023–2026, 1994.
- Joseph, J. H., Wiscombe, W. J., and Weinman, J. A.: The Delta-Eddington approximation for radiative flux-transfer, *J. Atmos. Sci.*, 33, 2.452–2.459, 1976.
- Key, J. R., Yang, P., Baum, B. A., and Nasiri, S. L.: Parameterization of shortwave ice cloud optical properties for various particle habits, *J. Geophys. Res.*, 107, Art. No. 4181, 2002.
- Khain, A. P., Beheng, K. D., Heymsfield, A., Korolev, A., Krichak, S. O., Levin, Z., Pinsky, M., Phillips, V., Prabhakaran, T., Teller, A., den Heever, S. C., and Yano, J.-I.: Representation of microphysical processes in cloud-resolving models: Spectral (bin) microphysics versus bulk parameterization, *Rev. Geophys.*, 53, 247–322, 2015.
- Klocke, D. and Rodwell, M. J.: A comparison of two numerical weather prediction methods for diagnosing fast-physics errors in climate models, *Q. J. Roy. Meteor. Soc.*, 140, 517–524, 2014.
- Klocke, D., Brueck, M., Hohenegger, C., and Stevens, B.: Rediscovery of the doldrums in storm-resolving simulations over the tropical Atlantic, *Nat. Geos.*, 10, 1752–0908, 2017.
- Klotzsche, S. and Macke, A.: Influence of crystal tilt on solar irradiance of cirrus clouds, *Appl. Opt.*, 45, 1034–1040, 2006.
- Kurucz, R.: Synthetic infrared spectra, in *Proceedings of the 154th Symposium of the International Astronomical Union (IAU)*, Tucson, Arizona, March 2-6, 1992, Kluwer, Acad., Norwell, MA, 1992.
- Kylling, A., Webb, A., Kift, R., Gobbi, G., Ammannato, L., Barnaba, F., Bais, A., Kazadzis, S., Wendisch, M., Jäkel, E., Schmidt, S., Kniffka, A., Thiel, S., Junkermann, W., Blumthaler, M., Silbernagl, R., Schallhart, B., Schmitt, R., Kjeldstad, B., Thorseth, T., Scheirer, R., and Mayer, B.: Spectral actinic flux in the lower troposphere: measurement and 1-D simulations for cloudless, broken cloud and overcast situations, *Atmos. Chem. Phys.*, 5, 1975–1997, 2005.
- Lacis, A. A. and Oinas, V.: A description of the correlated k distribution method for modeling nongray gaseous absorption, thermal emission, and multiple scattering in vertically inhomogeneous atmospheres, *J. Geophys. Res. Atmos.*, 96, 9027–9063, 1991.
- Liou, K.: *An Introduction to Atmospheric Radiation*, Academic Press, San Diego, London, 2002.
- Macke, A., Francis, P. N., McFarquhar, G. M., and Kinne, S.: The role of ice particle shapes and size distributions in the single scattering properties of cirrus clouds, *J. Atmos. Sci.*, 55, 2.874–2.883, 1998.
- Madonna, E., Boettcher, M., Grams, C. M., Joos, H., Martius, O., and Wernli, H.: Verification of North Atlantic warm conveyor belt outflows in ECMWF forecasts, *Q. J. Roy. Meteor. Soc.*, 141, 1333–1344, 2014.

- Marshak, A., Davis, A., Wiscombe, W., and Titov, G.: The verisimilitude of the independent pixel approximation used in cloud remote sensing, *Remote Sens. Environ.*, 52, 71–78, 1995.
- Martin, G. M., Johnson, D. W., and Spice, A.: The measurement and parameterization of effective radius of droplets in warm stratocumulus clouds, *J. Atmos. Sci.*, 51, 1823–1842, 1994.
- Martínez-Alvarado, O., Baker, L. H., Gray, S. L., Methven, J., and Plant, R. S.: Distinguishing the Cold Conveyor Belt and Sting Jet Airstreams in an Intense Extratropical Cyclone, *Mon. Weather Rev.*, 142, 2571–2595, <https://doi.org/10.1175/MWR-D-13-00348.1>, 2014.
- Mayer, B. and Kylling, A.: Technical note: The *libRadtran* software package for radiative transfer calculations - description and examples of use, *Atmos. Chem. Phys.*, 5, 1855–1877, 2005.
- Mayer, B., Kylling, A., Emde, C., Buras, R., Hamann, U., Gasteiger, J., and Richter, B.: *libRadtran* user’s guide, 2017.
- McComiskey, A. and Feingold, G.: Quantifying error in the radiative forcing of the first aerosol indirect effect, *Geophys. Res. Lett.*, 35, L02 810, 2008.
- Mech, M., Crewell, S., Meirolt-Mautner, I., Prigent, C., and Chaboureau, J. P.: Information content of millimeter-wave observations for hydrometeor properties in mid-latitudes, *IEEE T. Geosci. Remote*, 45, 2287–2299, 2007.
- Mech, M., Orlandi, E., Crewell, S., Ament, F., Hirsch, L., Hagen, M., Peters, G., and Stevens, B.: HAMP - the microwave package on the High Altitude and Long range research aircraft (HALO), *Atmos. Meas. Tech.*, 7, 4539–4553, 2014.
- Merk, D., Deneke, H., Pospichal, B., and Seifert, P.: Investigation of the adiabatic assumption for estimating cloud micro- and macrophysical properties from satellite and ground observations, *Atmos. Chem. Phys.*, 16, 933–952, 2016.
- Mie, G.: Beiträge zur Optik trüber Medien, speziell kolloidaler Metallösungen, *Annalen der Physik*, Vierte Folge, 25, 377–445, 1908.
- Mlawer, E., Taubman, S., Brown, P., Iacono, M., and Clough, S.: Radiative transfer for inhomogeneous atmospheres: RRTM, a validated correlated-k model for the longwave, *J. Geophys. Res.*, 102, 16 663–16 682, 1997.
- Nuijens, L., Medeiros, B., Sandu, I., and Ahlgrimm, M.: The behavior of trade-wind cloudiness in observations and models: The major cloud components and their variability, *J. Adv. Model. Earth Sy.*, 7, 600–616, 2015.
- Oreopoulos, L. and Davies, R.: Plane parallel albedo biases from satellite observations. Part I: Dependence on resolution and other factors, *J. Climate*, 11, 919–932, 1998a.
- Oreopoulos, L. and Davies, R.: Plane parallel albedo biases from satellite observations. Part II: Parameterization for bias removal, *J. Climate*, 11, 933–944, 1998b.
- Pawlowska, H. and Brenguier, J.-L.: An observational study of drizzle formation in stratocumulus clouds for general circulation model (GCM) parameterizations, *J. Geophys. Res. Atmos.*, 108, 2003.
- Petty, G.: *A First Course in Atmospheric Radiation*, 2nd Edition, Sundog Publishing, Madison, Wisconsin, 2006.
- Pincus, R., Barker, H. W., and Morcrette, J. J.: A fast, flexible, approximate technique for computing radiative transfer in inhomogeneous cloud fields, *J. Geophys. Res.*, 108, 4376, 2003.
- Platnick, S.: Vertical photon transport in cloud remote sensing problems, *J. Geophys. Res.*, 105, 22 919–22 935, 2000.

- Platnick, S. and Twomey, S.: Determining the susceptibility of cloud albedo to changes in droplet concentration with the Advanced Very High Resolution Radiometer, *J. Appl. Meteorol.*, 33, 334–347, 1994.
- Platnick, S., Li, J., King, M., Gerber, H., and Hobbs, P.: A solar reflectance method for retrieving the optical thickness and droplet size of liquid water clouds over snow and ice surfaces, *J. Geophys. Res.*, 106, 15 185–15 199, 2001.
- Platnick, S., King, M., Ackerman, S., Menzel, W., Baum, B., Riedi, J., and Frey, R.: The MODIS cloud products: Algorithms and examples from TERRA, *IEEE Trans. Geosci. Remote Sens.*, 41, 459–473, 2003.
- Platnick, S., Ackerman, S. A., Baum, B. A., Heidinger, A. K., Holz, R. E., King, M. D., Menzel, W. P., Nasiri, S., Weisz, E., and Yang, P.: Assessment of IDPS VIIRS cloud products and recommendations for EOS-era cloud climate data record continuity., Tech. Rep. p. 57, NASA Goddard Space Flight Center, Greenbelt, MD, USA, 2013.
- Platnick, S., Meyer, K. G., King, M. D., Wind, G., Amarasinghe, N., Marchant, B., Arnold, G. T., Zhang, Z., Hubanks, P. A., Holz, R. E., Yang, P., Ridgway, W. L., and Riedi, J.: The MODIS Cloud Optical and Microphysical Products: Collection 6 Updates and Examples From Terra and Aqua, *IEEE Trans. Geosci. Remote Sens.*, 55, 502–525, 2017.
- Pontikis, C. and Hicks, E.: Contribution to the cloud droplet effective radius parameterization, *Geophys. Res. Lett.*, 19, 2227–2230, 1992.
- Pontikis, C. A.: Parameterization of the droplet effective radius of warm layer clouds, *Geophys. Res. Lett.*, 23, 2629–2632, 1996.
- Reid, J. S., Hobbs, P. V., Rangno, A. L., and Hegg, D. A.: Relationships between cloud droplet effective radius, liquid water content, and droplet concentration for warm clouds in Brazil embedded in biomass smoke, *J. Geophys. Res. Atmos.*, 104, 6145–6153, 1999.
- Ricchiazzi, P., Yang, S., Gautier, C., and Sowle, D.: SBDART: A research and teaching software tool for plane-parallel radiative transfer in the Earth’s atmosphere, *Bull. Amer. Meteor. Soc.*, 79, 2101–2114, 1998.
- Rockel, B. and Raschke, E. and Weyres, B.: A parameterization of broad band radiative transfer properties of water, ice, and mixed clouds, *Beitr. Phys. Atmosph.*, 64, 1–12, 1991.
- Romps, D. M.: Exact Expression for the Lifting Condensation Level, *J. Atmos. Sci.*, 74, 3891–3900, 2017.
- Rosenfeld, D.: Aerosol-cloud interactions control of Earth radiation and latent heat release budgets, *Space Sci. Rev.*, 125, 149–157, 2006.
- Rosenfeld, D., Lohmann, U., Raga, G. B., O’Dowd, C. D., Kulmala, M., Fuzzi, S., Reissell, A., and Andreae, M. O.: Flood or drought: How do aerosols affect precipitation?, *Science*, 321, 1309–1313, 2008.
- Sato, Y., Nishizawa, S., Yashiro, H., Miyamoto, Y., Kajikawa, Y., and Tomita, H.: Impacts of cloud microphysics on trade wind cumulus: which cloud microphysics processes contribute to the diversity in a large eddy simulation?, *Prog. Earth Planet. Sc.*, 2, 2197–4284, 2015.
- Schäfler, A., Craig, G., Wernli, H., Arbogast, P., Doyle, J. D., McTaggart-Cowan, R., Methven, J., Rivière, G., Ament, F., Boettcher, M., Bramberger, M., Cazenave, Q., Cotton, R., Crewell, S., Delanoë, J., Dörnbrack, A., Ehrlich, A., Ewald, F., Fix, A., Grams, C. M., Gray, S. L., Grob, H., Groß, S., Hagen, M., Harvey, B., Hirsch, L., Jacob, M., Kölling, T., Konow, H., Lemmerz, C., Lux, O., Magnusson, L., Mayer, B., Mech, M., Moore, R., Pelon, J., Quinting, J., Rahm, S., Rapp, M., Rautenhaus, M., Reitebuch, O., Reynolds, C. A., Sodemann, H., Spengler, T., Vaughan, G., Wendisch, M., Wirth, M., Witschas, B., Wolf, K., and Zinner, T.: The North Atlantic Waveguide and Downstream Impact Experiment, *Bull. Amer. Meteor. Soc.*, 99, 1607–1637, <https://doi.org/10.1175/BAMS-D-17-0003.1>, 2018.

- Scheirer, R.: Solarer Strahlungstransport in der inhomogenen Atmosphäre, Ph.D. thesis, Christian-Albrechts-Universität Kiel, 2001.
- Schnitt, S., Orlandi, E., Mech, M., Ehrlich, A., and Crewell, S.: Characterization of Water Vapor and Clouds During the Next-Generation Aircraft Remote Sensing for Validation (NARVAL) South Studies, *IEEE J. Sel. Top. Appl.*, 10, 3114–3124, <https://doi.org/10.1109/JSTARS.2017.2687943>, 2017.
- Shonk, J. K. P. and Hogan, R. J.: Tripleclouds: an efficient method for representing cloud inhomogeneity in 1D radiation schemes by using three regions at each height, *J. Clim.*, 21, 2352–2370, 2008.
- Shonk, J. K. P., Hogan, R. J., Edwards, J. M., and Mace, G. G.: Effect of improving representation of horizontal and vertical cloud structure on the Earth’s global radiation budget. Part I: Review and parametrization, *Q. J. R. Meteorol. Soc.*, 136, 1191–1204, 2010.
- Siebert, H., Bethke, J., Bierwirth, E., Conrath, T., Dieckmann, K., Ditas, F., Ehrlich, A., Farrell, D., Hartmann, S., Izaguirre, M. A., Katzwinkel, J., Nuijens, L., Roberts, G., Schäfer, M., Shaw, R. A., Schmeissner, T., Serikov, I., Stevens, B., Stratmann, F., Wehner, B., Wendisch, M., Werner, F., and Wex, H.: The fine-scale structure of the trade wind cumuli over Barbados – an introduction to the CARRIBA project, *Atmos. Chem. Phys.*, 13, 10 061–10 077, 2013.
- Slingo, A.: A GCM parameterization for the shortwave radiative properties of water clouds, *J. Atmos. Sci.*, 46, 1419–1427, 1989.
- Stamnes, K., Tsay, S.-C., Wiscombe, W., and Laszlo, I.: DISORT, A General-Purpose Fortran Program for Discrete-Ordinate-Method Radiative Transfer in Scattering and Emitting Layered Media: Documentation of Methodology, Tech. rep., Dept. of Physics and Engineering Physics, Stevens Institute of Technology, Hoboken, NJ 07030, 2000.
- Stephens, G.: Radiation profiles in extended water clouds. II: Parameterization schemes, *J. Atmos. Sci.*, 35, 2123–2132, 1978.
- Stevens, B. and Lenschow, D.: Observations, experiments, and Large Eddy simulation, *Bull. Amer. Meteor. Soc.*, 82, 283–294, 2001.
- Stevens, B., Ament, F., Bony, S., Crewell, S., Ewald, F., Groß, S., Hansen, A., Hirsch, L., Jacob, M., Kölling, T., Konow, H., Mayer, B., Wendisch, M., Wirth, M., Wolf, K., Bakan, S., Bauer-Pfundstein, M., Brück, M., Delanoë, J., Ehrlich, A., Farrell, D., Forde, M., Gödde, F., Grob, H., Hagen, M., Jäkel, E., Jansen, F., Klepp, C., Klingebiel, M., Mech, M., Peters, G., Rapp, M., Wing, E. A., and Zinner, T.: A high-altitude long-range aircraft configured as a cloud observatory - the NARVAL expeditions, *Bull. Amer. Meteor. Soc.*, 100, 1061–1077, <https://doi.org/10.1175/BAMS-D-18-0198.1>, 2019.
- Su, W., Charlock, T., and Rose, F.: Deriving surface ultraviolet radiation from CERES surface and atmospheric radiation budget: Methodology, *J. Geophys. Res.*, 110, doi:10.1029/2005JD005 794, 2005.
- Sun, W. and Fu, Q.: Anomalous diffraction theory for randomly oriented nonspherical particles: a comparison between original and simplified solutions, *J. Quant. Spectrosc. Radiat. Transfer*, 70, 737–747, 2001.
- Sun, Z. and Rikus, L.: Parameterization of effective sizes of cirrus-cloud particles and its verification against observations, *Q. J. R. Meteorol. Soc.*, 125, 3037–3055, 1999.
- Takano, Y. and Liou, K.-N.: Solar radiative transfer in cirrus clouds. Part I: Single-scattering and optical properties of hexagonal ice crystals, *J. Atmos. Sci.*, 46, 1–19, 1989.
- Takano, Y. and Liou, K. N.: Solar Radiative transfer in cirrus clouds. Part III. Light scattering by irregular ice crystals, *J. Atmos. Sci.*, 52, 818–837, 1995.

- Tao, W.-K., Chen, J.-P., Li, Z., Wang, C., and Zhang, C.: Impact of aerosols on convective clouds and precipitation, *Rev. Geophys.*, 50, 1–62, <http://dx.doi.org/10.1029/2011RG000369>, rG2001, 2012.
- Taylor, J. P., Edwards, J. M., Glew, M. D., Hignett, P., and Slingo, A.: Studies with a flexible new radiation code. II: Comparisons with aircraft short-wave observations, *Q. J. Roy Meteor. Soc.*, 122, 839–861, 1996.
- Tegen, I., Hollrig, P., Chin, M., Fung, I., Jacob, D., and Penner, J.: Contribution of different aerosol species to the global aerosol extinction optical thickness: Estimates from model results, *J. Geophys. Res. Atmos.*, 102, 23 895–23 915, 1997.
- Thelen, J.-C. and Edwards, J. M.: Short-wave radiances: comparison between SEVIRI and the Unified Model, *Q. J. Royl. Meteor. Soc.*, 139, 1665–1679, 2012.
- Tiedtke, M.: Representation of clouds in large-scale models, *Mon. Weather. Rev.*, 121, 3040–3061, 1993.
- Tiedtke, M.: An Extension of Cloud-Radiation Parameterization in the ECMWF Model: The Representation of Subgrid-Scale Variations of Optical Depth, *Mon. Weather Rev.*, 124, 745–750, 1996.
- Twomey, S.: The influence of pollution on the shortwave albedo of clouds, *J. Atmos. Sci.*, 34, 1149–1152, 1977.
- vanZanten, M. C., Stevens, B., Vali, G., and Lenschow, D. H.: Observations of Drizzle in Nocturnal Marine Stratocumulus, *J. Atmos. Sci.*, 62, 88–106, 2005.
- Vial, J., Bony, S., Stevens, B., and Vogel, R.: Mechanisms and Model Diversity of Trade-Wind Shallow Cumulus Cloud Feedbacks: A Review, *Surv. Geophys.*, 38, 1331–1353, 2017.
- Voigt, C., Schumann, U., Minikin, A., Abdelmonem, A., Afchine, A., Borrmann, S., Boettcher, M., Buchholz, B., Bugliaro, L., Costa, A., Curtius, J., Dollner, M., Dörnbrack, A., Dreiling, V., Ebert, V., Ehrlich, A., Fix, A., Forster, L., Frank, F., Fütterer, D., Giez, A., Graf, K., Groöf, J.-U., Groß, S., Heimerl, K., Heinold, B., Hüneke, T., Järvinen, E., Jurkat, T., Kaufmann, S., Kenntner, M., Klingebiel, M., Klimach, T., Kohl, R., Krämer, M., Krisna, T. C., Luebke, A., Mayer, M., Mertes, S., Molleker, S., Petzold, A., Pfeilsticker, K., Port, M., Rapp, M., Reutter, P., Rolf, C., Rose, D., Sauer, D., Schäfler, A., Schlage, R., Schnaiter, M., Schneider, J., Spelten, N., Spichtinger, P., Stock, P., Walser, A., Weigel, R., Weinzierl, B., Wendisch, M., Werner, F., Wernli, H., Wirth, M., Zahn, A., Ziereis, H., and Zöger, M.: ML-CIRRUS – The airborne experiment on natural cirrus and contrail cirrus with the high-altitude long-range research aircraft HALO, *Bull. Amer. Meteor. Soc.*, <https://doi.org/10.1175/BAMS-D-15-00213.1>, 2017.
- Warren, S., Hahn, C., London, J., Chervin, R., and Jenne, R.: Global distribution of total cloud cover and cloud type amounts over the ocean, Tech. rep., National Center for Atmospheric Research, Boulder, Colorado, 1988.
- Wendisch, M. and Brenguier, J.-L.: Airborne Measurements for Environmental Research – Methods and Instruments, Wiley-VCH Verlag GmbH & Co. KGaA, Weinheim, Germany, Weinheim, Germany, <https://doi.org/10.1002/9783527653218>, ISBN: 978-3-527-40996-9, 2013.
- Wendisch, M. and Keil, A.: Discrepancies between measured and modeled solar and UV radiation within polluted boundary layer clouds, *J. Geophys. Res.*, 104, 27 373–27 385, 1999.
- Wendisch, M. and Yang, P.: Theory of Atmospheric Radiative Transfer - A Comprehensive Introduction, Wiley-VCH Verlag GmbH & Co. KGaA, Weinheim, Germany, iSBN: 978-3-527-40836-8, 2012.
- Wendisch, M., Müller, D., Schell, D., and Heintzenberg, J.: An airborne spectral albedometer with active horizontal stabilization, *J. Atmos. Oceanic Technol.*, 18, 1856–1866, 2001.

- Wendisch, M., Keil, A., Müller, D., Wandinger, U., Wendling, P., Stifter, A., Petzold, A., Fiebig, M., Wiegner, M., Freudenthaler, V., Armbruster, W., von Hoyningen-Huene, W., and Leiterer, U.: Aerosol-radiation interaction in the cloudless atmosphere during LACE 98. Part 1: Measured and calculated broadband solar and spectral surface insolutions, *J. Geophys. Res.*, 107, Art. No. 8124, 2002.
- Wendisch, M., Pilewskie, P., Jäkel, E., Schmidt, S., Pommier, J., Howard, S., Jonsson, H. H., Guan, H., Schröder, M., and Mayer, B.: Airborne measurements of areal spectral surface albedo over different sea and land surfaces, *J. Geophys. Res.*, 109, Art. No. D08 203, 2004.
- Wendisch, M., Pöschl, U., Andreae, M. O., Machado, L. A. T., Albrecht, R., Schlager, H., Rosenfeld, D., Martin, S. T., Abdelmonem, A., Afchine, A., Araujo, A., Artaxo, R., Aufmhoff, H., Barbosa, H. M. J., Borrmann, S., Braga, R., Buchholz, B., Cecchini, M. A., Costa, A., Curtius, J., Dollner, M., Dorf, M., Dreiling, V., Ebert, V., Ehrlich, A., Ewald, F., Fisch, G., Fix, A., Frank, F., Fütterer, D., Heckl, C., Heidelberg, F., Hüneke, T., Jäkel, E., Järvinen, E., Jurkat, T., Kanter, S., Kästner, U., Kenntner, M., Kesselmeier, J., Klimach, T., Knecht, M., Kohl, R., Kölling, T., Krämer, M., Krüger, M., Krisna, T. C., Lavric, J. V., Longo, K., Mahnke, C., Manzi, A. O., Mayer, B., Mertes, S., Minikin, A., Molleker, S., Münch, S., Nillius, B., Pfeilsticker, K., Pöhlker, C., Roiger, A. E., Rose, D., Rosenow, D., Sauer, D., Schnaiter, M., Schneider, J., Schulz, C., de Souza, R. A. F., Spanu, A., Stock, P., Vila, D., Voigt, C., Walser, A., Walter, D., : The ACRIDICON-CHUVA campaign: Studying tropical deep convective clouds and precipitation over Amazonia using the new German research aircraft HALO, *Bull. Amer. Meteor. Soc.*, 97, 1885–1908, <https://doi.org/10.1175/BAMS-D-14-00255.1>, 2016.
- Werner, F., Siebert, H., Pilewskie, P., Schmeissner, T., Shaw, R. A., and Wendisch, M.: New airborne retrieval approach for trade wind cumulus properties under overlying cirrus, *J. Geophys. Res. Atmos.*, 118, 3634–3649, 2013.
- Werner, F., Ditas, F., Siebert, H., Simmel, M., Wehner, B., Pilewskie, P., Schmeissner, T., Shaw, R. A., Hartmann, S., Wex, H., Roberts, G. C., and Wendisch, M.: Twomey effect observed from collocated microphysical and remote sensing measurements over shallow cumulus, *J. Geophys. Res.*, 119, 1534–1545, 2014.
- Wolf, K., Ehrlich, A., Jacob, M., Crewell, S., Wirth, M., and Wendisch, M.: Improvement of airborne retrievals of cloud droplet number concentration of trade wind cumulus using a synergetic approach, *Atmos. Meas. Tech.*, 12, 1635–1658, 2019.
- Wood, R.: Relationships between optical depth, liquid water path, droplet concentration and effective radius in an adiabatic layer cloud, personal note, 2006.
- Wood, R.: Stratocumulus clouds, *Mon. Wea. Rev.*, 140, 2373–2423, 2012.
- Yang, P. and Liou, K. N.: Geometric-optics-integral-equation method for light scattering by non-spherical ice crystals, *Appl. Opt.*, 35, 6.568–6.584, 1996.
- Yang, P., Liou, K. N., Wyser, K., and Mitchell, D.: Parameterization of the scattering and absorption properties of individual ice crystals, *J. Geophys. Res.*, 105, 4.699–4.718, 2000.
- Yang, P., Wei, H. L., Huang, H. L., Baum, B. A., Hu, Y. X., Kattawar, G. W., Mishchenko, M. I., and Fu, Q.: Scattering and absorption property database for nonspherical ice particles in the near-through far-infrared spectral region, *Appl. Opt.*, 44, 5512–5523, 2005.
- Yi, B., Yang, P., Baum, B. A., L'Ecuyer, T., Oreopoulos, L., Mlawer, E. J., Heymsfield, A. J., and Liou, K.-N.: Influence of ice particle surface roughening on the global cloud radiative effect, *J. Atmos. Sci.*, 70, 2794–2807, 2013.
- Zhang, J., Li, Z., Chen, H., and Cribb, M.: Validation of a radiosonde-based cloud layer detection method against a ground-based remote sensing method at multiple ARM sites, *J. Geophys. Res.-Atmos.*, 118, 846–858, 2013.

List of Symbols

Symbol	Symbol in Code	Unit	Longname
-	RRE2DE	-	Ratio of ice particle radius to ice particle diameter
-	RTT	K	Fusion-temperature of water
α_λ	-	-	Spectral Albedo
α_{cld}	-	-	Cloud Top Albedo
α_{sea}	-	-	Sea Surface Albedo
χ	-	-	Ratio of Upward Radiance for Cloud Mask
χ_p	-	-	Ratio of Cloud Top Phase
$d^2\Omega$	-	sr	Differential Solid Angle
δ_S	-	$^\circ$	Declination of Sun
Δz	-	m	Distance between Aircraft and Cloud Top
ϵ_r	ZRATIO	-	Ratio of Spectral Dispersion
ϵ	ZWOOD_FACTOR	-	Wood Factor
γ_λ	-	-	Spectral Reflectivity
$\gamma_{\lambda,P}$	-	-	Spectral Reflectivity of Reflectivity Panel
Γ_{calc}	-	K m^{-1}	Calculated Lapse-Rate
Γ_{OI}	-	rad or $^\circ$	Field of View of Optical Inlet
κ	-	-	Transmission Function
λ	-	μm	Wavelength
Λ	-	-	Number of Legendre Moments
ν	-	m^{-1}	Wavenumber
$\tilde{\omega}$	-	-	Single Scattering Albedo
$\langle\tilde{\omega}\rangle$	-	-	Volumetric Single Scattering Albedo
Ω	-	sr	Solid Angle
π	RPI	-	Pi
ϕ	PLAT	$^\circ$	Geographic Latitude
ϕ_{ac}	-	rad or $^\circ$	Aircraft Roll Angle
Φ_λ	-	$\text{J s}^{-1} \text{nm}^{-1}$	Spectral Radiant Energy Flux
φ_0	-	rad or $^\circ$	Solar Azimuth Angle
ψ	-	-	Relative Deviation in Sensitivity Study
ρ_{air}	ZAIR_DENSITY_GM3	g cm^{-3}	Density of Dry Air
ρ_{ice}	-	g m^{-3}	Density of Ice
ρ_{liq}	-	g m^{-3}	Density of Liquid Water
σ	-	variable	Standard Deviation
σ_{ext}	-	m^{-1}	Extinction Coefficient
τ	-	-	Cloud Optical Thickness
τ_A	-	-	Cloud Optical Thickness derived with Method A
τ_B	-	-	Cloud Optical Thickness derived with Method B

τ_{eR}	-	-	Cloud Optical Thickness of ecRad
τ_{MOD}	-	-	Cloud Optical Thickness of MODIS
θ	-	rad or $^{\circ}$	Atmospheric Zenith Angle
θ_0	-	rad or $^{\circ}$	Solar Zenith Angle
θ_{ac}	-	rad or $^{\circ}$	Aircraft Pitch Angle
ϑ	-	rad or $^{\circ}$	Scattering Angle
Υ	-	rad or $^{\circ}$	Wind Direction
ζ	-	a.u.	Arbitrary Measurement Signal
b_{ext}	-	m^{-1}	Spectral Volumetric Extinction Coefficient
b_{sca}	-	m^{-1}	Spectral Volumetric Scattering Coefficient
b_i	-		Legendre Moments
$\langle b_i \rangle$	-	-	Volumetric Legendre Moments
c_{λ}	-	-	Spectral Calibration Factor
c_p	-	J K^{-1}	Specific Heat Capacity (const. p)
$\text{d}^2 A$	-	m^2	Infinitesimal Area Element
$\text{d}z$	-	m	Cloud Geometric Thickness
$\frac{\text{d}N}{\text{d}D}(D)$	-	m^{-1}	Number Size Distribution
f	PCLOUD_FRAC	0 - 1 or %	Cloud Fraction
f_{ad}	-	-	Degree of Adiabaticity
f_{tot}	-	0 - 1 or %	Total Cloud Cover
$f_{\text{tot,eR}}$	SW_CLOUD_COVER	0 - 1 or %	Total Cloud Cover ecRad
$f_{\text{tot,lib}}$	-	0 - 1 or %	Total Cloud Cover libRadtran
$f_{\text{tot,mea}}$	-	0 - 1 or %	Total Cloud Cover SMART
g_{geo}	-	m s^{-2}	Gravitational Constant
h	-	$^{\circ}$	Hour Angle of Sun
h_{ac}	-	m or km	Flight Altitude of HALO
h_{BT}	-	m	Cloud Base Height
h_{CT}	-	m	Cloud Top Height
h_{geo}	-	m or km	Geometric Height
h_{LCL}	-	m	Lifting Condensation Level
i	-	-	Band Number of ecRad
k	ZSPECTRAL_DISPERSION	0 - 1	Spectral Dispersion
k_{B}	-	$\text{W m}^{-2} \text{K}^{-4}$	Stefan-Boltzmann Constant
k_{cos}	-	-	Cosine Correction Factor
k_{corr}	-	-	Correction Factor for $r_{\text{eff,ice}}$
\tilde{n}	-	-	Complex Index of Refraction
\tilde{n}_{i}	-	-	Imaginary Part of Index of Refraction
\hat{n}	-	-	Unit Vector
p	PPRESSURE	Pa	Pressure
p_{CT}	-	Pa	Cloud Top Pressure
p_{SLP}	-	Pa	Sea Level Pressure
q	PQ	g kg^{-1}	Mean Specific Humidity
q_{rw}	PQ_RAIN	kg kg^{-1}	Specific Rain Water Content
q_{liq}	PQ_LIQ	kg kg^{-1}	Specific Liquid Water Content
q_{ice}	PQ_ICE	kg kg^{-1}	Specific Ice Water Content
q_{sn}	PQ_SNOW	kg kg^{-1}	Specific Snow Water Content

r_{eff}	PRE_UM	μm	Effective Radius
$r_{\text{eff,A}}$	-	μm	Retrieved Effective Radius with Method A
$r_{\text{eff,B}}$	-	μm	Retrieved Effective Radius with Method B
$r_{\text{eff,liq,min}}$	PP_MIN_RE_UM	μm	Minimum Liquid Effective Radius
$r_{\text{eff,liq,max}}$	PP_MAX_RE_UM	μm	Maximum Liquid Effective Radius
$r_{\text{eff,liq}}^3$	ZRE_CUBED	μm^{-3}	Cubed Liquid Effective Radius
r_{vol}	-	μm	Volumetric Radius
\hat{s}	-	-	Direction of Propagation
t	-	s	Time
t_{int}	-	s	Integration Time
u	-	m s^{-1}	u-Wind Component
u_{10}	-	m s^{-1}	10m u-Wind Component
v	-	m s^{-1}	v-Wind Component
v_{10}	-	m s^{-1}	10m v-Wind Component
v_{ac}	-	m s^{-1}	Aircraft Velocity
x	-	-	Applied Ice Parameterization
A_D	-	m^2	Projected Area of an Ice Crystal
A_{FOV}	-	m	Area of SMART FOV
$A_{\lambda,L}$	-	$\text{W m}^{-2} \text{nm}^{-1} \text{sr}^{-1}$	Spectral Absolute Calibration Factors from Lamp
$A_{\lambda,S}$	-	$\text{W m}^{-2} \text{nm}^{-1} \text{sr}^{-1}$	Spectral Absolute Calibration Factors from Integrating Sphere
B_i	-	-	Bin
C_{abs}	-	m^2	Absorption Cross Section
C_{ext}	-	m^2	Extinction Cross Section
C_{sca}	-	m^2	Scattering Cross Section
D	-	m	Diameter of Cloud Particle
D_{max}	-	m	Maximum Dimension of an Ice Crystal
D_{eff}	-	μm	Particle Effective Diameter
$D_{\text{eff,ice}}$	ZDIAMETER_UM	μm	Ice Effective Diameter
$D_{\text{eff,ice,min}}$	ZMIN_DIAMETER_UM	μm	Minimum Ice Effective Diameter
$D_{\text{eff,ice,def}}$	ZDEFAULT_RE_UM	μm	Default Ice Effective Diameter
D_{FOV}	-	m	Diameter of SMART FOV
D_{Fu}	-	m	Ice Particle Diameter after Fu
E_{nr}	-	-	Power Spectral Density with Reduced Noise Characteristics
E_{rad}	-	J	Radiant Energy
F_{λ}	-	$\text{W m}^{-2} \text{nm}^{-1}$	Spectral Irradiance
$F_{\lambda,\text{Bulk}}^{\downarrow}$	-	$\text{W m}^{-2} \text{nm}^{-1}$	Downward Spectral Irradiance with Bulk Crystal Scattering Properties
$F_{\text{cor}}^{\downarrow}$	-	$\text{W m}^{-2} \text{nm}^{-1}$	Cosine Corrected Downward Irradiance
F_{inc}	-	$\text{W m}^{-2} \text{nm}^{-1}$	Incident Irradiance

F_{λ}^{\downarrow}	-	$\text{W m}^{-2} \text{ nm}^{-1}$	Downward Spectral Irradiance
F_{λ}^{\uparrow}	-	$\text{W m}^{-2} \text{ nm}^{-1}$	Upward Spectral Irradiance
FWHM	-	m	Full Width at Half Maximum
G	-	-	Digital Signal
I_{λ}	-	$\text{W m}^{-2} \text{ nm}^{-1} \text{ sr}^{-1}$	Spectral Radiance
$\overline{I_{\lambda}^{\uparrow}}$	-	$\text{W m}^{-2} \text{ nm}^{-1} \text{ sr}^{-1}$	Mean Upward Spectral Radiance
$I_{\lambda, \text{Bulk}}^{\uparrow}$	-	$\text{W m}^{-2} \text{ nm}^{-1} \text{ sr}^{-1}$	Upward Spectral Radiance with Bulk Crystal Scattering Properties
$I_{\lambda, \text{tr}, i}^{\uparrow}$	-	$\text{W m}^{-2} \text{ nm}^{-1} \text{ sr}^{-1}$	Transformed Spectral Radiance
I_{λ}^{\downarrow}	-	$\text{W m}^{-2} \text{ nm}^{-1} \text{ sr}^{-1}$	Downward Spectral Radiance
I_{λ}^{\uparrow}	-	$\text{W m}^{-2} \text{ nm}^{-1} \text{ sr}^{-1}$	Upward Spectral Radiance
$I_{\lambda, \text{S}}$	-	$\text{W m}^{-2} \text{ nm}^{-1} \text{ sr}^{-1}$	Defined Diffuse Radiance of Integrating Sphere
I_{diff}	-	$\text{W m}^{-2} \text{ nm}^{-1} \text{ sr}^{-1}$	Diffuse Solar Radiance
I_{dir}	-	$\text{W m}^{-2} \text{ nm}^{-1} \text{ sr}^{-1}$	Direct Solar Radiance
J_{diff}	-	$\text{W m}^{-2} \text{ nm}^{-1} \text{ sr}^{-1}$	Diffuse Source Term
J_{dir}	-	$\text{W m}^{-2} \text{ nm}^{-1} \text{ sr}^{-1}$	Direct Source Term
IWC	-	g m^{-3}	Ice Water Content
IWC_{cld}	ZIWC_INCLOUD_GM3	g cm^{-3}	In-cloud Ice Water Content
IWP	-	g m^{-2}	Ice Water Path
\mathcal{K}	-	m	Cloud Decorrelation Length
LSM	-	Land Sea Mask	
LWC	-	g m^{-3}	Liquid Water Content
LWC_{cld}	ZLWC_GM3	g cm^{-3}	In-cloud Liquid Water Content
LWP	-	g m^{-2}	Liquid Water Path
N	ZNTOT_CM3	cm^{-3}	Total Number of Activated Condensation Nuclei over Sea
N_A	-	cm^{-3}	Cloud Droplet Number Concentration by Method A
N_B	-	cm^{-3}	Cloud Droplet Number Concentration by Method B
N_C	-	cm^{-3}	Cloud Droplet Number Concentration by Method C
$N_{\text{p, sea}}$	PCCN_SEA	cm^{-3}	Activated Cloud Particle Number Concentration over Sea
N_{sea}	ZCCN	cm^{-3}	Cloud Condensation Nuclei Concentration over Sea
P	-	-	Pixel
\mathcal{P}	-	-	Phase Function
\mathcal{P}_i	-	-	Legendre Polynomials
Q_{λ}	-	-	Spectral Radiometric Quantity
R	-	0-1	Cloud Top Reflectivity
R_{dry}	R_DRY	$\text{J kg}^{-1} \text{ K}^{-1}$	Specific Gas Constant of Dry Air
RMSE	-	variable	Root Mean Square Error
RWC_{cld}	ZRWC_GM3	g cm^{-3}	In-cloud Rain Water Content
S	-	-	Measured Counts

S_0	-	$\text{W m}^{-2} \text{nm}^{-1}$	Extraterrestrial Irradiance
\mathcal{S}	-	km	Spatial Scale
T	PTEMPERATURE	K	Temperature
T_C	ZTEMPERATURE_C	$^{\circ}\text{C}$	Temperature
T_{CT}	-	K	Cloud Top Temperature
T_v	-	K	Virtual Temperature
T_s	-	K	Skin Temperature
\mathcal{T}_λ	-	-	Spectral Transfer Calibration Factors
TWP	-	g m^{-2}	Total Water Path
Z	-	dBz	Radar Reflectivity

List of Abbreviations and Acronyms

1D	one-dimensional
3D	three-dimensional
BB	Broadband
BLC	Boundary Layer Clouds
BT	Brightness Temperature
CCN	Cloud Condensation Nuclei
CDNC	Cloud Droplet Number Concentration
CB	Cloud Base
CBH	Cloud Base Height
CC	Cloud Case
CERES	Clouds and the Earth's Radiant Energy System
COA	Cloud Overlap Assumption
CRF	Cloud Radiative Forcing
CT	Cloud Top
CTA	Cloud Top Albedo
CTH	Cloud Top Height
CTP	Cloud Top Phase
CTR	Cloud Top Reflectivity
DISORT	Discrete Ordinate Radiative Transfer Solver
DLR	German Aerospace Center
DU	Dobson Units
ECHAM	ECMWF HAMburg
ECMWF	European Center for Medium Range Forecast
ecRad	ecMWF Radiation scheme
ETH	Eidgenössische Technische Hochschule
ERA 5	ECMWF Re-Analysis 5
FCC	Fractional Cloud Cover
FOV	Field of View
FSD	Fractional Standard Deviation
FWHM	Full Width at Half Maximum
GCM	Global Climate Model
GPM	Global Precipitation Measurement
GPS	Global Positioning System
HALO	High Altitude and Long Range Research Aircraft
HAMP	HALO Microwave Package
HCF	Homogeneity Cloud Flag
HIW	High Impact Weather
ICON	Icosahedral Nonhydrostatic
IDL	Interactive Data Language
IFS	Integrated Forecast System
IFS AD	IFS Analysis Data
IMU	Inertial Measurement Unit
IPA	Independent Pixel Approximation
ISA	International Standard Atmosphere
IWC	Ice Water Content
ITCZ	Intertropical Convergence Zone
libRadtran	library for Radiative transfer

LIM	Leipzig Institute for Meteorology
LMU	Ludwig-Maximilians-University
LSM	Land-Sea-Mask
LUT	Lookup Tables
LWC	Liquid Water Content
McICA	Monte Carlo Independent Column Approximation
MESO-NH	mesoscale atmospheric model
MODIS	Moderate-resolution Imaging Spectroradiometer
MPI	Max-Planck Institute
NARVAL	Next Generation Remote Sensing for Validation Studies
NASA	National Aeronautics and Space Administration
NAWDEX	North Atlantic Waveguide and Downstream impact EXperiment
NetCDF	Network Common Data Format
NIR	Visible to Near-Infrared Spectral Wavelength Range
NIST	National Institute of Standards and Technology
NWP	Numerical Weather Prediction
PAMTRA	Passive and Active Microwave TRAnsfer model
PDA	Photodiode Array
PDF	Probability Density Function
PGS	Plane-Grating Spectrometers
PSD	Particle Size Distribution
PV	Potential Vorticity
RF	Research Flight
RP	Reference Profile
RRTM-G	Rapid Radiative Transfer Model for Global Climate Models
RT	Radiative Transfer
RTE	Radiative Transfer Equation
RTS	Radiative Transfer Simulation
RWC	Rain Water Content
SBDART	Santa Barbara DISORT Atmospheric Radiative Transfer
SMART	Spectral Modular Airborne Radiation measurement sysTem
SNR	Signal-to-Noise-Ratio
SOD	Seconds of Day
SPARTACUS	Speedy Algorithm for Radiative Transfer through Cloud Sides
specMACS	spectrometer of the Munich Aerosol Cloud Scanner
SSFR	Solar Spectral Flux Radiometer
SWC	Snow Water Content
SZA	Solar Zenith Angle
SWIR	Shortwave-Infrared Spectral Wavelength Range
TC	Tropical Cyclone
TCC	Total Cloud Cover
TOA	Top of Atmosphere
TPV	Tropical Polar Vortex
TROPOS	Leibniz Institute for Tropospheric Research
UK	United Kingdom
UTC	Universal Time Coordinated
VIS	Visible Spectral Wavelength Range
WALES	Water vapour Lidar Experiment in Space
WCB	Warm Conveyor Belt
WWRP	World Weather Research Program

List of Figures

1.1	Illustration of comparisons strategy.	5
2.1	Illustration of the definition of radiances.	8
2.2	Solid angles in Polar Coordinates.	9
2.3	Scattering phase function of liquid water droplet and ice crystal.	10
2.4	Spectral single-scattering albedo of Baum and Fu ice parameterization.	11
2.5	ecRad calculation scheme	15
2.6	Spectral bands of ecRad and absorption due to bands.	17
3.1	HALO instrument overview.	21
3.2	SMART measurement schematic	23
3.3	Sketch of irradiance optical inlet.	24
3.4	Footprint size dependence on distance.	24
3.5	Irradiance calibration factors.	26
3.6	Flight tracks during NARVAL-II.	29
3.7	HALO flight pattern of 19 August 2016.	29
3.8	Flight tracks during NAWDEX.	31
3.9	HALO flight pattern of 26 September 2016.	31
4.1	Time series of CDNC retrieval fro 19 August 2016	40
4.2	PDF of cloud droplet number concentration.	42
4.3	Dependence of cloud top reflectivity on cloud droplet number concentration.	42
5.1	Relative uncertainties in ecRad from Ifs-input.	49
5.2	Modeled cloud top albedo sensitivity from libRadtran and ecRad	52
5.3	Time series of upward irradiance from ecRad for IPA, non-IPA, and the SMART ob- servations	54
5.4	PDF of broadband downward irradiance for NAWDEX.	55
5.5	PDFs of spectral and broadband cloud top albedo for RF06 of NARVAL-II.	56
5.6	PDF of total cloud cover for NAWDEX.	57
5.7	Time series for entire NAWDEX flight.	58
5.8	PDF of broadband upward irradiance of entire NAWDEX flight.	59
5.9	PDFs of spectral and broadband cloud top albedo for first ice cloud case.	61
5.10	Exemplary spectra of from first ice cloud #1.	62
5.11	Absolute difference in spectral cloud top albedo between SMART and ecRad.	63
5.12	Spectral cloud top albedo α	64
5.13	PDFs of spectral and broadband cloud top albedo for second ice cloud case.	66
5.14	PDFs of spectral and broadband cloud top albedo for boundary layer cloud case.	67
5.15	PDF of total cloud cover of entire RF06 of NARVAL-II.	68
5.16	Time series of entire RF06 of NARVAL-II.	69
5.17	PDF of broadband upward irradiances of entire RF06 of NARVAL-II.	71
5.18	PDFs of spectral and broadband cloud top albedo of entire RF06 from NARVAL-II.	72
5.19	PDFs of spectral and broadband cloud top albedo ($f_{\text{tot}} > 20\%$) of entire RF06 from NARVAL-II.	72
5.20	PDF of absolute differences between simulated and observed upward irradiance of entire RF06 of NARVAL-II.	73
5.21	PDF of absolute differences between simulated upward irradiance separated of entire RF06 of NARVAL-II.	74

5.22 PDF of absolute differences between simulated and observed upward irradiance separated for LWC and f_{tot} of entire RF06 of NARVAL-II.	75
---	----

List of Tables

1.1	List of characteristic features of ecRad and libRadtran.	4
2.1	List of spectral bands used in the ecRad scheme for the shortwave wavelength range. .	16
3.1	List of installed instruments during NARVAL-II and NAWDEX.	22
3.2	SMART measurement uncertainties.	27
3.3	List of measurement flights during NARVAL-II.	29
3.4	List of measurement flights during NARVAL-II.	30
4.1	CDNC parameter overview	38
4.2	Mean values of cloud properties of the presented cloud section.	41
5.1	List of p-file variables.	44
5.2	Mandatory ecRad input variables.	45
5.3	List of ecRad output variables.	47
5.4	Median values of solar upward irradiances F^\uparrow of the entire RF04.	59
5.5	Microphysical and macrophysical properties, solar zenith angle (SZA), and flight parameters of the selected cloud cases.	60
5.6	List of ice cloud (I) mean and median values.	61
5.7	List of ice cloud (II) mean and median values.	65
5.8	List of liquid cloud mean and median values.	66
5.9	List of NARVAL-II cloud case mean and median values.	71
7.1	List of key parameters of the ecRad namelist.	81